FLOW ENVIRONMENT ON CULTURED ENDOTHELIAL CELLS USING COMPUTATIONAL FLUID DYNAMICS

A Thesis
Presented to
The Academic Faculty

by

Massimiliano Pezzoli

In Partial Fulfillment
of the Requirements for the Degree
Doctor of Philosophy in
Bioengineering

School of Biomedical Engineering
Georgia Institute of Technology
December 2007

FLOW ENVIRONMENT ON CULTURED ENDOTHELIAL CELLS USING COMPUTATIONAL FLUID DYNAMICS

Approved by:

Professor Don P. Giddens, Advisor
School of Biomedical Engineering
Georgia Institute of Technology

Professor Xiangmin Jiao
College of Computing
Georgia Institute of Technology

Professor Hanjoong Jo
School of Biomedical Engineering
Georgia Institute of Technology

Professor Lakshmi N. Sankar
School of Aerospace Engineering
Georgia Institute of Technology

Professor Raymond Vito
School of Biomedical Engineering
Georgia Institute of Technology

Date Approved: July 2007

Ai miei genitori,

e a chiunque mi abbia voluto bene anche solo per un istante...

ACKNOWLEDGEMENTS

There are a number of people I would like to thank for their help and support during my five years of PhD studies. First, I want to thank my family for their constant loving support, especially when my decisions were not that easy to understand. I really feel lucky to have them always on my side.

Special thanks goes to my advisor Dr. Don Giddens for your guidance and your support, which allowed me to take full advantage of the opportunities I was given at Georgia Tech. I also sincerely appreciated your understanding of my personal situation during a particularly difficult time. I would also like to thank Dr. Xiangmin Jiao, Dr. Hanjoong Jo, Dr. Lakshmi N. Sankar and Dr. Raymond Vito for being part of my thesis committee.

I would like to thank all of the members of the "Cardiovascular Biofluid Dynamics Laboratory" for your support and friendship. A sincere thanks goes also to Michelle Sykes for providing me with the cultured endothelial cells, and to Tai-De Li for his precious AFM measurements.

To Chris, Pat, Lisa and Steven, you guys have been great and made my life here much easier. And in particular to Joanne, always there to help me in exchange for a few Italian recipes...

E finalmente si arriva agli amici. Un grazie particolare a Valerio, che nel momento del bisogno mi e' stato di immenso aiuto, dimostrandomi di essere un amico speciale. E ricordandomi di cio', mi sento di ringraziare dal profondo del cuore Paola e Leda, due donne fantastiche.

Un ulteriore ringraziamento a Stefano "Il cubista", per essere sempre stato un amico di livello, a Serkan, ormai turk-italiano, per il suo altruismo, e a Laura, per

essermi stata vicina.

Per ultima, e non certo per importanza, la famiglia. Un immenso grazie ai miei genitori, persone assolutamente fantastiche, a mio fratello Luca e a Linda, e ai miei nonni Romoletto, Maria e Palmira. Capitolo a parte per ringraziare l'unico altro PhD della mia famiglia, anche se honoris causa: nonno Mommino. Vi voglio bene.

TABLE OF CONTENTS

LIST OF FIGURES

SUMMARY

Atherosclerosis is a systemic disease occurring in specific sections of the cardiovascular tree such as the carotid and the coronary arteries. Atherosclerotic plaques consist of deposits of fatty substances, cholesterol, cellular waste products, calcium and other substances built up in the inner lining of an artery. The growth of these plaques can significantly reduce blood supply to the artery. In case of a plaque rupture, blood clots can form local occlusions or break off, travel downstream the arterial tree and finally occlude smaller arteries, causing tissues infarcts.

Previous studies proposed a strong correlation between plaque localization and blood flow patterns in specific sections of the arteries. In order to elucidate cellular mechanisms that contribute to atherosclerosis, standard cone-and-plate devices are widely used in experiments to reproduce in vitro the effect of different hemodynamic conditions on endothelial cells.

In this study, a novel computational fluid dynamic (CFD) numerical code based on the immersed boundary method is developed to simulate this microscopic flow field under different geometries and flow conditions. The Navier-Stokes equations are solved on a fixed Cartesian grid, and any boundary surface is discretized with an unstructured mesh. To impose physical boundary conditions on the underlying Cartesian grid, a new algorithm to exchange information between the two separate meshes is developed. The same algorithm can be used to account for any solid body with prescribed motion inside the flow field. A comprehensive validation of the CFD code is performed. The computed solutions for standard test problems are compared with analytical solutions, when available, or with results considered as benchmark

solutions in the available literature. Once validated, the code is used to analyze the flow field in the cone-and-plate device simulating conditions typically employed in endothelial cell experiments.

No previous studies have yet been performed on the fluid dynamics of the cone-and-plate device when surfaces representing actual endothelial cell contours are modeled on the plate surface. This represents a great opportunity to correlate the fluid dynamics in the experimental device and the biochemical properties of the cells under specific flow conditions. The challenging aspect of the problem is represented by its different length scales. While the size of the cone-and-plate device is of the order of millimeters, the endothelial cells laying on the plate surface have size of the order of microns. The goal is to obtain a spatial resolution smaller than the height of the single cell. This allows us to investigate the biological features of the endothelial cells under shear stress in different areas of their membrane surface. This feature must be incorporated in the numerical grid, representing a challenging computational problem and is expected to be a major contribution of the research.

CHAPTER I

INTRODUCTION

1.1 Atherosclerosis

Cardiovascular disease (CVD) is the main cause of death in the United States. Estimates are that 71,300,000 Americans have one or more forms of cardiovascular disease [1]. Mortality data show that CVD as the underlying cause of death accounts for about 37.3 percent of all deaths in the United States. CVD is also the leading cause of death in Europe, accounting for over 4 million deaths each year. Nearly half of all deaths in Europe are from CVD [2]. Cardiovascular diseases include coronary heart disease (CHD), stroke, heart failure, high blood pressure, diseases of the arteries, congenital cardiovascular defect and others. Among these, CHD is by far the most prevalent, accounting for about 53 percent of CVD deaths in the United States and 50 percent in Europe.

Atherosclerosis is a systemic disease occurring in specific sections of the cardiovascular tree such as the carotid and the coronary arteries [35]. The lesions of atherosclerosis represent a series of highly specific cellular and molecular responses that can best be described, in aggregate, as an inflammatory disease [81]. Numerous pathophysiologic observations led to the formulation of the response-to-injury hypothesis of atherosclerosis. According to this theory, each characteristic lesion of atherosclerosis represents a different stage in a chronic inflammatory process in the artery; if unabated and excessive, this process will result in an advanced, complicated lesion. Possible causes of endothelial dysfunction leading to atherosclerosis include elevated and modified LDL, free radicals caused by cigarette smoking, hypertension, diabetes mellitus, genetic alterations, infectious microorganisms and combinations of these or

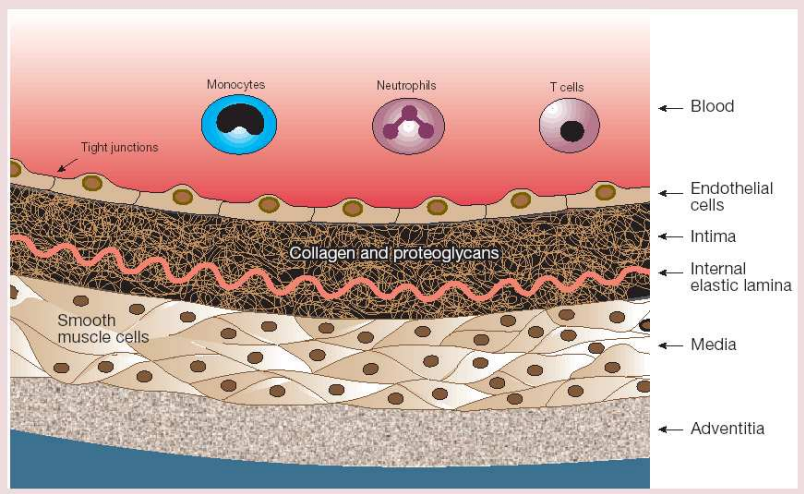

Figure 1: Diagrammatic representation of the main components of a normal vascular wall [62].

other factors. Regardless of the cause of endothelial dysfunction, atherosclerosis is a highly characteristic response of particular arteries [80].

The basic constituents of the walls of blood vessels are cells, predominantly endothelial cells and smooth muscle cells, and extracellular matrix, including elastin and collagen. As shown in figure 1, from a cross section view of a blood vessel we can identify three concentric layers: *intima, media* and *adventitia* [78]. In normal arteries, the intima consists of a single layer of endothelial cells, with minimal underlying sub-endothelial connective tissue, and is separated from the media by a dense elastic membrane called the *internal elastic lamina*. The media layer consists mainly of smooth muscle cells, and is separated from the adventitia by the *external elastic lamina*. The outermost layer, the adventitia, consists of connective tissue with nerve fibers and the *vasa vasorum* [78].

The endothelial dysfunction that results from injury leads to compensatory responses that alter the normal homeostatic properties of the endothelium. Adhesiveness of the endothelium with respect to leukocytes or platelets is increased, as well as its permeability. The injury also induces the endothelium to have procoagulant

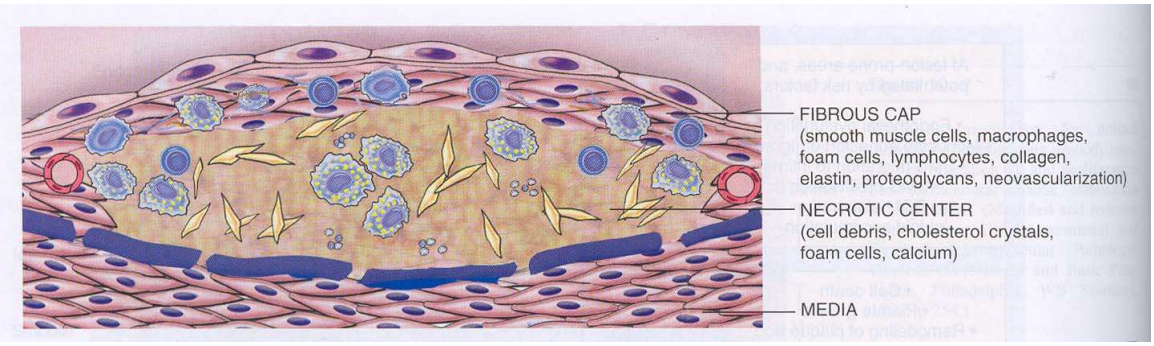

Figure 2: Schematic description of the major components of a well-developed atherosclerotic plaque [78].

instead of anticoagulant properties and to produce vasoactive molecules. In case the inflammatory response does not neutralize or remove the offending agents, it can continue indefinitely [80]. As for the inflammatory cells, the response is mediated by monocytes and T lymphocytes in the bloodstream that adhere to the endothelium and then transmigrate across the endothelial monolayer into the intima. Here, monocytes proliferate, differentiate into macrophages and take up lipoproteins, forming foam cells [62]. With time, activation of these cells leads to the release of hydrolytic enzymes which can induce further damage and eventually lead to focal necrosis, contributing their lipid-filled contents to the necrotic core of the lesion. In doing so, the inflammatory response can also stimulate migration and proliferation of smooth-muscle cells from the medial layer into the area of inflammation to form an intermediate lesion. As smooth muscle cells secrete fibrous elements, occlusive fibrous plaques develop and increase in size. If these responses continue, they can thicken the artery wall, which at first compensates by a gradual "remodeling" dilation of the artery so that the lumen remains unaltered [39]. At this stage, the lesion can continue to grow by the migration of new mononuclear cells from the blood. Thus, cycles of accumulation of mononuclear cells and extracellular lipid, migration and proliferation of smooth-muscle cells, production of extracellular matrix and formation of fibrous tissue lead to further enlargement and restructuring of the lesion, so that it becomes covered by

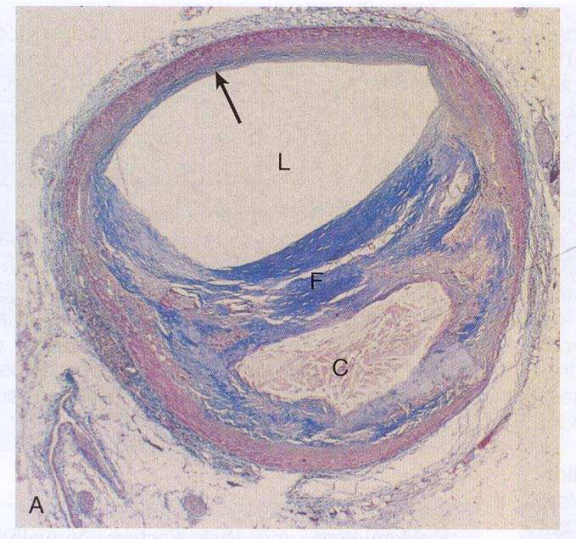

Figure 3: Histological features of an atherosclerotic plaque in a coronary artery [78] (F) fibrous cap, (C) lipid core, (L) narrowed lumen.

a fibrous cap that overlies a core of lipid and necrotic tissue. This advanced lesion is schematically represented in figure 2. At some point, the artery can no longer compensate by dilation and the lesion may then intrude into the lumen and alter the blood flow. The nature of the fibrous cap plays a crucial role in the atherosclerotic lesion. When the fibrous cap is thick and dense, it apparently provides stability to the lesion, whereas when a nonuniform fibrous cap with thin "shoulders" is present the lesion can be unstable. In this condition, rheological forces may affect it and lead to rupture or ulceration with a second hemorrhage, which can occur either from the lumen of the vessel or from the vasa vasora developed to provide nutrients and oxygen to the cells inside the lesion [79]. In case of a plaque rupture, local occlusions can occur or blood clots can form, break off, travel downstream the arterial tree and finally occlude smaller arteries, causing tissue infarcts [22, 34]. Figure 3 shows the histology of a fibrous plaque in the coronary artery. Even if it has been questioned if each type of lesion acts as a precursor for the others, it has been observed that with growth and time some early lesions may progress to fibrous plaques, whereas others

may either remain stable or regress and disappear [79, 65].

As the main cellular components of blood vessel walls, endothelial cells not only act as a liner for the vessel but they play numerous functional roles that, when disturbed, may participate in atherogenesis. In their physiological state, endothelial cells provide a non-adherent surface for leukocyte and platelets, and they act as a permeability barrier that controls the exchange of nutrients and fluid between the plasma and the artery wall. Endothelial cells are also crucial in maintaining the vascular tone by release of vasodilatory and vasoconstrictive molecules, being also responsible for modifying substances from the plasma such as lipoproteins that are transported into the arterial wall. Other functions include the formation and maintenance of connective tissue matrix, collagen and elastic fibers [79]. Moreover, endothelial cells modulate several aspects of normal hemostasis. Whenever needed, they exhibit antiplatelet, anticoagulant and fibrinolytic properties, but under different conditions they are capable of exerting procoagulant functions. The balance between anti- and prothrombotic activities of the endothelium determines whether thrombus formation, propagation or dissolution occurs.

1.2 Fluid mechanics in understanding Atherosclerosis

Formation of atherosclerotic plaques does not occur in a random fashion. Atherosclerotic plaques are most likely to arise in areas where branches or bifurcations are present. Specific sites such as the coronary arteries, the carotid artery and the major branches of the aortic arch are preferred sites of lesion formation within the arteries [27]. Lesions are mainly found along the outer walls of bifurcations, whereas the inner walls seem to be unaffected by plaques. Similarly, no atherosclerotic plaques are normally present along the vessel walls upstream and further downstream the bifurcations [93]. Using both experimental techniques of flow visualization and numerical simulations to investigate the flow field around atherosclerosis-susceptible

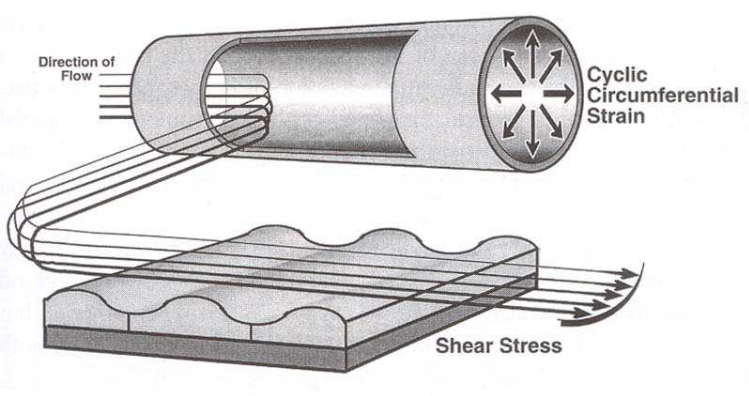

Figure 4: Schematic representation of the normal and tangential stresses acting on a blood vessel wall [86].

regions, flow separations, recirculations and flow reattachments have been observed within and downstream of vascular bifurcations. These observations led to the hypothesis that the characteristic mechanical environment acting on vascular cells at these specific locations could play a key role in determining many aspects of endothelial cell physiology and pathology. Since the mechanical conditions on endothelial cells are strongly dependent on the hemodynamic forces induced by the blood flow, an accurate knowledge of the interaction between the blood stream and the vascular endothelium is then considered fundamental to investigate the onset of various cardiovascular diseases.

As blood flows through a vessel, it exerts a physical force on the vessel wall. This force can be resolved into two principal vectors, respectively parallel and perpendicular to the vessel wall. Wall shear stress is defined as the portion of this force per unit surface parallel to the vessel wall. It represents the instantaneous frictional force exchanged by the blood flow and the endothelial surface of the vessel wall due to the no slip physical condition at their interface. An additional force per unit surface, perpendicular to the vessel wall, accounts for the blood pressure effects and for the normal component of the viscous stress tensor, as discussed in section 2.1.3. This situation is schematically represented in figure 4, where both normal and tangential

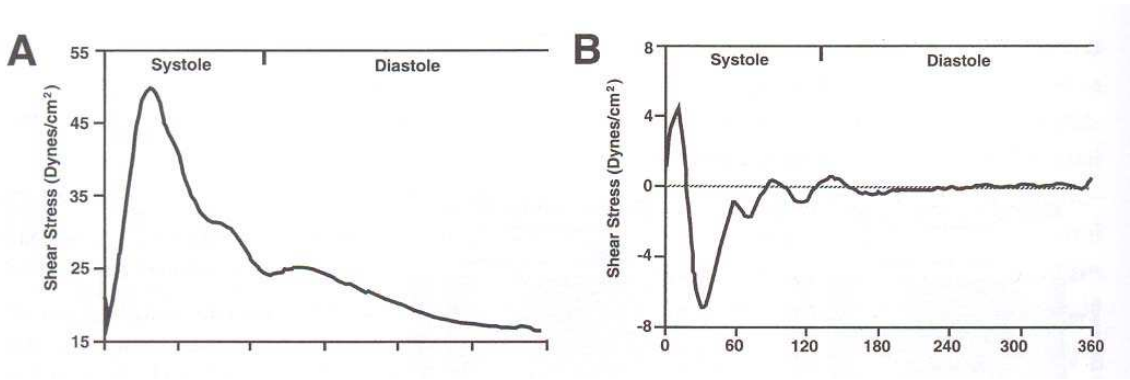

Figure 5: Wall shear stress temporal variations during the course of a cardiac cycle at two locations within the carotid bifurcation. (A) Inner flow-divider wall (B) Outer wall of the bifurcation, within the zone of recirculating flow [56].

stresses acting on a vessel wall are shown. Because of the cellular nature of blood, the dependence of its viscosity on the shear rate has been reported by many workers, showing that blood behaves as a non-Newtonian fluid [15, 30, 68]. Nevertheless, for blood stream in the macro-circulation, usually defined as blood vessels whose diameter is larger than $100\mu m$, it is recognized that the cellular elements do not affect the overall viscosity of blood, so that it can be considered as a Newtonian fluid [73, 14]. Given a Newtonian fluid with viscosity μ and tangential velocity $\mathbf{u}_t$ with respect to the wall normal vector $\mathbf{n}$, wall shear stress is calculated as

$$\boldsymbol{\tau}_w = \mu(\mathbf{n} \cdot \nabla)\mathbf{u}_t|_{wall} = \mu \frac{\partial \mathbf{u}_t}{\partial \mathbf{n}}|_{wall}$$

Blood flow in the cardiovascular system is pulsatile, causing the shear stress to vary throughout the cardiac cycle. Along much of the arterial tree, blood flow is stable and unidirectional and wall shear stress variations in time are always positive. Within these regions, endothelial cells are exposed to shear stresses on the order of 10 to 40 $dyne/cm^2$ [23]. By sensing and integrating hemodynamic stimuli, the endothelium in these regions plays a fundamental role in maintaining circulatory integrity and

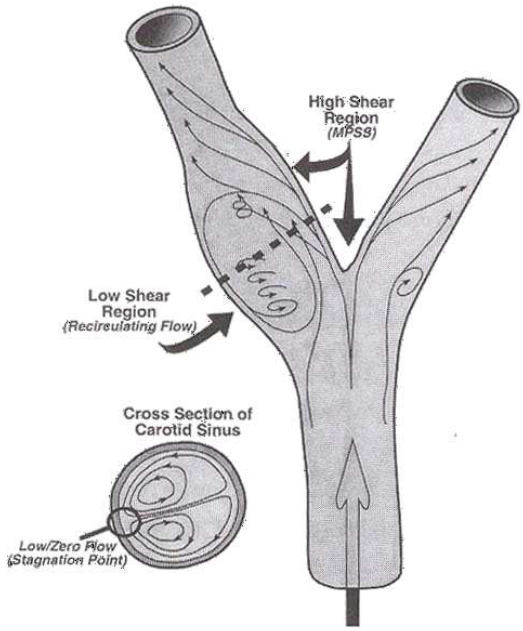

Figure 6: Flow patterns at the carotid bifurcation [56].

homeostasis. Although the mechanosensitive mechanism used by endothelial cells to sense hemodynamic forces and traduce those in biochemical signaling is still unclear, most lines of evidence are consistent with the atheroprotective role of mean positive wall shear stress. Endothelial cells respond to mean positive shear stress by releasing factors that inhibit coagulation, migration of leukocytes, and smooth muscle cell proliferation [86]. Moreover, different investigators have demonstrated that mean positive shear stress is required for optimal regeneration of injured endothelium [61].

In areas where the fluid mechanics is altered by geometry and curvature changes in the vasculature, such as around branch points and distal to stenoses, hemodynamic forces exerted upon the endothelium can be considerably different. At these locations, secondary flow patterns of separation, reattachment and recirculation tend to form. As a consequence, blood flow varies significantly in magnitude and direction throughout the cardiac cycle, and spatial gradients are accordingly high, as shown in figure 6. Given the pulsatile nature of blood flow, temporal gradients are also generated

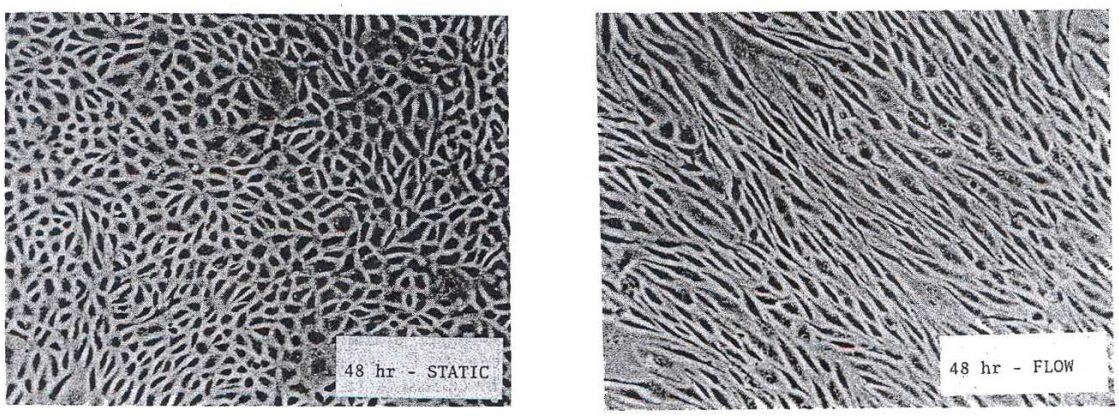

Figure 7: Shape change and orientation with flow in endothelial cells. (left) Static conditions (right) Imposed flow field [28].

throughout the entire vasculature, but they are magnified within recirculation areas. At this locations, maximal spatial and temporal wall shear stress gradients overlap each other, creating dynamically complicated blood flow patterns. An example of these abrupt temporal variations are shown in figure 5, where temporal variations in wall shear stress during a cardiac cycle are presented at two locations within the carotid bifurcation [56]. The geometry of the phantom used in both experimental and numerical simulations is presented in figure 6. The outer wall of the internal carotid branch, a site frequently affected by atherosclerotic plaques, is characterized by a region of recirculating flow with low value of mean shear stress and significant spacial and temporal shear stress gradients [101, 56]. Conversely, regions where plaque formation is typically very low, such as before the bifurcation and at the inner wall of the bifurcating branch, are characterized by linear and almost unidirectional flow field, with resulting higher values of mean wall shear stress.

From a morphological point of view, the endothelium also responds dynamically to different hemodynamic conditions, with endothelial cells geometry and surface topography being strongly affected by the blood flow. Within regions of relatively simple unidirectional flow, endothelial cells tend to align with their longitudinal axis parallel

to the flow direction [28]. Conversely, cells within areas with significant gradients in wall shear stress do not align with the flow and tend to assume a characteristic "cobblestone" shape [59, 61]. The two different morphologies are illustrated in figure 7. Accordingly, endothelial cells within recirculating areas have shown increased proliferation rate, a feature that is implicated in the process of atherogenesis [16]. Moreover, low shear stress around points of flow reattachment of recirculation areas could allow prolonged residence time for circulating pro-inflammatory particles to adhere to the endothelium [40].

Atherosclerosis dependency on different hemodynamic conditions was hypothesized in the 1960's and proved for the first time more than 20 years ago [101, 36]. Many other scientific reports trying to address this correlation have since been published, but the *in vivo* role of temporal and spatial wall shear stress gradients in atherogenesis remains unclear. Some investigators indicated the large temporal gradients in shear stress as the hemodynamic factor to promote atherosclerosis [56, 70], while others related it to spatial gradient distributions of mean wall shear stress [44]. Although it is not yet known what sensory machinery of the endothelial cells is involved in detecting fluid flow, it is now widely accepted that wall shear stress is the primary hemodynamic factor that is linked to atherosclerotic plaque localization.

Recent progresses in the development of micro-electro mechanical systems (MEMS) sensors to measure shear stress in the microcirculation [92, 83, 82] have greatly improved the performance traditionally provided by established techniques such as hot-wire anemometry and laser Doppler velocimetry. Unfortunately, despite these progresses, it is yet not possible to measure wall shear stress in vivo or in vitro with the precision needed. This explains why numerical simulations have become an essential tool to investigate the problem. Once the blood flow field is known from the CFD simulation, endothelial responses that are regulated at multiple levels of organization extending over scales from vascular beds to single cells, subcellular structures and

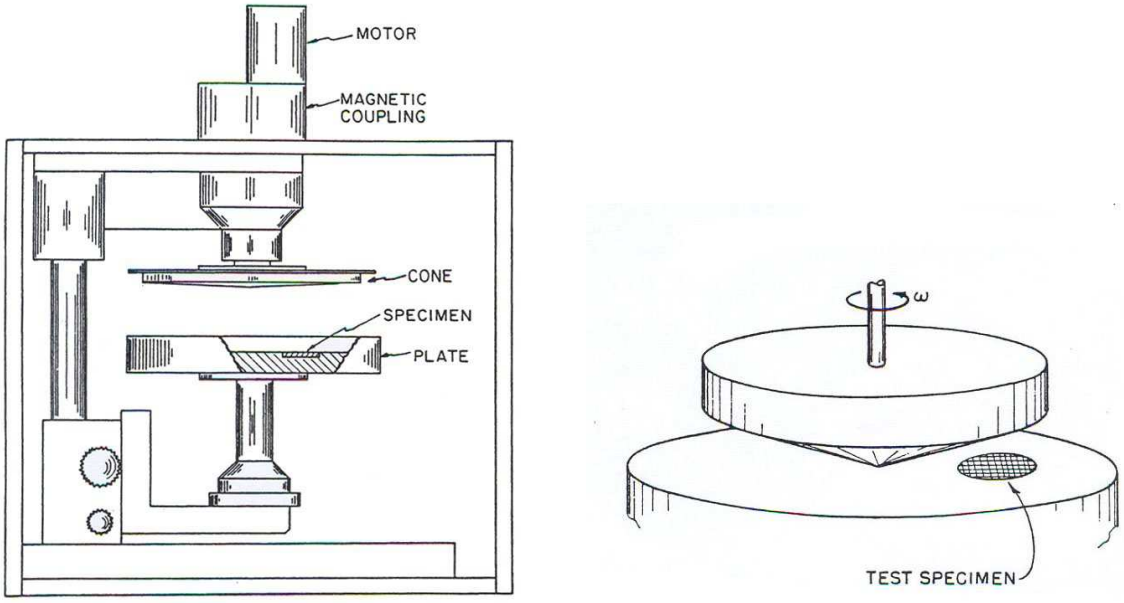

(a) **(b)**

Figure 8: Cone-and-plate shearing device [28]. (a) Overall view: for testing the plate is raised until a pre-defined gap is obtained from the apex of the rotating cone, (b) Positioning of the biological specimen.

individual molecules can be investigated. Insights have been lately obtained in understanding how surface topography of endothelial cells on the vascular bed responds to shear stress [71], how shear stress is distributed at both cellular and subcellular levels [26], and how these mechanical stimuli trigger different biochemical responses [9]. However, detailed quantitative descriptions of the involved mechanisms that are the origins of observed correlations are still missing.

The most widely used experimental apparatus to investigate endothelial cells response to shear stress *in vitro* is the so called cone-and-plate device [12, 28, 11]. As illustrated in figure 8, it consists of a cylindrical container (plate) coupled with a conical shaped cylinder (cone). The gap between the two is filled with a Newtonian biological media, usually the same used to culture the monolayer of endothelial cells (test specimen) present on the plate surface. When the cone is put under rotation, the

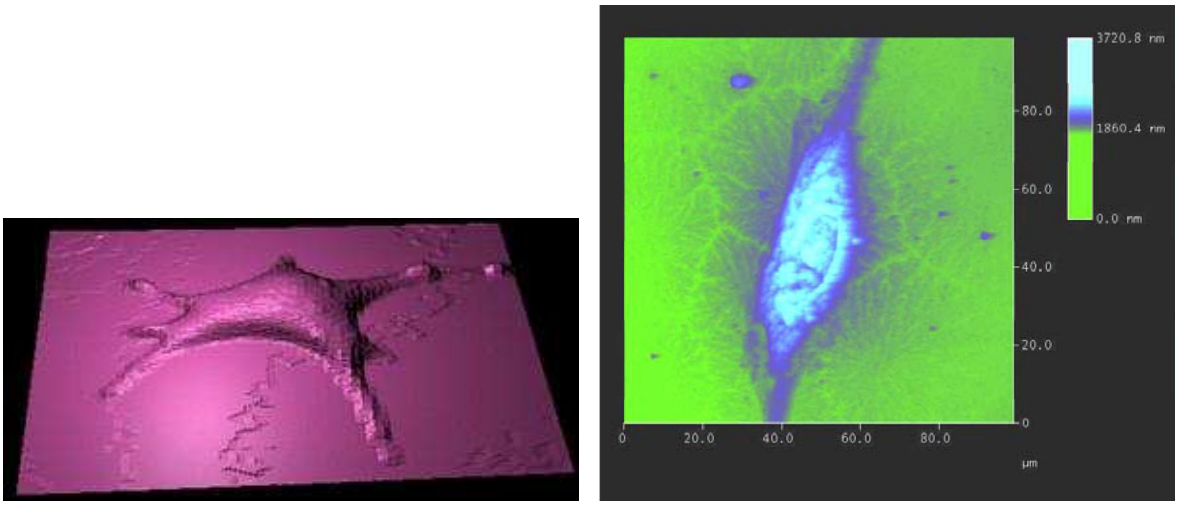

(a) **(b)**

Figure 9: Atomic force microscopy. (a) endothelial cell at rest, (b) endothelial cell aligned under a flow field.

media starts moving, creating a shearing force on the cells monolayer. After exposing the cells to a controlled flow field for a desired lapse of time, biochemistry experiments are performed on both the cells and the media to quantify the cells biological behavior under the imposed flow conditions. Fluid mechanics characteristics of the cone-and-plate device have been widely investigated using both numerical analyses and analytical approaches [19, 88, 6, 31], but only for geometrically and dynamically simplified configurations.

Following recent progress in digital imaging, there have been attempts to gain insights about *in vitro* single cell shape. Atomic force microscopy makes it possible nowadays to obtain a detailed description of the topography of cultured layers of endothelial cells. Examples of two different AFM scans are given in figure 9. The first image shows a single endothelial cell when no flow field is imposed on its surface. In the second picture the cell has been exposed to a uniform flow, and we can see that in response to the fluid mechanics environment the endothelial cell reorganizes its cytoskeleton structure to align along the flow field direction. Using the real shape

of the cells to implement numerical simulations provides the opportunity to compare the biochemistry response of the cells under different physiological and pathological flow conditions. Numerical analyses have already been attempted at a single cell level [84, 8, 85], but all of them were once again performed using simplified, not realistic configurations. An accurate knowledge of the shear stress distribution at the single cell level, simulating the real experimental configuration, would be essential to investigate the biological effects of the shearing force acting on the cells; the contribution of this thesis will be to try to fill this knowledge gap.

A specific aim of this thesis is, in fact, to develop a numerical code, based on an immersed boundary method (IBM) approach, capable of predicting the flow field in the cone-and-plate device, including the case of oscillatory flow. This aspect is crucially important, since only an unsteady flow can reproduce physiologically relevant conditions to be applied to endothelial cells cultured on the plate.

The spatial distribution of wall shear stress over endothelial cells may be important in mechanotransduction mechanism. The surface of endothelial cells is not uniform, and biological markers related to atherogenesis may have a local variation over the surface. Atomic force microscopy is used to obtain a detailed description of the endothelial cells surface topography, whose knowledge is essential to investigate how the flow field may affect the biological markers spatial distribution. Imposing specific waveforms to the cone rotation, numerical simulations are performed on the endothelial layer under different flow conditions. The computed velocity fields are analyzed, and a high resolution description of the wall shear stress fields over the cells surface in response to the imposed mechanical environments are obtained. A detailed flow field computation represents a great opportunity to gain a qualitative correlation between the specific wall shear stress distribution over the surface and many of the qualitatively observed biological behaviors typical of endothelial cells under controlled experimental conditions.

In addition, the developed CFD code is capable of handling two different fluids in the same flow field. For instance, the single endothelial cell could be modeled as a fluid inside a membrane, to see how its shape changes under different flow conditions. The detailed formulation of this latter problem, however, is beyond the scope of this thesis.

CHAPTER II

FLUID DYNAMICS BACKGROUND

2.1 A Brief Review

Computational fluid dynamics has long been an important tool to predict flow patterns in the cardiovascular system. Capitalizing on the great advances in the image processing field, it has been possible to perform simulations based on physiological geometries and boundary conditions obtained from in vivo measurements. Moreover, numerical simulations of the flow field over biological tissues cultured in vitro have been performed. This tool has provided the opportunity to gain a better understanding into the biochemical effects produced by forces exerted on a cell by the surrounding flow field.

2.1.1 Governing equations of fluid mechanics

The motion of a fluid is governed by the *conservation laws of mass and momentum*. These can be expressed in their integral form by

$$\begin{cases} \displaystyle\int_V \frac{\partial \rho}{\partial t} dV - \oint_S \rho \mathbf{u} \cdot \mathbf{n} dS = 0 \\ \\ \displaystyle\int_V \frac{\partial}{\partial t}(\rho \mathbf{u}) dV + \oint_S \rho \mathbf{u}(\mathbf{u} \cdot \mathbf{n}) dS = -\oint_S p \mathbf{n} dS + \oint_S \mathbb{S} \cdot \mathbf{n} dS + \int_V \rho \mathbf{f} dV \end{cases} \tag{1}$$

where $\mathbf{n}$ represents the outward normal from the closed surface S enclosing the arbitrary volume V, $\mathbf{f}(\mathbf{x}, t)$ is the force per unit mass due to any external field (e.g., gravity) and $\mathbb{S}$ the *viscous stress tensor*. The unknowns of the system are the density

$\rho(\mathbf{x}, t)$, the pressure $p(\mathbf{x}, t)$ and the velocity $\mathbf{u}(\mathbf{x}, t)$, but the system consists of a vectorial equation and a scalar one. We then need one more equation to have the same number of equations and unknowns. The additional scalar equation is represented by the *conservation law of energy*. Unfortunately, this equation contains two additional unknowns, the specific energy e and the temperature T. Then, considering for example the case of a fluid with a single stable chemical species, we have to include other two *equations of state* giving the relationship between the thermodynamic variables, such as

$$\begin{cases} p = p(e, \rho) \\ \\ T = T(e, \rho) \end{cases} \tag{2}$$

The form of these equations, called *constitutive equations* of the fluid, depends on the thermodynamic properties of the fluid (liquid or gas). In the most general case of a compressible viscous fluid, the energy equation is very complicated because of the complexity of the terms describing the increase in internal energy due to viscous effects. In the simpler case of an incompressible fluid, the density is considered constant. The conservation equations for mass and momentum can then be decoupled from the energy equation, leading to a mathematical system of two equations (one scalar and one vectorial) in four unknowns. For an incompressible Newtonian fluid the *viscous stress tensor* can be expressed as

$$\mathbb{S}(\mathbf{u}) = 2\mu\mathbb{E}(\mathbf{u}) \tag{3}$$

where μ is the dynamic viscosity and $\mathbb{E}$ represents the *rate of strain tensor* whose components are

$$e_{i,j}(\mathbf{u}) = \frac{1}{2}\left(\frac{\partial u_j}{\partial x_i} + \frac{\partial u_i}{\partial x_j}\right) \tag{4}$$

The simplified system of equations for an incompressible Newtonian fluid then becomes

$$\begin{cases} \oint_S \mathbf{u} \cdot \mathbf{n} dS = 0 \\ \\ \int_V \frac{\partial \mathbf{u}}{\partial t} dV + \oint_S \mathbf{u}(\mathbf{u} \cdot \mathbf{n}) dS = -\frac{1}{\rho} \oint_S p\mathbf{n} dS + \frac{1}{\rho} \oint_S 2\mu \mathbb{E}(\mathbf{u}) \cdot \mathbf{n} dS + \int_V \mathbf{f} dV \end{cases} \tag{5}$$

Applying the divergence theorem to the integral form of the mass and momentum conservation laws, we obtain the well known Navier Stokes equations for an incompressible fluid

$$\begin{cases} \nabla \cdot \mathbf{u} = 0 \\ \\ \frac{\partial \mathbf{u}}{\partial t} + (\mathbf{u} \cdot \nabla)\mathbf{u} = -\frac{\nabla p}{\rho} + \nu \nabla^2 \mathbf{u} + \mathbf{f} \end{cases} \tag{6}$$

where ν represents the coefficient of kinematic viscosity of the fluid, given by the dynamic viscosity divided by the density.

Initial and Boundary Conditions

The Navier Stokes equations are a set of partial differential equations that by themselves do not represent a complete mathematical problem. The statement of the problem is made complete by the specification of suitable boundary and initial conditions. A typical boundary condition consists of prescribing the value of the velocity field $\mathbf{b}$ on the boundary,

$$\mathbf{u}|_S = \mathbf{b}(\mathbf{x}_S, t) \tag{7}$$

where $S = \partial V$ is the boundary of the domain and $\mathbf{b}$ is the velocity specified on S and $\mathbf{x}_S \in S$. When the boundary is a solid wall in contact with the fluid, the boundary value $\mathbf{b}$ is equal to the velocity of the wall. The condition on the tangential components of velocity is known as the *no-slip condition*. It is important to note that no boundary condition is prescribed for the pressure on no-slip boundaries and that it

would be incorrect to specify one together with the velocity boundary condition (7). On the other hand, when velocity conditions different from (7) are encountered, such as on inflow or outflow boundaries and on a plane of symmetry or anti symmetry, the pressure can be supplemented by boundary conditions of a Dirichlet or Neumann type.

The initial condition consists in the specification of the velocity field $\mathbf{u}_0$ at the initial time, t=0, namely,

$$\mathbf{u}|_{t=0} = \mathbf{u}_0(\mathbf{x}) \tag{8}$$

In the viscous incompressible problem, initial and boundary conditions have to be linked together. Since at any instant of time the conservation of mass enforces a solenoidal flow field, the initial velocity $\mathbf{u}_0$ must satisfy the *compatibility condition*

$$\nabla \cdot \mathbf{u}_0 = 0 \tag{9}$$

Moreover, integrating on the boundary surface S the normal component of the velocity $\mathbf{b}(\mathbf{x}_S, t)$ prescribed on the boundary itself, we obtain

$$\oint_S \mathbf{u}_{|S} \cdot \mathbf{n} dS = \oint_S \mathbf{b}(\mathbf{x}_S, t) \cdot \mathbf{n} dS \tag{10}$$

at any instant of time $t > 0$. Applying the divergence theorem we get

$$\int_V \nabla \cdot \mathbf{u}(\mathbf{x}, t) dV = \oint_S \mathbf{b}(\mathbf{x}_S, t) \cdot \mathbf{n} dS \tag{11}$$

but the velocity field must be solenoidal at any instant of time, so that the first integral is zero and thus

$$\oint_S \mathbf{b}(\mathbf{x}_S, t) \cdot \mathbf{n} dS = 0 \tag{12}$$

for any $t > 0$. This represents a *global compatibility condition* that the normal component of the prescribed velocity at the boundary must satisfy to ensure the incompressibility condition at any instant of time. Finally, for stationary flows, there are no initial conditions and the value of the velocity boundary conditions does not depend on the time. We then remain with

$$\oint_S \mathbf{b}(\mathbf{x}_S) \cdot \mathbf{n} dS = 0 \tag{13}$$

2.1.2 Numerical methods

Coming to the numerical solution of the conservation laws of mass and momentum (in both the integral and differential forms) for an incompressible Newtonian fluid, a serious difficulty is met in the determination of the pressure field and in the fulfillment of the incompressibility condition. In fact, the continuity equation is somewhat particular in that it represents a constraint on the velocity field. At the same time the pressure variable, which appears in the momentum equation, provides the degrees of freedom necessary to accommodate and satisfy such a constraint. Correspondingly, no evolutionary equation exists for the pressure, so that in incompressible problems this variable has not the usual thermodynamic meaning. Here, the role of the pressure is that of adjusting itself instantaneously in order for the divergence free condition to be satisfied at any instant of time. This behavior is related to the fact that in an incompressible fluid the value of the speed of sound becomes infinite. As a consequence, the pressure field cannot be calculated by an explicit time-advancement procedure but requires instead an implicit determination able to take into account the coupling existing between the pressure and the velocity, as well as the effect of the velocity boundary condition. This aspect can be considered the most distinctive feature of the primitive variable formulation of the incompressible conservation laws

of mass and momentum.

Methods for the approximate solution of the governing equations of fluid mechanics have been investigated rather extensively in the last three decades. Several numerical schemes have been developed for computing both steady and unsteady viscous flows using different mathematical formulations of the problem. An important aspect of the numerical methods for solving this class of problems is the proper specification of the boundary conditions, especially in the presence of solid walls. Of course, the treatment depends on the variables chosen as unknowns and, from a numerical viewpoint, the specific form assumed by the boundary conditions may also depend on the method adopted for the spatial and temporal discretizations.

It is important to distinguish between the different forms of equations described above, because each of them has been used to develop different numerical methods. Finite element and finite volume methods typically employ the integral form of the conservation laws, while finite differences methods are based on the differential Navier Stokes equations. Each of these discretization methods can then be coupled to various numerical schemes. Here, we only review the finite volume method associated to the fractional step - projection method, which has been used in the development of our CFD code. Other methods and discretization techniques can be found in the literature.

Finite volume discretization

The finite volume method is based on the integral form of the conservation laws for mass and momentum. The integral conservation law is enforced on small control volumes V_i defined by the computational mesh

$$V = \bigcup_{i=1}^{N} V_i, \qquad V_i \bigcap V_j = \emptyset, \qquad \forall i \neq j \tag{14}$$

Pressure and velocity are defined at the center of each of these control volumes as the average value in the cell itself

$$\phi_i = \frac{1}{|V_i|} \int_{V_i} \phi dV \tag{15}$$

Because the flux entering a given volume is identical to that leaving the adjacent volume, finite volume methods are fully conservative.

Fractional step methods

The fractional step methods, also called projection methods, were first introduced by Chorin [17] and Temam [94] in 1968. They are based on the observation that in incompressible viscous flows pressure does not retain any thermodynamic meaning and it represents the Lagrange multiplier associated with the incompressibility constraint. Because of this fact, projection methods are used to decouple the computation of velocity and pressure. Fractional-step methods have been repeatedly considered in CFD literature and several implementations have been proposed using spatial discretizations based on finite difference, finite elements or spectral methods. All of these schemes start from the same idea. In the first step, an intermediate velocity field is computed using an incomplete momentum equation. In the second step the intermediate velocity is projected into a divergence free vector space, as required by the continuity equation. These schemes differ in that the momentum equation is solved differently in the first step. Considering schemes based on finite difference discretization and using the categorization proposed by Gresho [41], the most widely used versions are labeled as P1 and P2. In the P1 method the pressure term is set to zero in the momentum equation, and the Poisson equation is then solved for the pressure at the new instant of time. In the P2 method the pressure is set in the momentum equation to the value computed at the previous instant of time, and then the Poisson

equation is solved for the incremental pressure at the new time step. Considering for simplicity a time stepping algorithm with an implicit discretization for the viscous term and explicit for the advection term, the first step in the P1 version is

$$\frac{\mathbf{u}^* - \mathbf{u}^n}{\Delta t} + (\mathbf{u}^n \cdot \nabla)\mathbf{u}^n = \nu \nabla^2 \mathbf{u}^* \tag{16}$$

Then the terms omitted from the momentum equation in the first step must be solved together with the continuity equation

$$\begin{cases} \dfrac{\mathbf{u}^{n+1} - \mathbf{u}^*}{\Delta t} + \dfrac{1}{\rho}\nabla p^{n+1} = 0 \\ \\ \nabla \cdot \mathbf{u}^{n+1} = 0 \end{cases} \tag{17}$$

Taking the divergence of the first equation and using the fact that the field of $\mathbf{u}^{n+1}$ is divergence free we obtain the Poisson equation for pressure

$$\nabla^2 p^{n+1} = \frac{\rho}{\Delta t} \nabla \cdot \mathbf{u}^* \tag{18}$$

Once the pressure at the n+1 instant of time is computed, the value of the intermediate velocity can be updated using the first equation in (17)

$$\mathbf{u}^{n+1} = \mathbf{u}^* - \frac{\Delta t}{\rho}\nabla p^{n+1} = 0 \tag{19}$$

This method is very efficient if compared to the straightforward time discretization solution of the coupled Navier Stokes equations. The drawback is represented by the presence of a numerical boundary layer on pressure and velocity fields. Because of this, specification of boundary conditions represents an essential aspect of the problem, since the use of bad boundary conditions could pollute the solution in the entire domain. Using periodic boundary conditions the accuracy of the method can be easily

analyzed [18]. When more physical boundary conditions such as no slip boundary conditions are used, it becomes more difficult to prove the accuracy of the numerical scheme, although convergence has been proved in [18]. In a very similar fashion, the P2 method solves the momentum equation using the pressure field calculated at the previous instant of time

$$\frac{\mathbf{u}^* - \mathbf{u}^n}{\Delta t} + (\mathbf{u}^n \cdot \nabla)\mathbf{u}^n = -\nabla p^n + \nu \nabla^2 \mathbf{u}^* \tag{20}$$

and the Poisson equation is then solved for the incremental value of the pressure $\delta p = p^{n+1} - p^n$

$$\nabla^2 \delta p = \frac{\rho}{\Delta t} \nabla \cdot \mathbf{u}^* \tag{21}$$

The divergence free velocity is then calculated using

$$\mathbf{u}^{n+1} = \mathbf{u}^* - \frac{\Delta t}{\rho} \nabla \delta p = 0 \tag{22}$$

In this case physical boundary conditions can be used on the intermediate velocity field, since the intermediate velocity still satisfies the momentum equation. Boundary conditions for the pressure in the projection step still represent a problem. This delicate issue will be discussed later on. Shen [89, 90] recently proved convergence with some error estimates for different versions of the projection methods using different boundary conditions. Despite these publications, there are still controversies with regard to the optimal choice of boundary conditions for the fractional step method [42, 5, 3, 4].

2.1.3 Shear stress

In equation 3 we defined the viscous stress tensor $\mathbb{S}(\mathbf{u})$ for an incompressible Newtonian fluid as twice the product of its dynamic viscosity μ times the rate of stress tensor $\mathbb{E}(\mathbf{u})$. The viscous stress vector on a generic surface point $\mathbf{P}$ can be calculated as the dot product of the viscous stress tensor and the unit vector normal to the plane $\boldsymbol{T}$ tangent to the surface at $\mathbf{P}$

$$\mathbf{s}_n(\mathbf{u}) = \mathbb{S}(\mathbf{u}) \cdot \mathbf{n} = 2\mu\mathbb{E}(\mathbf{u}) \cdot \mathbf{n} \tag{23}$$

Shear stress is thus defined as the projection of this vector on the plane $\boldsymbol{T}$. Recalling the definition of $\mathbb{E}(\mathbf{u})$ given in equation 4, the viscous stress vector components along the three Cartesian directions can be written as

$$\mathbf{s}_n(\mathbf{u}) = 2\mu \begin{bmatrix} \dfrac{\partial u}{\partial x} n_x + \dfrac{1}{2}\left(\dfrac{\partial u}{\partial y} + \dfrac{\partial v}{\partial x}\right) n_y + \dfrac{1}{2}\left(\dfrac{\partial u}{\partial z} + \dfrac{\partial w}{\partial x}\right) n_z \\ \dfrac{1}{2}\left(\dfrac{\partial u}{\partial y} + \dfrac{\partial v}{\partial x}\right) n_x + \dfrac{\partial v}{\partial y} n_y + \dfrac{1}{2}\left(\dfrac{\partial v}{\partial z} + \dfrac{\partial w}{\partial y}\right) n_z \\ \dfrac{1}{2}\left(\dfrac{\partial u}{\partial z} + \dfrac{\partial w}{\partial x}\right) n_x + \dfrac{1}{2}\left(\dfrac{\partial v}{\partial z} + \dfrac{\partial w}{\partial y}\right) n_y + \dfrac{\partial w}{\partial z} n_z \end{bmatrix} \tag{24}$$

We now want to express the viscous stress vector in a slightly different way that will be more convenient for implementation in our computational code. The mathematics involved in this 3D process is very tedious. We will then avoid to report it, presenting a simplified 2D version of it. Once solved, it will be straightforward to extend it to the original 3D case. The viscous stress vector in two dimensions is given by

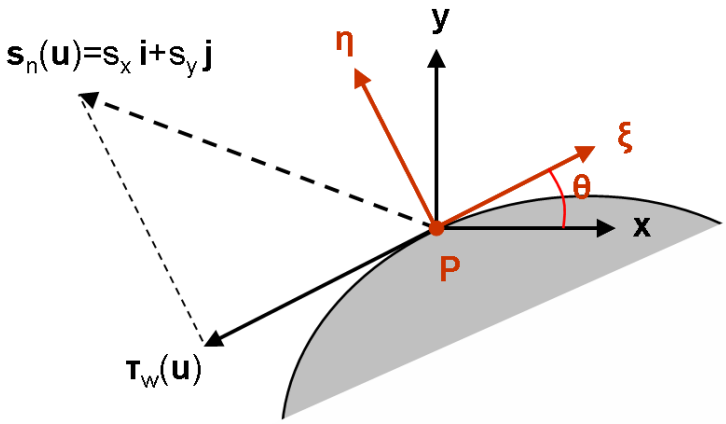

Figure 10: The shear stress in **P** can be considered as the projection of the viscous stress vector on the axis ξ of the new curvilinear coordinate systems.

$$\mathbf{s}_n(\mathbf{u}) = 2\mu \begin{bmatrix} \dfrac{\partial u}{\partial x} n_x + \dfrac{1}{2}\left(\dfrac{\partial u}{\partial y} + \dfrac{\partial v}{\partial x}\right) n_y \\ \\ \dfrac{1}{2}\left(\dfrac{\partial u}{\partial y} + \dfrac{\partial v}{\partial x}\right) n_x + \dfrac{\partial v}{\partial y} n_y \end{bmatrix} \tag{25}$$

Let's define a new Cartesian coordinate system (ξ, η) that has its origin at **P** and whose η axis is perpendicular to that surface itself. The ξ axis will accordingly lay on **T**. Following the conventions in figure 10, the rotation matrix describing the change of coordinate system is

$$\begin{Bmatrix} x \\ y \end{Bmatrix} = \begin{bmatrix} cos\theta & -sin\theta \\ sin\theta & cos\theta \end{bmatrix} \begin{Bmatrix} \xi \\ \eta \end{Bmatrix} \tag{26}$$

As a consequence, we can express the normal components of **n** along the x and y axes in terms of the angle θ as

$$\mathbf{n} = \begin{Bmatrix} n_x \\ n_y \end{Bmatrix} = \begin{bmatrix} cos\theta & -sin\theta \\ sin\theta & cos\theta \end{bmatrix} \begin{Bmatrix} n_\xi \\ n_\eta \end{Bmatrix} = \begin{Bmatrix} -sin\theta \\ cos\theta \end{Bmatrix} \tag{27}$$

being $n_\xi = 0$ and $n_\eta = 1$. Using the chain rule, we can also write the velocity derivatives present in equation (25) as a function of their derivatives along the ξ and η axes

$$\begin{cases} \dfrac{\partial \phi}{\partial x} = \dfrac{\partial \phi}{\partial \chi} \cdot \dfrac{\partial \xi}{\partial x} + \dfrac{\partial \phi}{\partial \eta} \cdot \dfrac{\partial \eta}{\partial x} = \phi_\xi cos\theta - \phi_\eta sin\theta \\ \\ \dfrac{\partial \phi}{\partial y} = \dfrac{\partial \phi}{\partial \chi} \cdot \dfrac{\partial \xi}{\partial y} + \dfrac{\partial \phi}{\partial \eta} \cdot \dfrac{\partial \eta}{\partial y} = \phi_\xi sin\theta + \phi_\eta cos\theta \end{cases} \tag{28}$$

Due to the no slip viscous condition on the solid boundary, all of velocities partial derivatives with respect to the $\xi - axis$ will vanish

$$\frac{\partial \phi}{\partial \xi} = 0 \qquad \phi = u, v \tag{29}$$

Considering the above conditions, we can then write

$$\begin{cases} \dfrac{\partial u}{\partial x} = u_\eta n_x & \dfrac{\partial v}{\partial x} = v_\eta n_x \\ \\ \dfrac{\partial u}{\partial y} = u_\eta n_y & \dfrac{\partial v}{\partial y} = v_\eta n_y \end{cases} \tag{30}$$

Using these identities, our viscous stress vector becomes

$$\mathbf{s}_n(\mathbf{u}) = 2\mu \begin{bmatrix} \dfrac{\partial u}{\partial \eta} n_x^2 + \dfrac{1}{2}\left(\dfrac{\partial u}{\partial \eta} n_y + \dfrac{\partial v}{\partial \eta} n_x\right) n_y \\ \\ \dfrac{1}{2}\left(\dfrac{\partial u}{\partial \eta} n_y + \dfrac{\partial v}{\partial \eta} n_x\right) n_x + \dfrac{\partial v}{\partial \eta} n_y^2 \end{bmatrix} \tag{31}$$

Shear stress at $\mathbf{P}$ was defined as the projection of this vector on the plane $\boldsymbol{T}$, that in this 2D case is represented by the ξ direction. We then conclude that

$$\tau_w = \mathbf{s}_n(\mathbf{u}) \cdot \boldsymbol{\xi} = \mathbf{s}_n(\mathbf{u}) \cdot \begin{bmatrix} n_y \\ -n_x \end{bmatrix} \tag{32}$$

and after some maths we end up with

$$\tau_w = \mu \left(\frac{\partial u}{\partial \eta} n_y - \frac{\partial v}{\partial \eta} n_x \right) \tag{33}$$

It is now clear that this formula represents the directional derivative of the velocity vector along the normal to the solid surface at $\mathbf{P}$ projected on the tangent $\boldsymbol{T}$ plane, expressed mathematically as

$$\boldsymbol{\tau}_w = \mathbf{s}_n(\mathbf{u}) - \mathbf{s}_n(\mathbf{u})_\perp = \mu \frac{\partial \mathbf{u}}{\partial \mathbf{n}}\bigg|_{wall} - \left(\mu \frac{\partial \mathbf{u}}{\partial \mathbf{n}}\bigg|_{wall} \cdot \mathbf{n} \right) \mathbf{n} \tag{34}$$

As already anticipated, this formulation will be useful in the numerical evaluation of the shear stress field on our immersed solid interfaces. We can visualize this result looking at the simple case, when the solid surface is perpendicular to the z-axis at $\mathbf{P}$: as a consequence, we will have $\mathbf{n} = (0, 0, 1)$. Considering this *ad hoc* situation, we do not need any fictitious change of coordinate system, and the viscous stress vector in equation 24 becomes

$$\mathbf{s}_n(\mathbf{u}) = \mu \left[\left(\frac{\partial u}{\partial z} + \frac{\partial w}{\partial x} \right), \left(\frac{\partial v}{\partial z} + \frac{\partial w}{\partial y} \right), 2\frac{\partial w}{\partial z} \right] \tag{35}$$

No slip conditions on the solid wall imply that the partial derivative of any velocity component along the x and y directions must be zero. After simplifications, the formula for the wall shear stress vector becomes

$$\boldsymbol{\tau}_w = \mu \left[\frac{\partial u}{\partial z}, \frac{\partial v}{\partial z}, 0 \right] \tag{36}$$

Using the tangential velocity $\mathbf{u}_t$ with respect to the wall normal vector $\mathbf{n}$, wall shear stress can also be expressed in an equivalent way as

$$\boldsymbol{\tau}_w = \mu(\mathbf{n} \cdot \nabla)\mathbf{u}_t|_{wall} = \mu \frac{\partial \mathbf{u}_t}{\partial \mathbf{n}}\bigg|_{wall} \tag{37}$$

a formula already anticipated in the introduction chapter.

2.2 Related work in literature

2.2.1 cone-and-plate device

By far the most common use for the rotating cone-and-plate configuration has been in viscosimetry. This device was first introduced by Mooney [69] in 1934 and provides viscosity data for fluids with various stress-strain relations. Characteristic of this experimental device compared to other types of viscometers was found to be a constant shear stress throughout the fluid sample, provided the cone angle and the gap between the cone and the plate are sufficiently small. About 30 years later, Cox [21] first observed secondary flow phenomena using dye visualization techniques. Pelech [74] first identified the ratio of the fluid centrifugal forces to viscous forces as the parameter governing secondary fluid motion in the cone-and-plate device, following the work of Slattery [91] where he pointed out the conditions under which secondary flow can be neglected. From that time on, many approaches have been proposed to elucidate the effect of secondary flow on the overall flow field. Using an expansion of the Navier-Stokes equations, Sdougos [88] presented an analytical solution of the flow field in the cone-and-plate device for a Newtonian fluid. For low rotational speeds, these results were in good agreement with experimental measurements performed

using hot film heat-transfer probes. These results were confirmed by Dudgeon [31] using laser doppler velocimetry (LDV). Flow profiles were also measured by Dudgeon in a misaligned geometry in which the cone axis of rotation is slightly tilted off the perpendicular with the plate surface. Only recently, some works were presented to obtain a solution for the flow field in the cone-and-plate device for unsteady flow. Chung [19] described the flow analytically using a perturbation method in terms of the Womersley and Reynolds numbers, which respectively account for the local unsteadiness of the flow field and for the effect of the viscosity. Buschmann [11] provided a numerical solution for the flow field in the device (but with a simpler geometry) for both an oscillating and a pulsating case, showing that there is a small region on the plate surface where, although the shear stress periodically changes in time, it can be considered nearly constant in space.

2.2.2 Fluid mechanics on endothelial cells

About 20 years ago, Bussolari [12] designed and used for the first time a cone-and-plate device to expose cultured endothelial cells to a controlled hemodynamic environment. This in-vitro system did not attempt to reproduce precisely the flow experienced by vascular endothelium in vivo, but still represented a valuable tool in the examination of the effects on cells of fluid shear stress in combination with other variables, such as time of exposure and fluid composition. Using the cone-and-plate experimental device, Dewey [28] observed a time dependent change in cell shape when a confluent monolayer of cultured endothelial cells is exposed to constant shear stress, in contrast to the static case. About 10 years later, Satcher [85] used linear perturbation theory to calculate the flow field over a wavy surface which approximates a monolayer of vascular endothelial cells exposed to a unidirectional flow. He also performed a numerical analysis on the same geometry, and the two results he obtained

were in good agreement although they diverged as the amplitude of surface undulation was increased. Barbee [8] performed a similar work using a periodic surface topology obtained from atomic force microscopy. He observed a reorganization of the endothelial surface in response to prolonged exposure to steady flow, causing a reduction in the computed average peak shear stress per cell. However, the range of shear stresses was similar for the aligned and the non-aligned cells, expressing values between $0.5\tau_{w\_no\_cells} < \tau_w < 1.5\tau_{w\_no\_cells}$, where $\tau_{w\_no\_cells}$ represents the shear stress value experienced by the substrate when no cells were present. Additionally, Yamaguchi [99] designed a self-perturbing model with a 3D configuration resembling cultured endothelial cells in order to investigate their morphology under different shear stress loading conditions. He showed how endothelial cells change their shape and arrangement in order to keep the highest wall shear stress within a physiological range. A detailed description of the shear stress distribution over the surface of a single endothelial cell as a function of the flow direction was also attempted by Sakurai and Yamaguchi [84, 99]. They described how the slope of the cell surface greatly affects the shear stress distribution, obtaining for their specific geometry peak values up to ten times higher than the lowest shear stress computed at any point on the individual cell surface. While all of the studies mentioned above have been carried on using steady unidirectional flows, biological experiments in the cone-and-plate shearing device are often performed under oscillatory flows. To our knowledge, no research on the time-dependent wall shear stress distribution over a cells layer subjected to unsteady flow has been published.

In the last decade, the hemodynamic environment over the endothelium has been suggested to be responsible for various biological functions, such as cellular and subcellular force transmission, cytoskeleton displacement and reorganization, initiation of molecular mechanisms of mechano-transduction, microstimuli at adhesion sites and cell-cell junctions, and chemical signaling [71, 26]. However, the specific mechanisms

mediating the cellular responses to different flow conditions have not been yet identified, and many studies have been recently performed trying to address these issues [26, 23, 25, 24, 45]. Of particular interest for this work, at Emory University, Dr. Jo's research group extensively uses the cone-and-plate device [51] to investigate how chronic shear stress stimulates caveolae formation by translocating caveolin-1 from the Golgi to the luminal plasma membrane and alters cell signaling responses [9]. A close collaboration with Dr. Jo's laboratory may then allow them to gain a deeper understanding on how these mechano-transduction mechanisms are dependent on the hemodynamic environment on a microscale level.

CHAPTER III

HYPOTHESIS AND SPECIFIC AIMS

The relationship between blood flow, mechanotransduction and the localization of arterial lesions is becoming a central topic in the ongoing investigation on the biology of the endothelium. Over the past decades, wall shear stress acting on the arterial walls has been observed to play a key role in the physiological and pathological behavior of the endothelium, and qualitative relationships with many of the biological and biochemical processes occurring at the single cell level have been hypothesized. In order to investigate these processes on a more quantitative basis, a detailed description of the fluid dynamics acting on the endothelium surface at a subcellular scale is needed.

Endothelial cells have a characteristic length of the order of microns, while the cone-and-plate shearing device used for the biological experiments on the endothelium has a size of the order of millimeters. From a numerical viewpoint, incorporating the two different length scales in the same computation may cause instability problems of the solution. This feature must be incorporated in the numerical grid, representing a challenging aspect of the entire numerical setup.

Another aspect that must be considered in the simulation of the flow field over an endothelial layer is represented by the heterogeneity of the cells surface topography. A computational code capable of dealing with different endothelial geometries without the need of modifying the computational mesh is considered a particular feature of this work. A new numerical approach to handle the treatment of a generic boundary surface is thus needed in the implementation of the developed CFD code.

Hypothesis

The immersed boundary approach can be employed to model the flow field over a group of endothelial cells in a cone-and-plate shearing device with a high degree of precision, and it will be able to determine shear stress variations over individual cells in order to elucidate mechano-transduction mechanisms.

Specific Aims

1. Develop a CFD code based on the finite volume approach. The code must be capable of dealing with complicated geometries without the need of changing the computational grid over time. Validate the code using benchmark solutions to standard test problems.

2. Use the CFD code to analyze the flow field over a group of endothelial cells in the cone-and-plate shearing device. Simulate the flow field for both steady and unsteady regimes imposed in standard biological experiments.

CHAPTER IV

METHODS

4.1 CFD code description

Our finite volume discretization refers to brick-shaped control volumes surrounding each node of an orthogonal Cartesian grid. The code allows us to construct non-uniform grids along each of the three Cartesian directions. Velocity and pressure are defined at the center of each control volume in a non-staggered fashion. Every time velocities or pressure are needed at a control cell surface, their values are computed using a weighted average function, obtaining second order accuracy in space for both uniform and non-uniform grids. As shown in figure 11, the value of a general variable ϕ at a cell border is given by

$$\varphi_{cb} = \frac{dx_i}{dx_i + dx_{i+1}}\varphi_{i+1} + \frac{dx_{i+1}}{dx_i + dx_{i+1}}\varphi_i + O(dx_i \cdot dx_{i+1}) \tag{38}$$

Similarly, in order to discretize our governing equations, we will need to evaluate velocity and pressure partial derivatives at each cell border. Specifically, these operators will only need to be computed along the direction perpendicular to the considered cell surface. As an example, referring again to figure 11, this is accomplished by

$$\left.\frac{\partial\varphi}{\partial x}\right|_{cb} = \frac{\varphi_{i+1} - \varphi_i}{dx_i + dx_{i+1}} + O\left(\frac{dx_{i+1}^2 - dx_i^2}{dx_{i+1} + dx_i}\right) = \begin{cases} \text{II } order & dx_{i+1} = dx_i \\ \\ \text{I } order & dx_{i+1} \neq dx_i \end{cases} \tag{39}$$

This approximation results second order accurate in space when evaluated on an uniform grid, but only first order in case of a non-uniform grid.

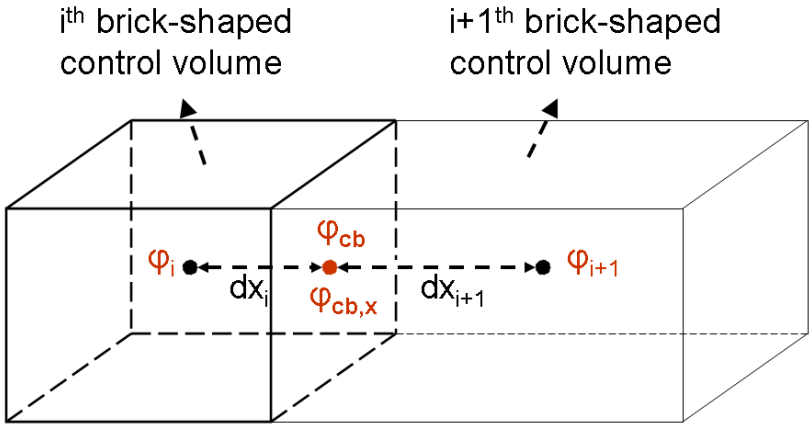

Figure 11: Control volume representation. The value of a generic variable φ and its derivative φ_x along the i-axis direction at the cell border (cb) will be calculated interpolating the values of the variable at the centers of the adjacent cells.

4.1.1 Pre-processing and immersed boundary theory

Since we work on a Cartesian orthogonal grid, our computational domain is represented by a parallelepiped. To simulate any flow field inside a more complex shaped domain, we need to introduce this new geometry inside our computational mesh.

Various techniques to simulate the fluid/structure interaction that dominates the overall flow field have been developed, posing a formidable challenge from a computational viewpoint. In recent years, non-boundary conforming numerical methods [37] are becoming increasingly attractive as compared to the classical boundary-fitted techniques based on the so-called Arbitrary Lagrangian Eulerian (ALE) approach [48]. Non-boundary conforming methods do not require the mesh to conform to the body, allowing the governing equations to be solved on a fixed Cartesian grid. In these methods, the effect of any solid body immersed in the flow field is taken into account by the imposition of suitable boundary conditions at some specific points on the Cartesian grid, which no longer coincide with the solid body surface. The goal of this work is to build a computational tool that will allow us to simulate the flow

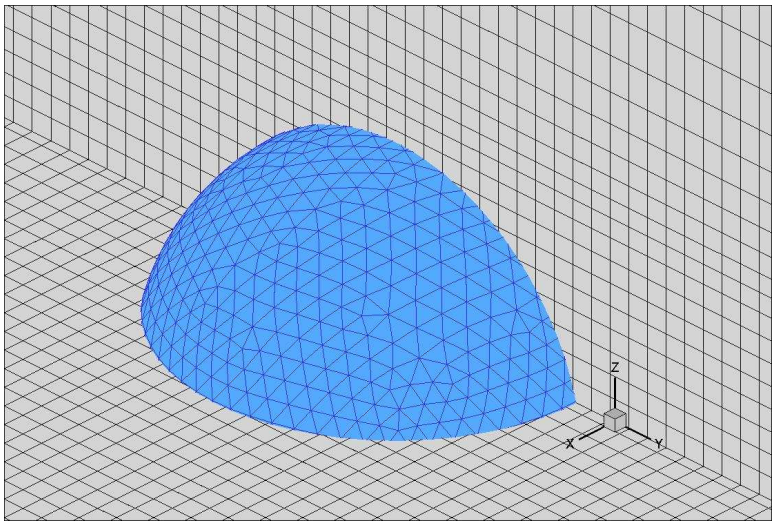

Figure 12: The immersed solid body is here represented by a discretized sphere surface. The size of the two communicating meshes is similar.

field around any generic endothelial surface topography obtained from Atomic Force Microscopy in a relatively straightforward manner. As a consequence, we will develop our numerical code based on the non-boundary conforming methods, eliminating the tedious task of grid adaptation required in classical boundary conforming techniques.

Every immersed surface in our computational domain represents a new physical boundary for the flow field and is created and discretized in triangular elements using a commercially available software named *Gambit*, distributed by *Ansys, Inc.* The linear size of the these elements must be comparable to the size of the Cartesian grid spacing. As will be explained later on, this restriction is essential to avoid poor results in the communication between these two grids, and the way the two meshes exchange information is essential to the code ability to compute realistic solutions. An example of such discretization is shown in figure 12.

The geometrical characteristics of the interface are then exported from Gambit into a specific format file and recalled from the CFD code. This file contains the coordinates of every interface mesh point and the way they are connected to form all of the triangular elements. These data are analyzed and processed, and all of

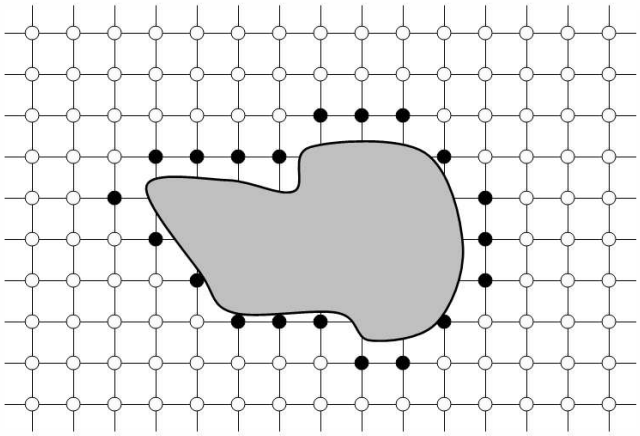

Figure 13: IB points around a generic interface. All the computational black points around the interface will be considered as boundary points during the computation. Boundary conditions must be specified on these points .

the geometrical characteristics of the immersed interface are calculated at this stage. Among these are the area of each triangular mesh element and its normal vector pointing inside the flow field, curvature and normal vectors from each interface vertex, and the volume enclosed by the entire interface; this information will be needed later on during the computation. At this point of the computation we are left with an unstructured triangular mesh immersed in our primitive computational grid. Since a solid body with prescribed motion is now present in the flow-field, boundary conditions known on the unstructured mesh representing the immersed body need to be transferred to the stationary Cartesian grid where the Navier Stokes equations will be solved. A physical model linking the two different meshes is then needed.

Different methodologies have been recently proposed to solve this problem [67]. Our approach is a variation of the work presented by Gilmanov [38], and is organized in different steps. First, the computational nodes of our primitive mesh are classified into three different categories: points inside the solid body, points inside the flow field and points close to the solid-fluid interface, named *immersed boundary* (IB) points. These are nodes within the fluid phase that are closest to the solid body.

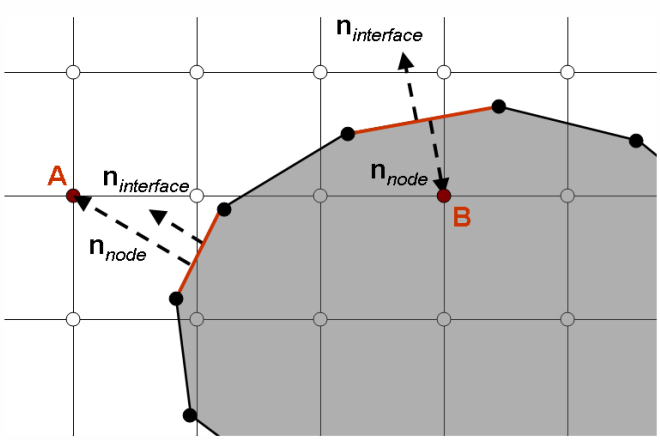

Figure 14: Algorithm to classify each of the Cartesian grid nodes as inside -point B- or outside -point A- the immersed interface.

The governing equations will be solved at all fluid nodes using boundary conditions specified on the IB points (see figure 13). To classify each of the Cartesian grid nodes into one of the mentioned categories, the following algorithm has been developed.

For each Cartesian point, we look for the interface node that is closest to it. All of the triangular interface elements that contain the selected interface point as one of their vertexes are then analyzed. We have to decide which one of these elements will be used for geometrical comparison with the Cartesian grid point under investigation. To do so, for all of the candidate elements we compute the projection of the Cartesian grid point on the plane defined by the interface element itself. Priority condition for a triangular element to be chosen from among others is that it contains the computed projection. If more than one of the candidate elements satisfy this condition, the element whose centroid is closest to the Cartesian point will be selected. The same condition will be considered in case that none of the elements contain the grid point projection. It will be shown soon that the priority given to the condition on the projection of the grid point contained in the interface mesh element is essential for a proper functioning of the overall algorithm. At this stage of the computation, we thus have a Cartesian point under investigation and a selected interface triangular element.

The vector pointing from the projection of the grid point on the plane defined by the considered interface element (either inside or outside the triangular element) to the grid point itself is addressed to as $\mathbf{n}_{node}$. We previously stated that the code already computed the unit vector perpendicular to the interface element itself and pointing outside the discretized solid body: let's refer to it as $\mathbf{n}_{interface}$. As illustrated in figure 14, the following condition is used to classify every computational node

$$\frac{\mathbf{n}_{node} \cdot \mathbf{n}_{interface}}{|\mathbf{n}_{node}|} = \begin{cases} 1 & \text{either fluid node or } IB \text{ node} \\ -1 & \text{solid node} \end{cases} \tag{40}$$

As anticipated earlier, a selection criterion different from the 'contained-projection-condition' in the choice of the interface element used in equation 40 could lead to misleading results. Figure 15 shows what happens if priority is given to a condition on the minimal distance along the normal vector from the element itself, as well as a condition on the minimal distance from the element centroid. Points that are geometrically outside the interface could be considered by the CFD code as inside the interface and vice versa, with deleterious results in the whole computational outcome. Nevertheless, this algorithm can give some problems in case of surfaces with very high curvature, when the angle between two adjacent discrete elements is smaller than 90 degrees. Concerning all of the simulations performed for this work, we run into this problem only when dealing with very simple geometries, such as cubical or cylindrical interfaces. In these easy cases, the problem was overcome through bypassing the described algorithm and defining the grid point properties using simple geometrical considerations on the flow domain. However, the treatment of these extreme cases with an adequate algorithm is beyond the scope of this thesis. To determine the IB nodes, the 6 grid points $(i \pm 1, j, k)$, $(i, j \pm 1, k)$, $(i, j, k \pm 1)$ surrounding any solid node (i, j, k) are investigated. Each such node that is not a solid node is classified as an IB node. Figure 13 shows a 2D illustration of how these points are chosen.

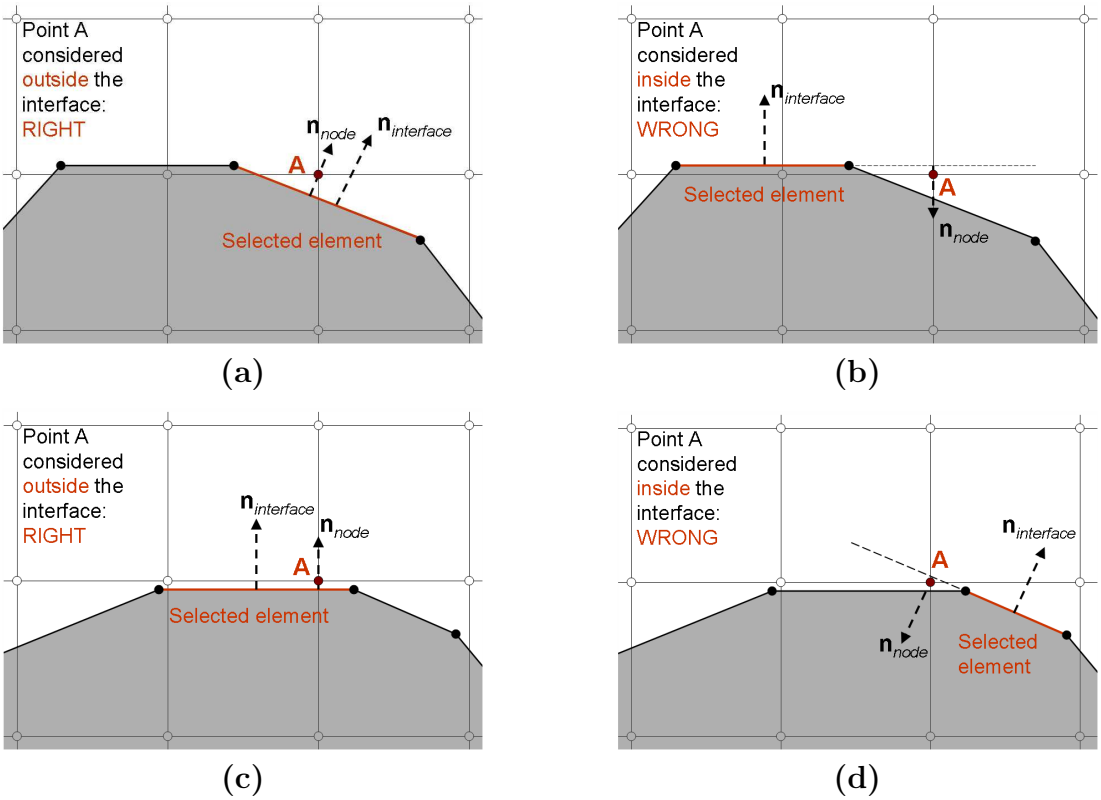

Figure 15: Graphical representation of the algorithm used in the classification of every Cartesian grid point as inside or outside the solid interface. Using the 'contained-projection-condition' we obtain right results in (a) and (c). The other sketches show the erroneous outcome of the algorithm when different criteria are used. (b) Condition on the minimal distance along the normal vector from the element itself. (d) Condition on the minimal distance from the element centroid. For clarity, the vectors $\mathbf{n}_{node}$ have been magnified.

The algorithm can also handle the "inverse" case, where the flow field is inside the immersed interface and everything that is left outside must be considered as a solid. At this point of the computation, every Cartesian grid node has been classified.

To solve our governing equations, we now must assign boundary values to the new IB boundary points. Physical boundary conditions are known on the unstructured interface mesh. These are typically Dirichlet boundary conditions for velocity and Neumann boundary conditions for pressure. Figure 16 represents a 2D simplified illustration of how these boundary values are assigned. The value of the velocity at any IB point is calculated using a linear interpolation between velocities in A

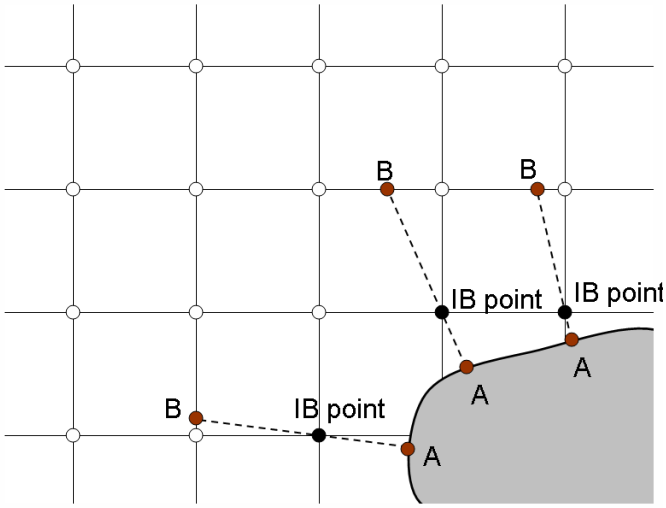

Figure 16: Particular of IB points around a generic interface. The boundary conditions on these points will be specified through interpolation between the values at points A and B.

and B. As discussed earlier, Point A is the normal projection of the IB point on an interface triangular element in case it is contained in the triangular element itself. If no elements happen to contain the projection of the IB point, A will be the node on the interface mesh closest to the IB point itself. Since the physical boundary conditions are assigned only on the interface nodes, when point A represents the projection on an interface element, its velocity is calculated by interpolating the known velocity values at the three vertexes of the triangular element

$$\phi_A = \sum_{i=1}^{N} A_i \phi_i + O(\sum_{i=1}^{N} A_i) \tag{41}$$

where $N = 3$, ϕ_i are the velocity components at the triangular interface vertexes and A_i represent the weights used in the interpolation, as illustrated in figure 17(a). Since the interface element's size is comparable with the surrounding grid spacing dx, this means than $A_i \sim O(dx^2)$, meaning a second order accurate in space approximation. It is evident that this interpolation will not be needed in case the point A is already

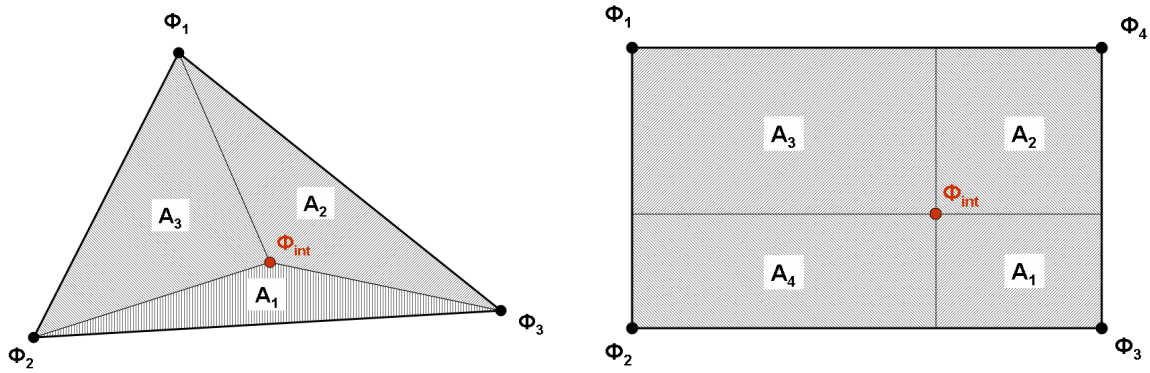

(a) (b)

Figure 17: The value of a variable ϕ at any point inside an interface element (a) or a control cell wall (b) is obtained through interpolation of the known values of the variable at the vertexes of the considered element. Geometrical interpretation.

coincident with an interface node, where physical boundary conditions are directly known. Point B represents the intersection of the line connecting A and the IB point with the first control cell surface encountered. Velocity here is computed bilinearly interpolating the velocity values at the four corner nodes of the intersected surface. Equation 41 will now be applied using $N = 4$, as illustrated in figure 17(b). Accordingly, this is also second order accurate in space approximation. Performing one last linear interpolation between the velocities in A in B, we obtain a boundary condition on the IB point velocity that is second order accurate in space

$$V_{IB} = \frac{dB}{dA + dB} V_A + \frac{dA}{dA + dB} V_B + O(dA^2 + dB^2) \tag{42}$$

since dA and dB, distances from the IB point to respectively points A and B, are comparable to the grid sizing.

To obtain pressure boundary conditions we use a slightly different algorithm. As will be explained in the next section, the Neumann boundary condition on the pressure is given by

$$\nabla p^{n+1} \cdot \mathbf{n} = \frac{\partial p^{n+1}}{\partial \mathbf{n}} = 0 \qquad on \;\; \partial V \tag{43}$$

and is valid everywhere on the interface. From the IB point, we consider the normal to the interface. In case a triangular element contains the projection of the IB point, the normal passing through the IB point will have the same direction cosines of the normal to the triangular element itself. Otherwise, we will use the director cosines of the unit normal from the node on the interface that is closest to the IB point itself. This is calculated as a weighted average of the normal vectors to all of the interface elements containing the considered interface point as one of their vertices (in a total number of el).

$$\mathbf{n} = \frac{\sum_{i=1}^{el} \mathbf{n}_i}{\left| \sum_{i=1}^{el} \mathbf{n}_i \right|} \tag{44}$$

We now have the normal vector passing from the IB node and pointing inside the flow field; we look for its intersection point B with the first control cell surface encountered. As we did for the velocity, the pressure in B is obtained by a bilinear interpolation using the pressure values at the four corner nodes of the considered control cell surface (see figure 17). Using a Taylor expansion around point A, we can thus compute the boundary pressure value on the IB node as

$$P_{IB} = P_B + O((dA + dB)^2) \Longleftarrow \begin{cases} P_B = P_A + \left. \dfrac{\partial P}{\partial \mathbf{n}} \right|_A (dA + dB) + O((dA + dB)^2) \\ \\ P_{IB} = P_A + \left. \dfrac{\partial P}{\partial \mathbf{n}} \right|_A dA + O(dA^2) \end{cases} \tag{45}$$

Once again, the distance $(dA + dB)$ will be comparable to the underlying Cartesian

grid size. Because of the condition of zero normal pressure gradient on the interface point A, the described interpolation is also a second order approximation in space.

In this section we have described how information is passed from the immersed body with prescribed motion to the underlying Cartesian grid, where the conservation equations of fluid mechanics will be solved. All of the described algorithms assure a second order accuracy in space. We will see later on that an inverse process will be needed during the post-processing of our results, when data will be passed from the Cartesian grid to the immersed interface.

4.1.2 Solver

Conservation laws of mass and momentum in their integral form are solved using the fractional step method in its P1 formulation. The first step leads to the calculation of the intermediate velocity $\mathbf{u}^*$ through the equation

$$\int_V \frac{\mathbf{u}^* - \mathbf{u}^n}{\Delta t} dV + \oint_S \mathbf{u}(\mathbf{u} \cdot \mathbf{n}) dS = \frac{1}{\rho} \oint_S 2\mu \mathbb{E}(\mathbf{u}) \cdot \mathbf{n} dS + \int_V \mathbf{f} dV \tag{46}$$

where we still have to decide whether convection and diffusion terms must be treated implicitly or explicitly. The second step calculates a pseudo pressure at the time n+1 through the solution of a Poisson-like equation

$$\frac{1}{\rho} \oint_S \nabla \phi^{n+1} \cdot \mathbf{n} dS = \oint_S \frac{\mathbf{u}^* \cdot \mathbf{n}}{\Delta t} dS \tag{47}$$

We will see later on why this pseudo pressure differs from the thermodynamic pressure. It is then possible to update the value of the intermediate velocity by projecting it in the divergence free vector space

$$\int_V \frac{\mathbf{u}^{n+1}}{\Delta t} dV = \int_V \frac{\mathbf{u}^*}{\Delta t} dV - \frac{1}{\rho} \oint_S \phi^{n+1} \mathbf{n} dA \tag{48}$$

Following the approach used by Kim and Moin [55], convection and diffusion terms are discretized using Adams-Bashforth and Crank-Nicholson schemes, respectively. Both discretizations are second order accurate in time at $t = n + 1/2$. The time derivative in the momentum equation is discretized using a centered approximation, and thus it is also second order accurate in time at $t = n + 1/2$. Using the following notation for convection and diffusion terms

$$H(\mathbf{u}) = \oint_S \mathbf{u}(\mathbf{u}\cdot\mathbf{n})dS \quad and \quad D(\mathbf{u}) = \frac{1}{\rho}\oint_S 2\mu\mathbb{E}(\mathbf{u})\cdot\mathbf{n}dS \tag{49}$$

we will solve the predictor step (46) as

$$\int_V \frac{\mathbf{u}^* - \mathbf{u}^n}{\Delta t}dV + \frac{1}{2}(3H(\mathbf{u}^n) - H(\mathbf{u}^{n-1})) = \frac{1}{2}(D(\mathbf{u}^*) + D(\mathbf{u}^n)) + \int_V \mathbf{f}dV \tag{50}$$

Substituting the integral of the intermediate velocity field as expressed in the projection step (48) into the predictor equation (50) we obtain

$$\int_V \frac{\mathbf{u}^{n+1} - \mathbf{u}^n}{\Delta t}dV + \frac{1}{2}(3H(\mathbf{u}^n) - H(\mathbf{u}^{n-1})) =$$

$$= -\frac{1}{\rho}\oint_S (\phi^{n+1} - \frac{\nu\triangle t}{2}\nabla^2\phi^{n+1})\mathbf{n}dA + \frac{1}{2}(D(\mathbf{u}^{n+1}) + D(\mathbf{u}^n)) + \int_V \mathbf{f}dV \tag{51}$$

This equation is therefore a second order in time approximation of the momentum equation in (5), provided the term for the pseudo pressure ϕ is a second order approximation in time of the real pressure at $t = n + 1/2$

$$p^{n+1/2} = \phi^{n+1} - \frac{\nu\triangle t}{2}\nabla^2\phi^{n+1} \tag{52}$$

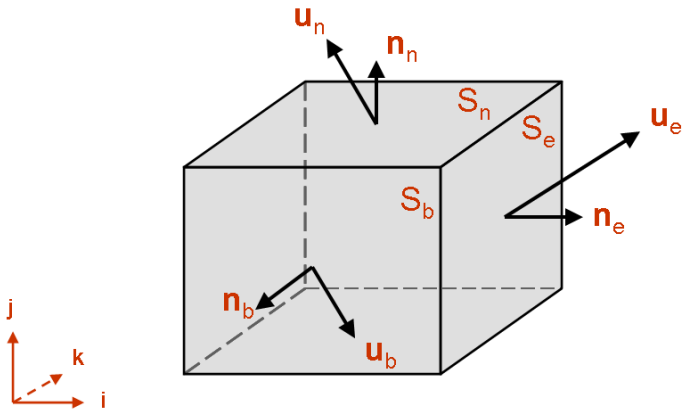

Figure 18: Graphical representation of a control cell with velocities an normals defined on its lateral surfaces.

Step1: Predictor

In order to obtain a numerical solution for equation (50), all of its terms must be discretized. For clarity, we will refer to any variable on the lateral surfaces shared by the i^{th} cell with the $(i+1)^{th}$ and $(i-1)^{th}$ cells with the subscript e (east) and w (west), respectively. Similarly, we will assign the subscripts n (north) and s (south) to the shared surfaces along the $j-axis$ and f (forward) and b (backward) along $k-axis$. The described convention is illustrated in figure 18. All of the surface integrals will be evaluated considering the velocity to be constant on each control cell surface S.

Let's start looking at the convection term H($\mathbf{u}$) as introduced in (49). If we define the following three vectors

$$H^1(\mathbf{u}) = \begin{bmatrix} u^2 \\ uv \\ uw \end{bmatrix} \qquad H^2(\mathbf{u}) = \begin{bmatrix} vu \\ v^2 \\ vw \end{bmatrix} \qquad H^3(\mathbf{u}) = \begin{bmatrix} wu \\ wv \\ w^2 \end{bmatrix} \tag{53}$$

the convection term can thus be expressed as

$$H(\mathbf{u}) \approx (H_e^1 - H_w^1)\mathrm{S}_e + (H_n^2 - H_s^2)\mathrm{S}_n + (H_f^3 - H_b^3)\mathrm{S}_f \tag{54}$$

where, due to the orthogonality of our numerical grid, $\mathrm{S}_e = \mathrm{S}_w$, $\mathrm{S}_n = \mathrm{S}_s$ and $\mathrm{S}_f = \mathrm{S}_b$. Velocity values needed at the cell surfaces are evaluated using the second order accurate in space approximation presented in equation (38).

We now need to consider the diffusion term. The viscous stress tensor can be decomposed into

$$\mathbb{S}(\mathbf{u}) = \mu \left(\mathbb{E}^1(\mathbf{u}) + \mathbb{E}^2(\mathbf{u}) \right) \tag{55}$$

where

$$\mathbb{E}^1(\mathbf{u}) = \begin{bmatrix} \dfrac{\partial u}{\partial x} & \dfrac{\partial u}{\partial y} & \dfrac{\partial u}{\partial z} \\ \dfrac{\partial v}{\partial x} & \dfrac{\partial v}{\partial y} & \dfrac{\partial v}{\partial z} \\ \dfrac{\partial w}{\partial x} & \dfrac{\partial w}{\partial y} & \dfrac{\partial w}{\partial z} \end{bmatrix} \qquad \mathbb{E}^2(\mathbf{u}) = \begin{bmatrix} \dfrac{\partial u}{\partial x} & \dfrac{\partial v}{\partial x} & \dfrac{\partial w}{\partial x} \\ \dfrac{\partial u}{\partial y} & \dfrac{\partial v}{\partial y} & \dfrac{\partial w}{\partial y} \\ \dfrac{\partial u}{\partial z} & \dfrac{\partial v}{\partial z} & \dfrac{\partial w}{\partial z} \end{bmatrix} \tag{56}$$

The diffusion term can thus be expressed as

$$D(\mathbf{u}) = \frac{1}{\rho} \left(\oint_S \mu \mathbb{S}^1(\mathbf{u}) \cdot \mathbf{n} dS + \oint_S \mu \mathbb{S}^2(\mathbf{u}) \cdot \mathbf{n} dS \right) \tag{57}$$

Working on the term depending on $\mathbb{S}^2(\mathbf{u})$, and recalling the conservation of mass condition express in its integral form, we obtain

$$\oint_S \mu \mathbb{S}^2(\mathbf{u}) \cdot \mathbf{n} dS = \nabla \oint_S \mu \mathbf{u} \cdot \mathbf{n} dS = 0 \tag{58}$$

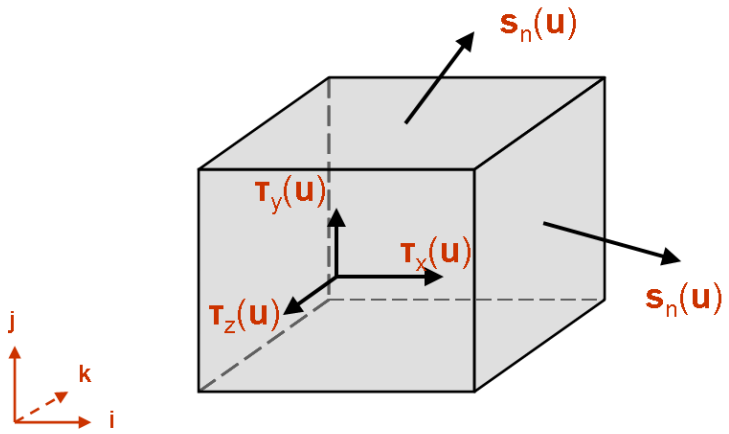

Figure 19: Graphical representation of a control cell with the components of the viscous stress defined on its lateral surfaces. We note that $\mathbf{s}_n(\mathbf{u}) = \mu D^1(\mathbf{u})$ when $\mathbf{n} = (1, 0, 0)$, and accordingly for the other components of tensor $\mathbb{S}$.

since viscosity μ is considered constant throughout the whole domain. The diffusion term thus becomes

$$D(\mathbf{u}) = \frac{1}{\rho} \oint_S \mu \mathbb{S}^1(\mathbf{u}) \cdot \mathbf{n} dS \tag{59}$$

Analogous to what we did with the convection term, let's now define

$$D^1(\mathbf{u}) = \begin{bmatrix} \frac{\partial u}{\partial x} \\ \frac{\partial v}{\partial x} \\ \frac{\partial w}{\partial x} \end{bmatrix} \qquad D^2(\mathbf{u}) = \begin{bmatrix} \frac{\partial u}{\partial y} \\ \frac{\partial v}{\partial y} \\ \frac{\partial w}{\partial y} \end{bmatrix} \qquad D^3(\mathbf{u}) = \begin{bmatrix} \frac{\partial u}{\partial z} \\ \frac{\partial v}{\partial z} \\ \frac{\partial w}{\partial z} \end{bmatrix} \tag{60}$$

The diffusion term can thus be expressed as

$$D(\mathbf{u}) \approx \nu(D_e^1 - D_w^1)\mathrm{S}_e + \nu(D_n^2 - D_s^2)\mathrm{S}_n + \nu(D_f^3 - D_b^3)\mathrm{S}_f \tag{61}$$

The partial derivatives present in this formulation are evaluated using the approximation presented in equation (39). Since considered constant throughout the whole domain, density ρ and viscosity μ do not need to be interpolated. It is interesting to notice how, for each vector in (60), the components associated with the directions lying on the considered cell surface represent the shear stress on the surface itself. The remaining component accounts for the viscous stress perpendicular to the surface that will be added to the hydrostatic pressure.

The other terms in equation (50), accounting for the velocity time derivative and for the force per unit volume $\mathbf{f}(\mathbf{x}, t)$ due to any external force field, are evaluated at the cell center and multiplied by the cell volume, as expressed by

$$\int_V \frac{\mathbf{u}^* - \mathbf{u}^n}{\Delta t} dV \approx \frac{\mathbf{u}_c^* - \mathbf{u}_c^n}{\Delta t} \mathrm{V}_{cell} \qquad and \qquad \int_V \mathbf{f} dV \approx \mathbf{f}_c \mathrm{V}_{cell} \tag{62}$$

At this point, all the terms in the predictor equation have been discretized. We are thus left with the following implicit equation ready to be solved for the intermediate velocity $\mathbf{u}^*$

$$\int_V \frac{\mathbf{u}^*}{\Delta t} dV - \frac{1}{2} D(\mathbf{u}^*) = \int_V \frac{\mathbf{u}^n}{\Delta t} dV - \frac{1}{2}(3H(\mathbf{u}^n) - H(\mathbf{u}^{n-1})) + \frac{1}{2} D(\mathbf{u}^n) + \int_V \mathbf{f} dV \tag{63}$$

Characteristic of this vectorial equation is the decoupled nature of the intermediate velocity components (u^*, v^*, w^*), a condition due to the special form of the conservation of mass in case of an incompressible fluid. Once discretized, the above equation can in fact be represented as

$$\begin{bmatrix} \mathbf{A}_u & \varnothing & \varnothing \\ \varnothing & \mathbf{A}_v & \varnothing \\ \varnothing & \varnothing & \mathbf{A}_w \end{bmatrix} \begin{Bmatrix} \mathbf{u}_l^* \\ \mathbf{v}_l^* \\ \mathbf{w}_l^* \end{Bmatrix} = \begin{Bmatrix} \mathbf{b}_u \\ \mathbf{b}_v \\ \mathbf{b}_w \end{Bmatrix} \qquad l = 1...p \tag{64}$$

where $\mathbf{A}_u, \mathbf{A}_v$ and $\mathbf{A}_w$ are sparse pxp matrixes, $\mathbf{u}_l^*, \mathbf{v}_l^*$ and $\mathbf{w}_l^*$ are px1 vectors of the form

$$\boldsymbol{\varphi}_l^* = \{\varphi_1, \varphi_2, ..., \varphi_p\}^T \qquad \varphi = u, v, w$$

and $\mathbf{b}_u, \mathbf{b}_v$ and $\mathbf{b}_w$ represent px1 vectors accounting for every term present in the right hand side of the discretized prediction equation (63), including velocities computed at previous instants of time, external body forces and, very importantly, velocities at the boundaries at the intermediate time $t = t^*$. These boundary conditions on the velocity field $\mathbf{u}^*$ will be discussed later on. In case p is equal to the entire number of nodes in our computational grid, regardless of their physical position inside or outside any solid boundary, matrixes $\mathbf{A}_u, \mathbf{A}_v$ and $\mathbf{A}_w$ will be tridiagonal plus four additional symmetric bands. For our purposes, we want p to account only for the computational cells where Navier Stokes equations are solved. The three matrixes $\mathbf{A}_u, \mathbf{A}_v$ and $\mathbf{A}_w$ will still be tridiagonal, but the elements of the additional four bands will lose their symmetry. Considering the decoupled equation for $\mathbf{u}_l^*$, it can be written as

$$\mathbf{A}_u \mathbf{u}_l^* = \mathbf{b}_u \tag{65}$$

Every line of this system will present seven unknowns, the velocity u_l^* plus the six velocities at the centers of the surrounding cells. Computational nodes having as their

neighbors points lying on the domain boundary will represent an exception. Referring to u_l^* with $u_{i,j,k}^*$, a generic equation can be expressed as

$$f\left(u_{i,j,k}^*, u_{i\pm1,j,k}^*, u_{i,j\pm1,k}^*, u_{i,j,k\pm1}^*\right) = b_{u(i,j,k)} \tag{66}$$

Let's look at the numerical method used to solve the above linear system. The idea is to compute its solution as the limit of a vector series

$$\mathbf{u}_l^* = \lim_{k\to\infty} \mathbf{r}^k \tag{67}$$

and to stop at the minimum k such as

$$\|\mathbf{r}^k - \mathbf{r}^{k-1}\| < \varepsilon \tag{68}$$

where ε is a pre-defined tolerance. The strategy to build the series $\{\mathbf{r}^k\}$ is based on the splitting of $\mathbf{A}_u = \mathbf{P} - \mathbf{N}$ where $\mathbf{P}$ and $\mathbf{N}$ are matrixes and $\mathbf{P}$ is non singular. Once assigned $\mathbf{r}^0$, we obtain $\mathbf{r}^k$ for $k > 1$ throughout the solution of

$$\mathbf{P}\mathbf{r}^k = \mathbf{N}\mathbf{r}^{k-1} + \mathbf{b}_u \tag{69}$$

Defining the error associated to the $k-th$ iteration as

$$\mathbf{e}^k = \mathbf{r}^k - \mathbf{u}_l^* \tag{70}$$

we can write that

$$\mathbf{e}^k = \mathbf{B}\mathbf{r}^{k-1} \qquad \mathbf{B} = \mathbf{P}^{-1}\mathbf{N} \tag{71}$$

Iterating the process k times we obtain

$$\mathbf{e}^k = \mathbf{B}^k\mathbf{e}^0 \tag{72}$$

where $\mathbf{B}$ is the iteration matrix associated to the splitting. The iteration vector will converge to the real solution if and only if the error shrinks to zero regardless the value of the initial error $\mathbf{e}^0$, condition expressed by

$$\lim_{k\to\infty} \mathbf{B}^k = 0 \tag{73}$$

In our specific case, matrix $\mathbf{A}_u$ in the predictor equation (65) is arranged sweeping the computational domain along the $i - axis$. This means that, including in the matrix $\mathbf{P}$ the tridiagonal elements of $\mathbf{A}_u$, every equation of the new system (69) will look like

$$f_1\left(r^{k+1}_{i,j,k}, r^{k+1}_{i\pm1,j,k}\right) = f_2\left(r^{\#}_{i,j\pm1,k}, r^{\#}_{i,j,k\pm1}\right) + b_{u(i,j,k)} \tag{74}$$

where $r^{\#}$ represents the last available value for r, which is either r^k or r^{k+1}. As initial vector, we choose $\mathbf{r}^0 = \mathbf{u}^n$. The tridiagonal matrix $\mathbf{P}$ is now easily inverted using the TDMA *Thomas algorithm* [20]. In order to get a faster convergence, the computed vector at each pseudo iteration $k+1$ is updated using a *relaxation method*

$$\mathbf{r}^{k+1} = \omega\mathbf{r}^{k+1} + (1-\omega)\mathbf{r}^k \tag{75}$$

where ω is a pre-defined parameter such as $1 < \omega < 2$. Once the convergence condition (68) is met, we are left with our updated value for the u velocity vector

$$\mathbf{u}_l^* = \mathbf{r}^{k+1} \tag{76}$$

The described numerical technique is known as *line successive over relaxation method* (LSOR), and its convergence is assured by the strict diagonal dominance of matrix $\mathbf{A}_u$ [77]. The described numerical process will be in turn applied to the remaining sub-matrices in equation (64), leading to a solution for the velocity components vectors $\mathbf{v}_l^*$ and $\mathbf{w}_l^*$.

Step 2: Poisson-like equation

We now have to compute a value for the pseudo pressure ϕ. It will be used to project the intermediate velocity into a divergence free vector space, as required by the continuity equation. We start discretizing the left hand side of eq. (47) as

$$\oint_S \nabla\phi^{n+1} \cdot \mathbf{n} dS \approx \left(\left.\frac{\partial\phi}{\partial x}\right|_e - \left.\frac{\partial\phi}{\partial x}\right|_w \right) \mathrm{S}_e + \left(\left.\frac{\partial\phi}{\partial y}\right|_n - \left.\frac{\partial\phi}{\partial y}\right|_s \right) \mathrm{S}_n + \left(\left.\frac{\partial\phi}{\partial z}\right|_f - \left.\frac{\partial\phi}{\partial z}\right|_b \right) \mathrm{S}_f \tag{77}$$

where the pseudo pressure derivatives are implicitly evaluated at time $t = n+1$, once again using interpolation formula (39). The remaining right hand side becomes

$$\rho \oint_S \frac{\mathbf{u}^* \cdot \mathbf{n}}{\Delta t} dS \approx \frac{\rho}{\Delta t} \left[(u_e^* - u_w^*)\mathrm{S}_e + (v_n^* - v_s^*)\mathrm{S}_n + (w_f^* - w_b^*)\mathrm{S}_f \right] \tag{78}$$

After imposition of appropriate boundary conditions, as will be discussed soon, the

Poisson-like equation is ready to be implicitly solved for the pseudo pressure ϕ. It can be expressed as

$$\mathbf{A}_\phi \boldsymbol{\phi}_l^{n+1} = \mathbf{b}_\phi \tag{79}$$

where, similar to what happens for the predictor equation, px1 vector $\mathbf{b}_\phi$ includes velocities computed at the intermediate time $t = t^*$ and pseudo pressure values at the boundaries at time $t = n + 1$. To solve the pressure Poisson like equation, both a point over relaxation method (PSOR) and a *alternating direction implicit* method (ADI) have been implemented, but the latter turned out to be more efficient. It consists in solving the previously described LSOR algorithm alternating the sweeping direction of the matrix $\mathbf{A}_\phi$. Using the same notations introduced in the predictor step, we can write the algorithms resulting from the successive sweepings along the three Cartesian directions as

$$\begin{aligned}
f_1\left(r_{i,j,k}^{k+\frac{1}{3}}, r_{i\pm1,j,k}^{k+\frac{1}{3}}\right) &= f_2\left(r_{i,j\pm1,k}^{\#}, r_{i,j,k\pm1}^{\#}\right) + b_{\phi(i,j,k)} \\
f_3\left(r_{i,j,k}^{k+\frac{2}{3}}, r_{i,j\pm1,k}^{k+\frac{2}{3}}\right) &= f_4\left(r_{i\pm1,j,k}^{\#}, r_{i,j,k\pm1}^{\#}\right) + b_{\phi(i,j,k)} \\
f_5\left(r_{i,j,k}^{k+1}, r_{i,j,k\pm1}^{k+1}\right) &= f_6\left(r_{i\pm1,j,k}^{\#}, r_{i,j\pm1,k}^{\#}\right) + b_{\phi(i,j,k)}
\end{aligned} \tag{80}$$

where $r^{\#}$ still represents the last available value for the considered equation. Once convergence condition (68) is satisfied, we are left with the updated value for the pseudo pressure at time $t = n + 1$

$$\boldsymbol{\phi}_l^{n+1} = \mathbf{r}^{k+1} \tag{81}$$

ready to be used in the corrector step.

Step 3: Corrector

As the last step for the projection method, intermediate velocity $\mathbf{u}^*$ must then be updated using the computed pseudo pressure field. Straightforward discretization of projection equation (48) leads to an explicit formulation for the velocity field at time $t = n + 1$ given by

$$\mathbf{u}^{n+1} = \mathbf{u}^* - \frac{\Delta t}{\rho \mathrm{V}_{cell}} \begin{bmatrix} (\phi_e^{n+1} - \phi_w^{n+1})\mathrm{S}_e \\ (\phi_n^{n+1} - \phi_s^{n+1})\mathrm{S}_n \\ (\phi_f^{n+1} - \phi_b^{n+1})\mathrm{S}_f \end{bmatrix} \tag{82}$$

Values for the pseudo pressure at the cell borders are as usual evaluated using equation (38). This step, involving the solution of an explicit vectorial equation, does not need any use of numerical methods for inverting matrixes, as for the previously described steps.

Boundary conditions

Boundary conditions are required on the pseudo pressure ϕ in order to solve equation (47). In addition, since equation (50) is to be advanced implicitly, boundary conditions on the intermediate velocity $\mathbf{u}^*$ are also needed. The latter are also used to compute the right hand side of equation (47). Since both $\mathbf{u}^*$ and ϕ are auxiliary variables, lacking a well defined physical meaning, the original problem formulation does not tell us what boundary conditions should be imposed. A first natural choice for the intermediate velocity, at least for first order schemes, is to impose the physical boundary condition

$$\mathbf{u}^* = \mathbf{u}^{n+1} = \mathbf{b}^{n+1} \qquad on \;\; \partial V \tag{83}$$

Using equation (52) for the pressure, Kim and Moin [55] suggested for the intermediate

velocity boundary condition

$$\mathbf{u}^* = \mathbf{u}^{n+1} + \Delta t \nabla \phi^n \tag{84}$$

proving a second order accuracy in time of the overall scheme. Both of the above conditions on the intermediate velocity have been tested, and they do not seem to perform very differently. Coming to the boundary conditions for the projection step, the issue becomes more complicated. Basic to this issue is the orthogonal decomposition theorem by Ladyzhenskaya [58], that is part of the more general theorem by Hodge [47]. In its simplest form it states that any vector $\mathbf{v}$ defined in V admits the unique orthogonal decomposition

$$\mathbf{v} = \mathbf{w} + \nabla \varphi \tag{85}$$

where $\mathbf{w}$ is solenoidal in V and with zero normal component on the boundary $S = \partial V$. Looking at equation (19) it is natural to introduce the orthogonal projection operator $\mathcal{P}$ onto the vector space $\mathbf{J}$ defined as

$$\mathbf{J}(V) = \{\mathbf{w} \in \mathbf{L}^2(V) \ / \ \nabla \cdot \mathbf{w} = 0, \ \ \mathbf{w} \cdot \mathbf{n} = 0 \ \ on \ \ S = \partial V\} \tag{86}$$

In case we have an homogeneous boundary condition on the normal component of the velocity, i.e. $\mathbf{b}^{n+1} \cdot \mathbf{n} = 0$ on ∂V, the updated velocity $\mathbf{u}^{n+1}$ can be seen as the orthogonal projection of $\mathbf{u}^*$ onto $\mathbf{J}$, i.e. $\mathbf{u}^{n+1} = \mathcal{P}(\mathbf{u}^*)$. For non-homogeneous boundary conditions, we have to recall the orthogonal decomposition of the space of the gradient fields by Temam [32, 75]. The updated velocity $\mathbf{u}^{n+1}$ can then be seen as the orthogonal projection of $\mathbf{u}^*$ onto $\mathbf{J}$, plus the gradient of an harmonic function

h with normal derivative equal to $\mathbf{b}^{n+1} \cdot \mathbf{n}$, as required by the final solution for $\mathbf{u}^{n+1}$, i.e. $\mathbf{u}^{n+1} = \mathcal{P}(\mathbf{u}^*) + \nabla h \quad / \quad \nabla h \cdot \mathbf{n} = \mathbf{b}^{n+1} \cdot \mathbf{n}$. It then comes natural to impose the boundary condition on the updated velocity field as

$$\mathbf{u}^{n+1} \cdot \mathbf{n} = \mathbf{b}^{n+1} \cdot \mathbf{n} \qquad on \;\; \partial V \tag{87}$$

The boundary condition for the pressure is obtained by taking the normal component on the boundary of the first equation in (17). By the conditions imposed on the predictor step (83) and on the projection one (87) we end up with

$$\nabla p^{n+1} \cdot \mathbf{n} = \frac{\partial p^{n+1}}{\partial \mathbf{n}} = 0 \qquad on \;\; \partial V \tag{88}$$

The specification of the boundary condition only for the normal component of the velocity is a characteristic feature of the fractional step methods, and is a consequence of the definition of the space $\mathbf{J}$ involved in the orthogonal projection defined by the Hodge theorem cited above. It is important to note that the above boundary equation has been obtained after the time discretization leading to the fractional step method. This means that it is not correct to consider this as a real physical condition for the pressure in the original problem. Similarly, we can point out that the discrete velocity $\mathbf{u}^{n+1}$ satisfies only the normal component of the real boundary condition. The tangential component is imposed in the computation of the intermediate velocity, so that the error on the overall velocity should be small enough [76]. Although it is possible to find different boundary conditions for the pressure in the literature, they still come from the imposition only for the normal component of the velocity in the projection step [10, 96]. However, the condition on the normal derivative for the pressure (88) remains the most widely used.

At this point, we are now ready to run our simulation. Nevertheless, something

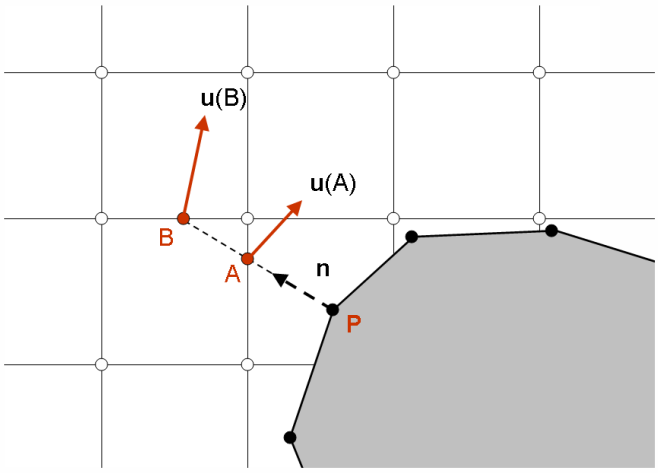

Figure 20: Computed velocities are used to obtain a shear stress value on the interface point P.

else must be done in order to interpret the computed results in a useful manner.

4.1.3 Post-processing and shear stress

From the solution of the time-dependent Navier Stokes equations, we obtain values for velocity and pressure at any point in the discretized flow field at any required instant of time. However, as widely discussed in the introduction chapter, shear stress localization on the surface of the endothelial monolayer is the hemodynamic factor we have to focus on. Computing the shear stress field can be considered as the 'inverse' process of the algorithm used to obtain boundary conditions on the IB points, when known information on the immersed boundary needed to be transferred to the surrounding Cartesian grid. Conversely, we now have to use the computed velocity field on the numerical grid to obtain a shear stress value on each node of the interface mesh.

To describe the algorithm developed to accomplish this task, we must recall the physical meaning of shear stress as described in the a previous chapter. We can refer to the wall shear stress in a point P of a solid body surface as the viscous stress vector minus its projection along the unit normal vector $\mathbf{n}$ to the body surface

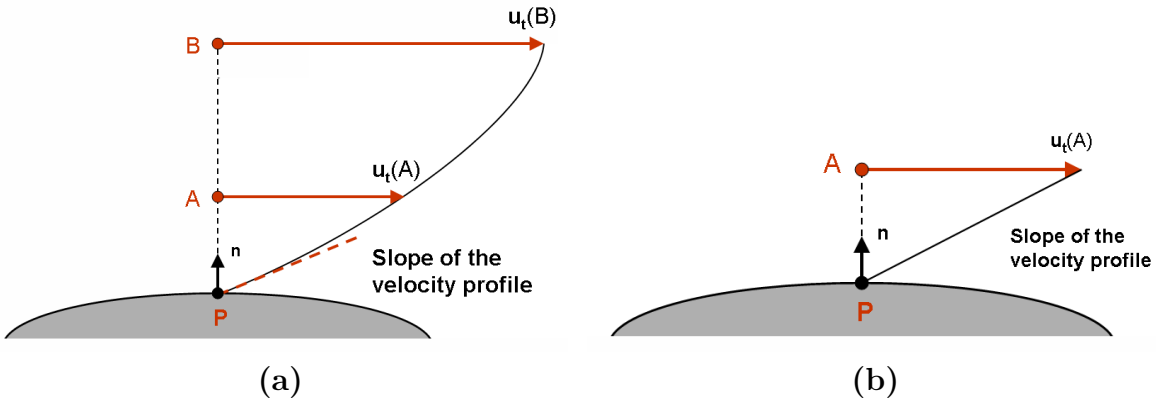

Figure 21: Geometrical interpretation of the algorithm used to compute shear stress on the interface point P using a (a) second order or (b) first order approximation in space.

$$\boldsymbol{\tau}_w = \mu \frac{\partial \mathbf{u}}{\partial \mathbf{n}}\bigg|_{wall} - \left(\mu \frac{\partial \mathbf{u}}{\partial \mathbf{n}}\bigg|_{wall} \cdot \mathbf{n} \right) \mathbf{n} \tag{89}$$

The above definition will be used to compute the shear stress field on the immersed interface, as illustrated in figure 20 for a 2D case. From a generic interface point P, we defined the unit normal vector to the interface as a weighted average of the normals to all of the interface elements containing point P as one of their vertexes, as described in equation 44. Point A and point B represent respectively the intersections of $\mathbf{n}$ with the first and second control cell surface encountered. Once again, velocities at these points are computed throughout bilinear interpolation of the velocity values at the four control nodes of the intersected surfaces (see equation 41). An important exception to this rule will be presented soon. Using the computed velocities, we can obtain a value for the directional derivative of $\mathbf{u}$ in P that is second order accurate in space

$$\frac{\partial \mathbf{u}}{\partial \mathbf{n}}\bigg|_{wall} = \frac{dB^2}{dAdB(dB - dA)}\mathbf{u}_A - \frac{dA^2}{dAdB(dB - dA)}\mathbf{u}_B + O(dB^2) \tag{90}$$

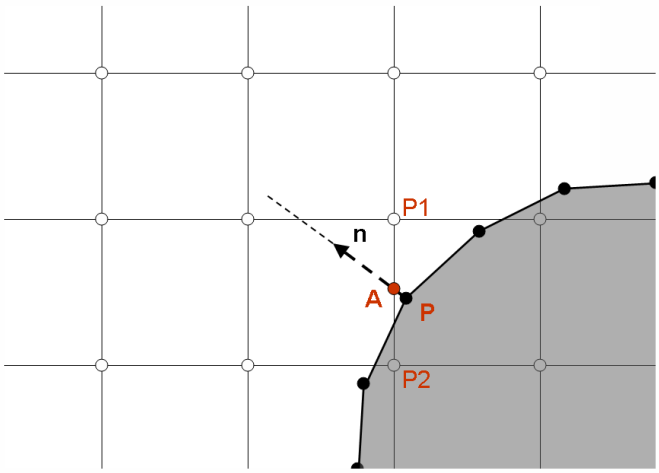

Figure 22: Point A represents the intersection between the normal $\mathbf{n}$ to the interface in P and the grid surface-line $\overline{P1P2}$. In this specific case, vertex $P2$ is inside the solid body. A modified algorithm will be needed to compute the interpolated velocity in A.

or, using the only velocity computed in A, first order accurate

$$\left.\frac{\partial \mathbf{u}}{\partial \mathbf{n}}\right|_{wall} = \frac{\mathbf{u}_A}{dA} + O(dA) \tag{91}$$

where dA and dB represent the distances from point P to A and B, respectively. A simplified 2D geometrical interpretation of the considered approximations is presented in figure 21. Due to the geometrical relationship between dA and dB, we note that, on average, we will have $dB \sim 3dA$. Nevertheless, their values can be very variable. These considerations suggested us to analyze the outcome of the two discretizations before making our choice. Both of the formulas were then tested for numerical simulations whose analytical solutions are known, such as the Poiseuille flow in a circular pipe (see Results chapter). The shear stress values computed by the second order approximation formula were very dependent on the size of dA relative to dB, resulting often poorly accurate on random interface points. Conversely, equation (91) produced very reliable shear stress values everywhere on our immersed interface.

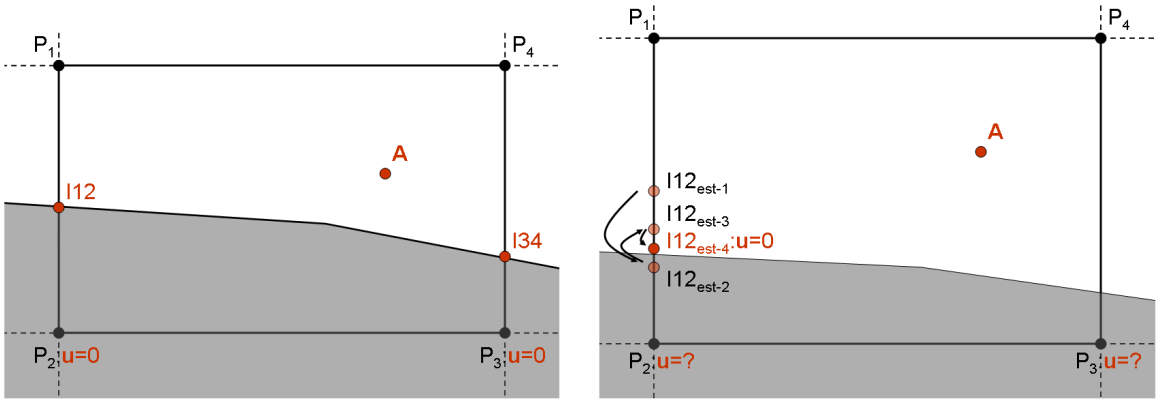

Figure 23: 3D representation of fig 22. Both vertexes $P2$ and $P3$ are inside the solid interface. (a) Exact position of points $I12$ and $I34$ is still unknown. (b) Iterative method used to approximate their position. It will be essential for an accurate determination of velocity in A throughout bilinear interpolation.

We obviously decided to implement the more reliable first-order-accurate algorithm. Now that we have computed the viscous stress vector in P, we can finally obtain a value for the shear stress as

$$\boldsymbol{\tau}_w = \mu \frac{\partial \mathbf{u}}{\partial \mathbf{n}}\bigg|_{wall} - \left(\mu \frac{\partial \mathbf{u}}{\partial \mathbf{n}}\bigg|_{wall} \cdot \mathbf{n} \right) \mathbf{n}$$

Test simulations performed on the described implementation showed this algorithm to perform poorly in specific points of the interfaces. A deeper analysis revealed that the problem arises every time the normal vector $\mathbf{n}$ intersects a control cell surface with specific geometrical features. More precisely, every time that at least one of the four corner nodes involved in the bilinear interpolation is found to be in the solid phase *inside* the interface, the computed shear stress value will not be accurate. A 2D example of such a geometry is illustrated in figure 22. Here, the 2D cell surface intersected by the normal vector $\mathbf{n}$ is represented by line $\overline{P1P2}$. We must notice as point $P2$ is inside the solid body enclosed in the immersed interface. Returning to our realistic 3D case, figure 23(a) shows a generic control cell surface intersected in

A by the normal vector to the interface. In this specific case we suppose that both points $P2$ and $P3$ are solid nodes inside the immersed interface. It is interesting to notice that none of the geometrical configuration tested in this thesis ever resulted in an intersected control cell surface whose number of nodes inside the solid interface was different from zero or two. Points $P2$ and $P3$ are consequently assigned a zero velocity value. This means that hypothetically computed velocities on "interface points" $I12$ and $I34$ using standard bilinear interpolation would result in non-zero values, as opposite to the real "physical" situation of no slip boundary conditions. The way to overcome this incongruence is thus to modify the algorithm to make it reliable also in these specific situations. First, we have to obtain an approximation of the intersection point between the control cell borders and the interface surface. For this purpose, we use an iterative bisecting method. Considering the segment $\overline{P1P2}$ in figure 23(b), we apply the algorithm to classify a point as inside or outside a solid body interface to the middle point M. This will leave us with one of the two halves of the $\overline{P1P2}$ segment still "shared" between the solid and the fluid phases. Iterating this step n times (four will be sufficient for our purposes), it is straightforward to see that our error on the intersection point estimation will be

$$max\left(|I12 - I12_{est-n}|\right) < \frac{\overline{P1P2}}{2^n} \tag{92}$$

Now that we have an estimated intersection point $I12_{est}$, a fictitious velocity value must be assigned to point $P2$ by bilinear interpolation in order to obtain zero velocity in $I12_{est}$

$$\mathbf{u}(P2) = -\frac{d2}{d1}\mathbf{u}(P1) \tag{93}$$

where $d1$ and $d2$ represent the distances between $I12_{est}$ and $P1$ and $P2$ respectively.

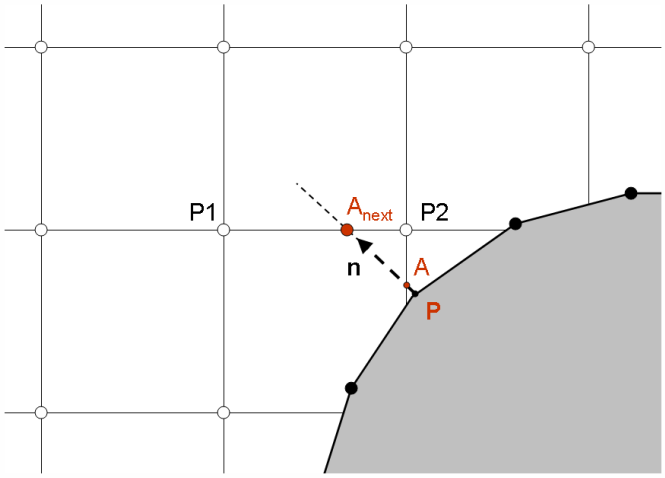

Figure 24: The distance dA between points P and A is below a pre-defined threshold. Point A will then be bypassed to consider next intersection point A_{next}.

The same process will be applied to the other element $\overline{P3P4}$ segment in the figure 23. The new velocities assigned to $P2$ and $P3$ will then be used to compute the velocity in A, as described in equation 41. This modified algorithm was proved to be able to correct all of the previously computed poor estimates of shear stress. A detailed description of these results will be presented in the next chapter. One last comment must be made on this overall procedure to compute the shear stress field on every immersed interface. The distance dA between P and the first intersection point A can happen to be very small. This value is used in the denominator of equation 91, and when too small can cause the computed directional derivative to be not reliable. We overcome this problem using a high pass filter on dA. In case its value is below a set threshold dependent on the local grid size, we bypass the first intersected control element surface to apply our algorithm to the next intersection point A_{next}, as illustrated in figure 24.

4.1.4 CFD code validation procedures

One specific aim of this thesis is to develop a numerical code based on the immersed boundary method (IBM) approach. This code must be capable of predicting the

flow field in the cone-and-plate device in the presence of cultured endothelial cells on the plate surface. All of the developed algorithms that have been described in the previous sections need to be validated. This task is accomplished by running multiple simulations on standard test cases of increasing geometrical and physical complexity. We start by simulating the flow field inside a duct with square cross section. Due to the geometrical simplicity of this configuration, Cartesian boundaries of our orthogonal domain are capable of representing the physical walls of the square tunnel with no need for any immersed solid body interface. This simple case will be also used to asses the order of accuracy of our CFD code. Next, we investigate the solution for a cubic lid-driven cavity flow. No immersed boundaries are yet present in the computational domain, but the complexity of the expected solution increases greatly when compared to the previous test case. We then start running test simulations in the presence of immersed solid bodies in the numerical domain. Poiseuille flow will be simulated inside a cylindrical solid interface. Due to the heterogeneous geometrical orientation of the triangular elements discretizing the immersed interface, this test case will also be used to asses the performance of the developed shear stress algorithm. We then concentrate on uniform flow past a sphere, where recirculation areas in the sphere wake will be investigated. As one last steady state validation test, we simulate the flow field induced in a cylinder with its top wall rotating. This set presents some geometrical similarities to our real cone-and-plate testing device, and will give us insights about the solutions to be expected. We then move on to test our CFD code simulating an unsteady flow. The pressure driven pulsatile flow field inside a cylindrical pipe is analyzed, and the computed results compared with the analytical Womersley solutions. In case our CFD code provides us with trustable and reliable results for all of the validation tests, we will then be ready to run our final simulations on the cone-and-plate device, confident about the accuracy of the flow fields that will be computed.

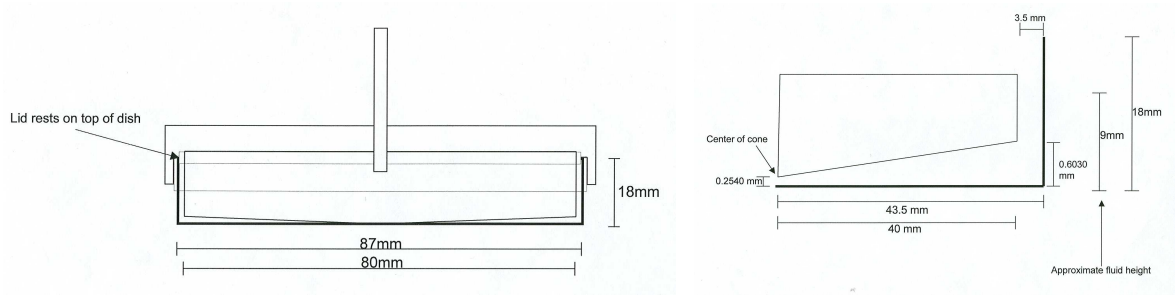

(a) (b)

Figure 25: cone-and-plate device. (a) cross section, (b) particulars of half cross section.

4.2 cone-and-plate simulation

Experiments to investigate the biological response of endothelial cells under shear stress are commonly performed using the so called "cone-and-plate" device. One such device employed by collaborators at Emory University consists of a cylindrical container (plate) with a 87mm diameter coupled with a conical shaped cylinder (cone) with a 80mm diameter. The cone angle is $\beta = 0.5$ degrees. The gap between the cone and the plate can be adjusted at the desired height. Most of the experiments we want to simulate are carried out with the gap height h=0.254mm. Figure 25 shows the geometry of the mechanical device.

4.2.1 Numerical domain

One first difficulty encountered in the simulation of the flow field in the cone-and-plate device arises from the geometry of the numerical domain. Its height is two orders of magnitude smaller than its radial size, this representing a problem in the creation of a suitable computational mesh. In fact, in order to construct a mesh with a comparable number of elements along each of the three Cartesian directions, very distorted computational cells should be used. Numerical instability may arise from the use of such distorted elements. On the other hand, creating a mesh with more regular elements would mean having an enormous number of elements along

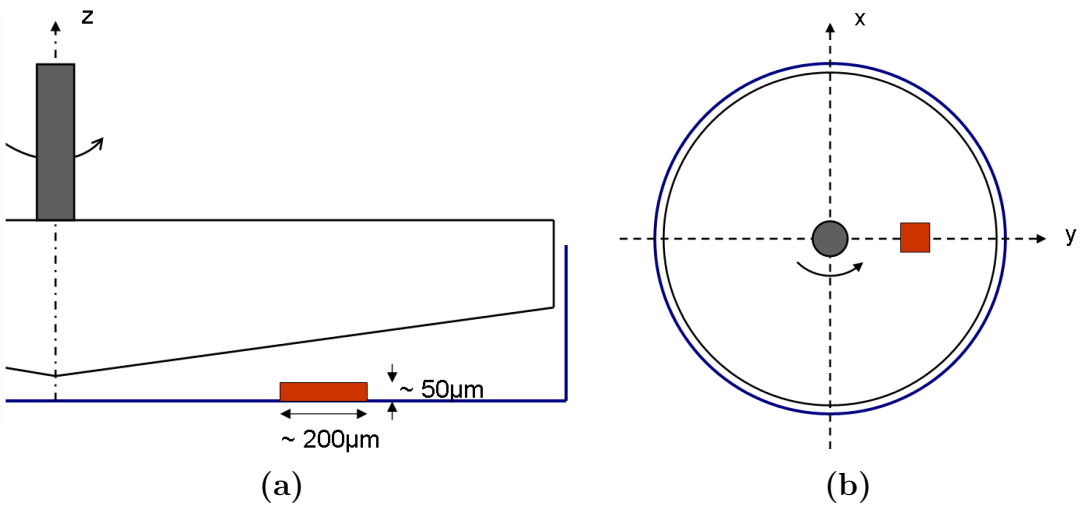

Figure 26: Side (a) and top (b) views of the new numerical domain, obtained considering only a brick-shaped portin of the original cone-and-plate domain. For clarity, geometrical proportions are not respected.

the two directions perpendicular to the axis of rotation of the cone, and a single processor would not be suitable anymore to carry such a heavy computational load. Implementing the message passing interface (MPI) in the computational code in order to use a cluster of processors would provide a much higher computational power to overcome this problem, but this solution is beyond the scope of this thesis.

The alternative approach is then to simulate the flow field in a specific section of the original cone-and-plate domain. This is obtained considering only a small brick-shaped portion of the original domain , as illustrated in figure 26. Its bottom surface represents a sector of the real plate surface, and it is then straightforward to impose no slip boundary conditions on that. When we try to impose boundary conditions on the remaining top and lateral surfaces, we have to face the problem that these surfaces are in the interior of the original cone-and-plate domain, and thus no velocity values are given from simple physical considerations.

The way we proceed is to solve analytically a simplified version of the Navier-Stokes equations in the whole cone-and-plate domain using reasonable hypotheses

based on the expected solution. This will be done following the asymptotic expansion approach described in [88, 6, 11]. For the unsteady case of the oscillatory cone displacement, a perturbation method similar to the one used by Chung [19] will be used. Once the analytical solutions are computed, they are compared to the numerical solutions obtained by a commercially available CFD code named *Fluent*, distributed by *Ansys, Inc.* The two results are thus compared and integrated to achieve an *hybrid* solution that will be used to impose numerical boundary conditions on our new "reduced" numerical domain. We are then left with one last step before our CFD simulation is ready to be run.

4.2.2 AFM and endothelial monolayer geometry

Our numerical solution must describe the detailed flow field over the surface of a small group of specific endothelial cells. Since the fluid mechanical environment over cultured endothelial cells has been found to be a key factor in the production of various sensor and signaling molecules, this work will aid investigation on a quantitative basis of the cell biological responses under different flow conditions near the cell surface. Essential to this is to simulate the flow field in the device using the realistic geometry encountered in the *in vitro* experiments. For this purpose, the surface of the endothelial cells layer must also be discretized, meshed and included as an immersed boundary in our computational domain. This surface will then represent the new boundary where no slip physical boundary conditions must be imposed. The solid-fluid interaction algorithm previously described will then compute the new set of numerical boundary conditions on the IB points surrounding the cells monolayer surface.

We want to be able to characterize the flow field around a cluster of endothelial cells with a spatial resolution one order of magnitude smaller than the single cell size. Endothelial cells are approximately 3-4 μm thick and 20-80 μm in the circumferential

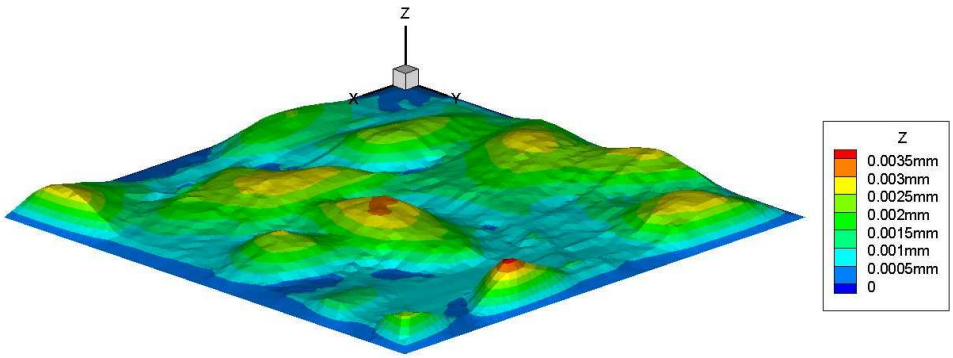

Figure 27: Monolayer of cultured endothelial cells imaged with AFM shown using Techplot software. The data have been previously processed by Gambit.

and axial dimensions. Because of the actual limits in CPU computational power, it then seems unrealistic and unnecessary trying to simulate the flow field over a wide area covered with endothelial cells. The idea is then to try to simulate the flow field over a smaller area of the plate surface where a reasonable number of confluent endothelial cells have been modeled. The number of these cells will depend on the spatial resolution we need on a single cell.

With the great advances in the field of AFM (atomic force microscopy), it is nowadays possible to obtain 3D images with a resolution capable of accurately describing the surface topology of a single endothelial cell cultured in vitro. Therefore, using AFM, detailed images of a single layer of cultured endothelial cells may be obtained. In figure 27 we present the image of the topology of such a monolayer obtained from AFM. The idea is to process these images and obtain the endothelium surface geometry needed by the numerical code. This geometry will allow us to perform numerical analyses and simulate experiments performed with the real cone-and-plate device, where cultured endothelial cells are subjected to shear stress resulting from the rotation of the device. Using a computational mesh with a spatial resolution higher than the average single cell length, it will then be possible to compute the variations of the fluid mechanics parameters over the surface of the single cells.

CHAPTER V

RESULTS

5.1 CFD code validation

In order to test our CFD code performance, different simulations based on standard problems, whose solutions have been widely investigated in the literature, are executed. Each time a computation simulating a steady state flow field is implemented, the time step used will lose its original physical Nevertheless, in order to avoid numerical instability, its size must be chosen very carefully, depending on the specific computational setup. In order to check if the computed solution has reached a steady state, at the end of each time step n a pointwise stability error defined as

$$\varepsilon_s = \max_{i,j,k} \frac{|\mathbf{u}^n_{i,j,k} - \mathbf{u}^{n-1}_{i,j,k}|}{|\mathbf{u}^n_{i,j,k}|} \tag{94}$$

is computed. The simulation will be stopped for the first estimated error smaller than a pre-defined value, and the last computed flow field will be considered the sought solution. Next step is then to check if this solution, although stable, has converged to the right value. This is verified by comparing it to the benchmark solution considered for the specific problem, usually available in the scientific literature either in analytical or numerical form. In order to assess the CFD code performance for time dependent problems, one last validation test simulating the unsteady oscillatory Womersley flow inside a rigid tube is performed. An accurate computed solution will make us more confident when simulating the oscillatory flow field over a layer of endothelial cells, considered the final goal of this thesis.

In the following sections, those simulations whose numerical domains contain solid

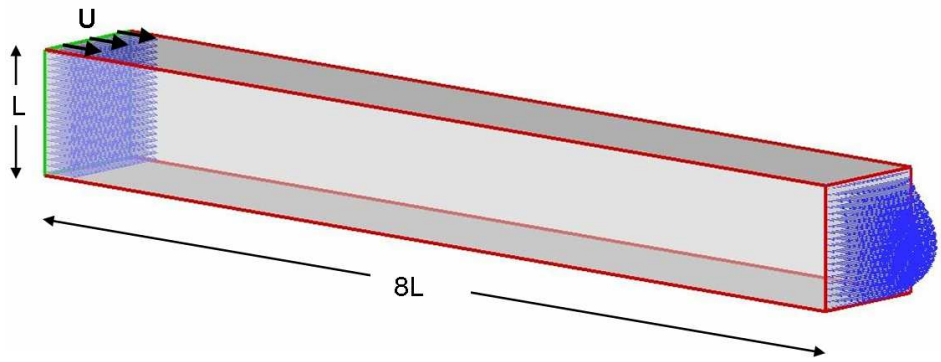

Figure 28: Geometry of the duct with a square cross section. Imposed velocity profile at the inlet and computed fully developed profile at the outlet.

interfaces are indicated with the symbol *IB*. To account for the solid-fluid interaction, the previously described algorithms developed for the immersed boundary method are implemented.

5.1.1 Flow in a duct with square cross section

The first simulated test case involves the flow in a duct with square cross section. The rectangular Cartesian grid is capable of fully describing the required geometry for this problem, with no need for immersed interfaces in our computational domain, as illustrated in figure 29.

Geometry, initial and boundary conditions

The length of the duct is eight times the length of the side of the duct square cross section, named L. This is enough to obtain at the outlet section a fully developed flow, provided the Reynolds number is sufficiently low. This condition will be checked by comparison of the velocity profiles at different sections in the proximity of the outflow.

At the inlet section, Dirichlet boundary conditions on the velocity field are implemented through the imposition of a uniform and constant velocity value U on the entire surface. To avoid discontinuities in the initial velocity field, the u value at

the inlet section is smoothly increased in time from zero to U. Neumann boundary conditions are imposed at the outlet section, where the velocity variation along the longitudinal axes of the duct is set to zero. This corresponds to the condition of a fully developed flow. On the remaining four lateral surfaces, no-slip zero velocity boundary conditions are implemented. Regarding boundary conditions for the pressure field, a constant value P_{in} is imposed at the inlet, and a linear variation at the outer section. On the lateral walls, pressure variations along the directions normal to the surfaces are set to zero. All of these conditions, summarized below, are implemented using second order in space approximations.

$$\begin{cases} initial\ (t=0) & \mathbf{u}=0 & & p=0 \\ inlet & u=0 \rightarrow U & v=w=0 & p=P_{in} \\ outlet & \dfrac{\partial \mathbf{u}}{\partial x}=0 & & \dfrac{\partial p}{\partial x}=constant \\ lateral\ surfaces & \mathbf{u}=0 & & \dfrac{\partial p}{\partial \mathbf{n}}=0 \end{cases}$$

Using L and U as our characteristic length and velocity in the definition of the Reynolds number, the simulation is performed at the low Reynolds number Re=10.

Results

The numerical simulation is performed on a uniform mesh whose grid size is L/20, resulting in a computational mesh of about 80k cells. The computation is stopped when a pointwise stability error $\varepsilon_s < 10^{-5}$ is achieved. At this time, a global conservation of mass will also be reached, such that the difference between the inflow and the outflow is less than one percent. The evolution in time of both the pointwise error

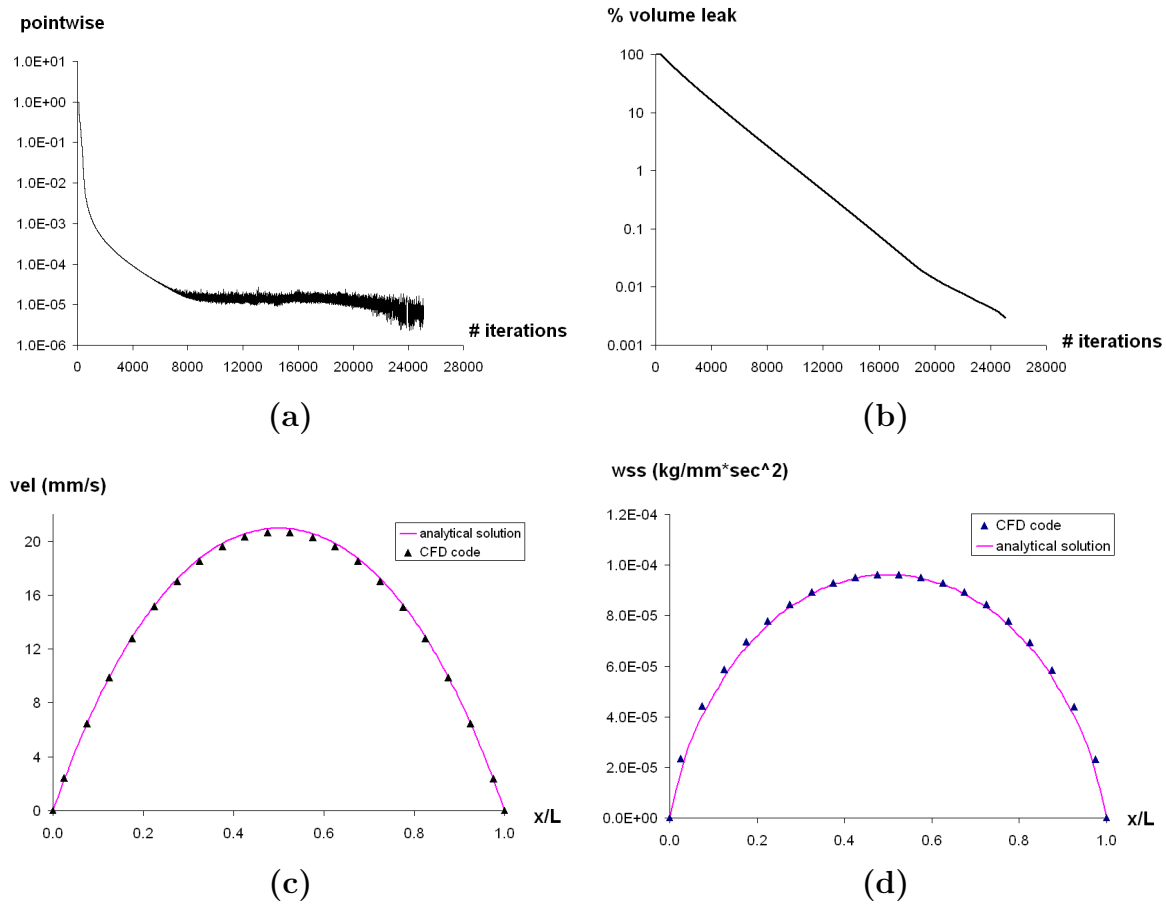

Figure 29: Flow in a duct with square cross section. Pointwise error (a) and volume leak (b) evolutions in time. Comparison between analytical and numerical solution at the intersection line between the outflow cross section and a longitudinal median plane for velocity (c) and wall shear stress (d) profiles.

and the volume leak between inlet and outlet sections is shown in figures 29 (a,b)

The numerical results are then compared to the analytical solution obtained using the separation of variables to solve the governing equations. Figure 29 (c) shows the velocity profile obtained on the intersection line between the outflow cross section and a longitudinal median plane. To prove that the flow is fully developed, a second velocity profile at a different section close to the outlet is also analyzed. Those results perfectly overlap with the outlet flow profile. The wall shear stress on one side of the transversal cross section is also plotted. Because of the geometrical symmetry of

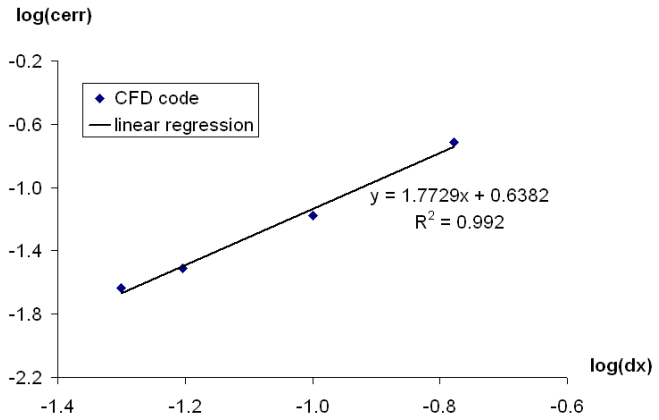

Figure 30: Flow in a duct with square cross section. Error vs. grid size shows the numerical scheme to be almost second order accurate in space.

the domain, this will be representative of the shear stress computed on any of the four sides. A good agreement between the analytical and the numerical solutions is obtained for both velocity and wall shear stress.

This simple case is also used to study the order of accuracy of the CFD code in case no interfaces are present in the domain. Defining the $\ell_{2,\triangle x}$ norm in our finite dimensional space, we can compute the convergency error as

$$\varepsilon_c = \|\mathbf{err}\|_{2,\triangle x} = \sqrt{\Sigma_{i,j,k}|\mathbf{u}_{i,j,k} - \mathbf{u}^b_{i,j,k}|^2 \Delta x \Delta y \Delta z} \tag{95}$$

where $\mathbf{u}$ and $\mathbf{u}^b$ respectively represent the computed and the benchmark solutions, while N, Δx, Δy and Δz define number and size of the computational cells in the domain. The same simulation is then run using differently refined meshes, whose grid sizes range from L/6 to L/20, and the convergency error for each of these solutions is computed. In figure 30, the convergency errors with respect to the analytical solution are plotted as a function of the grid size. From the slope of the regression line interpolating the error data, we can infer that our numerical code is almost second order accurate in space.

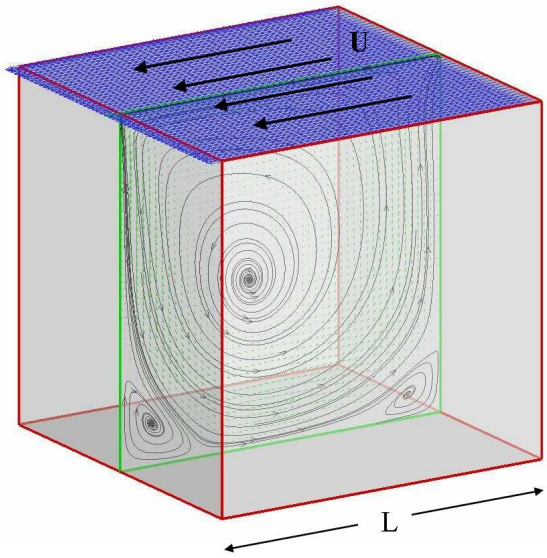

Figure 31: Geometry of the cubical domain. The top lid (dark blue) moves with constant velocity U. The flow will be computed inside the solid interface. Curves are the representation of streamlines projections on a planar central section.

5.1.2 Cubic lid-driven cavity flow

In order to analyze a more complex problem, the flow in a cubic lid-driven cavity is now simulated. The orthogonal computational grid will still be capable of representing the geometry of this problem with no need for immersed interfaces, as illustrated in figure (31).

Geometry and boundary conditions

The computational domain consists of a cube with side length L. No slip Dirichlet boundary conditions for velocity are imposed on all of the six cube surfaces. The top wall moves with a constant velocity U along the *x-axis*, while all of the other walls are fixed. A zero pressure variation along the normal to every lateral surface is also imposed, reflecting the typical Neumann boundary condition used on solid walls. All of the described conditions, summarized below, are implemented using, once again, second order approximations in space.

$$\begin{cases} \textit{initial } (t=0) & \mathbf{u}=0 & & p=0 \\ \textit{top wall} & u=U & v=w=0 & \dfrac{\partial p}{\partial \mathbf{n}}=0 \\ \textit{lateral and bottom walls} & \mathbf{u}=0 & & \dfrac{\partial p}{\partial \mathbf{n}}=0 \end{cases}$$

Using L and U as our characteristic length and velocity in the definition of the Reynolds number, the flow field is simulated at Re=100, 400, 1000.

Results

All the simulations are performed using a grid size L/50, resulting in a computational mesh of about 150k cells. A single case with an improved grid resolution including about 500k mesh points was also solved, and it did not produce significantly more accurate results. For each simulation, a steady state with a pointwise stability error $\varepsilon_s < 10^{-3}$ is achieved. The fact that the error does not become smaller, especially at high Reynolds numbers, depends on the vortexes arising at the center and at the bottom corners of the domain. Accordingly, the points exhibiting the highest errors are clustered in the proximity of the vortexes centers, where velocities are tipically very small. Excluding these areas from the computation of the stability error, a value $\varepsilon_s < 10^{-4}$ is easily reached.

The solution computed by Ding [29], already shown to be in agreement with the ones obtained by Ku [57], Jiang [50] and others [33, 43], is here considered to be our benchmark solution. The computed velocity profiles along the vertical and horizontal centerlines are given and compared with the Ding data. Figure 32 shows a very good agreement between the two solutions for both vertical and "axial" velocities for all of the simulated Reynolds numbers. Figure 33 also shows the streamlines on the

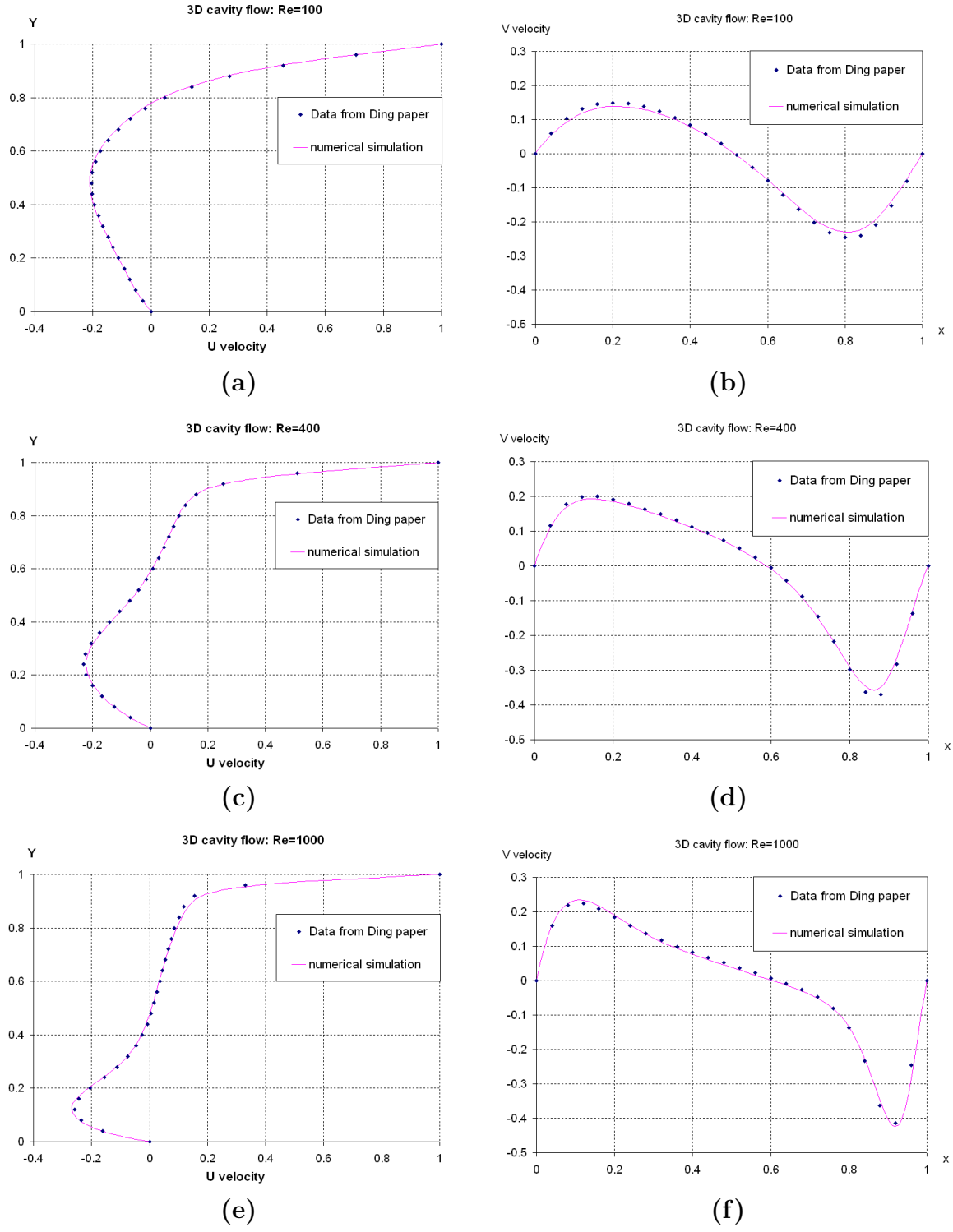

Figure 32: 3D cavity flow. Comparison of velocity distribution along the vertical centerline of the cubic cavity: (a and b) Re=100, (c and d) Re=400, (e and f) Re=1000.

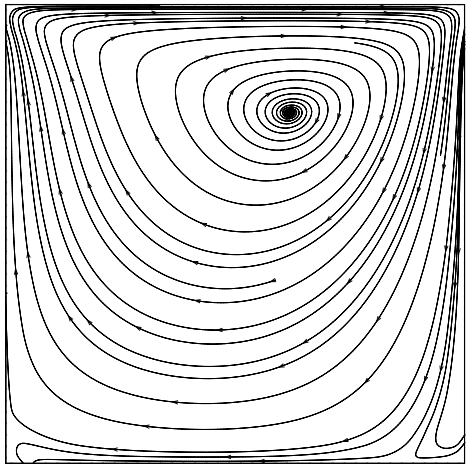

(a)

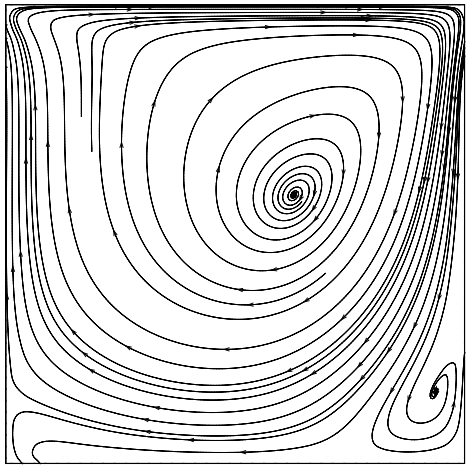

(b)

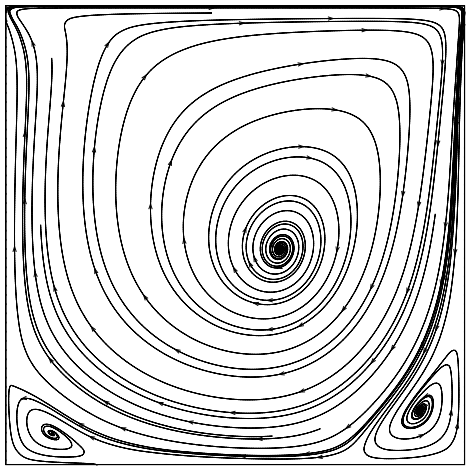

(c)

Figure 33: 3D cavity flow. Flow patterns at mid-vertical-plane: (a) Re=100, (b) Re=400, (c) Re=1000.

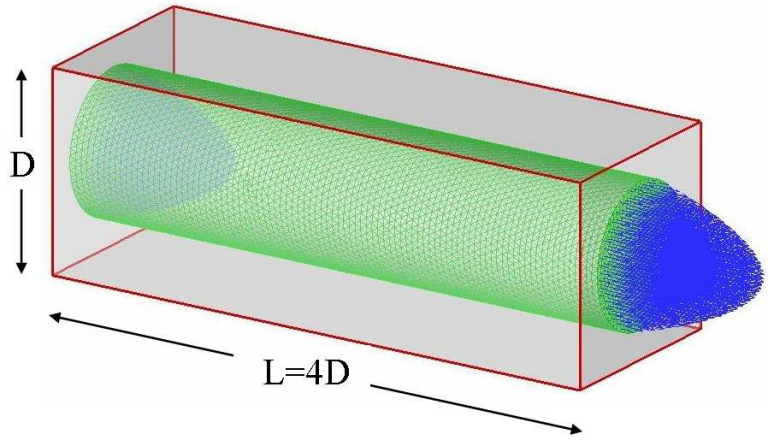

Figure 34: Poiseuille flow. Geometry of the cylindrical interface immersed in the Cartesian computational domain. The flow will be computed inside the solid interface.

mid-vertical-plane for the three different Reynolds numbers. It can be observed that the axis of the primary vortex starts at the top right corner and then moves towards the center as the Reynolds number increases. Moreover, the size of the recirculating areas at the bottom corners becomes larger as the inertial forces increase compared to the viscous ones. This is also in agreement with the solution obtained by Ding.

5.1.3 Poiseuille flow - *IB*

As one first simulation implementing the *immersed boundary method*, the 3D Poiseuille flow inside a cylindrical pipe is implemented. The computational domain is still represented by a Cartesian grid, but a cylindrical solid interface is now immersed in it. Figure 34 shows the geometry of the two domains, where the Cartesian mesh has been shaded for clarity. The governing equations are solved exclusively inside the interface.

Geometry and boundary conditions

The length of the duct L is four times the length of the diameter of the cylinder cross section, named D. The imposition of appropriate boundary conditions is here

different compared to the previous case of flow in the duct with square cross section. Due to the presence of an immersed interface inside the computational domain, all of the Cartesian grid points geometrically outside the cylinder will not be part of the flow field, and thus excluded from the computation. As a consequence, we do not need to impose any boundary condition on the Cartesian longitudinal walls. Conversely, boundary conditions are now needed on the cylindrical interface, representing the new physical border for the flow field under investigation. On this surface, no slip boundary conditions are imposed on the velocity field, while the value for the pressure variation along the normal is set to zero. Neumann boundary conditions are implemented at both the inlet and the outlet Cartesian sections through the imposition a zero derivative for the velocity values along the longitudinal axis of the cylinder. Pressure is here treated using Dirichlet type boundary conditions. To avoid numerical instabilities caused by discontinuities in the pressure field, a zero pressure value is imposed at the outlet, while an increasing in time value from zero to $P_{in} = 1.28 \cdot 10^{-3}\ kg/(mm \cdot s^2)$ is forced at the inlet section. The overall boundary conditions are summarized below.

$$\begin{cases} initial\ (t=0) & \mathbf{u} = 0 & p = 0 \\ inlet & \dfrac{\partial \mathbf{u}}{\partial x} = 0 & p = 0 \longrightarrow P_{in} \\ outlet & \dfrac{\partial \mathbf{u}}{\partial x} = 0 & p = 0 \\ cylinder\ lateral\ surfaces & \mathbf{u} = 0 & \dfrac{\partial p}{\partial \mathbf{n}} = 0 \end{cases}$$

The difference between this simulation and the previous one performed in the duct with square cross section must be once again remarked. In that case, a specific amount

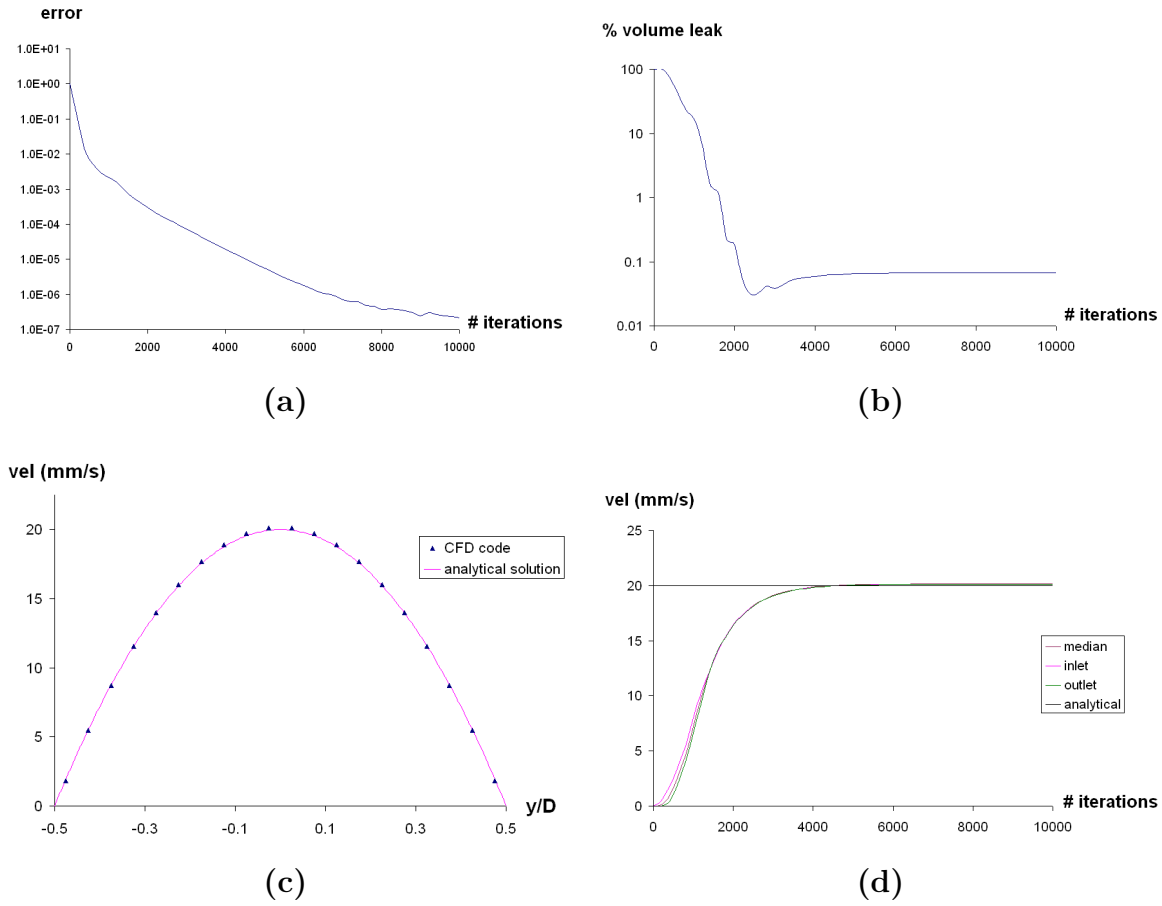

Figure 35: Poiseuille flow solution. Pointwise error (a) and volume leak (b) evolutions in time. Comparison between analytical and numerical solution of the velocity profile on a generic diameter at the outlet section (c). Evolutions in time of the centerline velocities computed at different sections of the pipe (d). The analytical value at fully developed flow is also shown for comparison.

of flow was forced throughout the inlet section, and the difference in pressure necessary to drive that flow was consequently "developed" by the code. In the current simulation, a pressure gradient along the cylinder is now imposed, letting the CFD code compute the resulting pressure-driven velocity field. Because of this assumption, it is not necessary to use a channel long enough to obtain a fully developed flow. Using D and the expected centerline velocity U as our characteristic length and velocity in the definition of the Reynolds number, the simulation is performed at

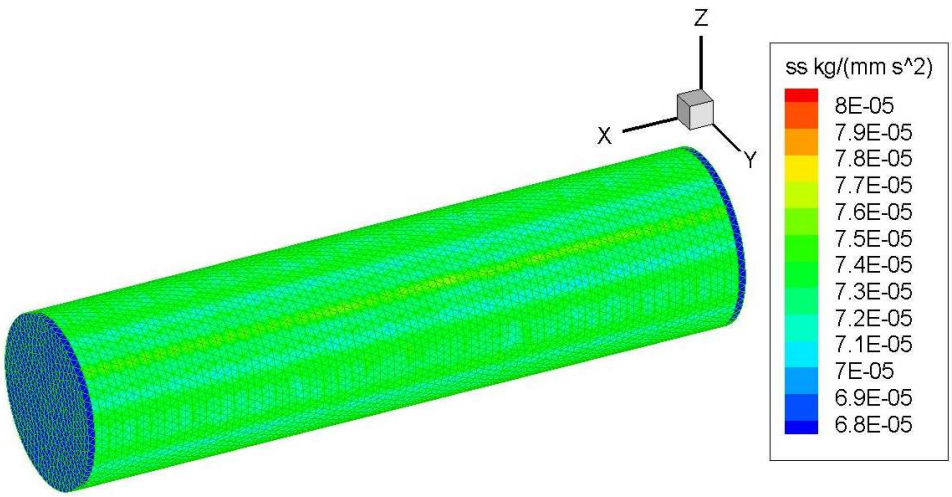

Figure 36: Wall shear stress computed on the cylindrical inner surface. The expected value from the analytical solution is $8 \cdot 10^{-5} kg/(mm \cdot s^2)$.

Re=20, considering for this specific case a channel diameter D=4mm and a water-like fluid with viscosity $\mu = 10^{-6} kg/(mm \cdot s)$ and density $\rho = 10^{-6} kg/mm^3$.

Results

The numerical simulation is performed on a uniform mesh whose grid size is D/20, resulting in a computational mesh of about 75k cells. The cylinder surface is discretized with an unstructured triangular mesh, whose elements have a side length comparable to the grid spacing. The computation is stopped when a pointwise error $\varepsilon_s = 10^{-6}$ is reached. At this time, a global conservation of mass is also achieved, being the difference between the inflow and the outflow of less than one percent. Error and volume leak evolutions in time are shown in figure 35 (a,b). Our results are compared to the analytical Poiseuille solution, whose velocity profile is given by

$$u(r) = \frac{1}{4\mu} \frac{\Delta p}{L} (R^2 - r^2) \tag{96}$$

where R indicates the radius of the circular section. In figure 35 (c), the velocity profile

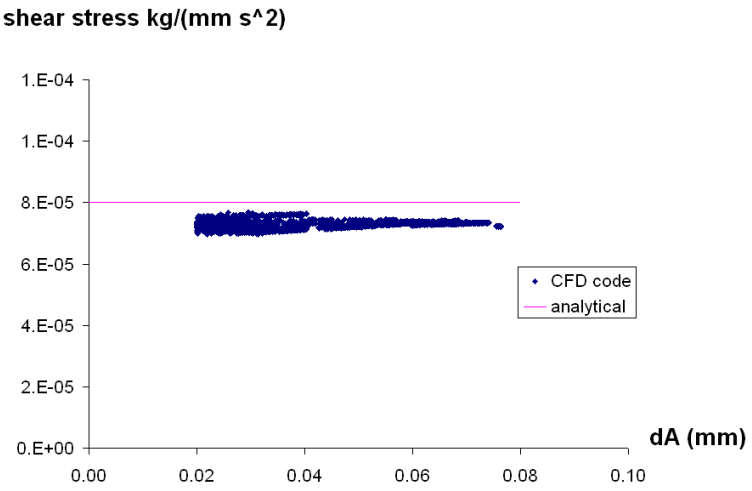

Figure 37: Wall shear stress values on the cylinder as a function of the interface grid points distances dA defined in 4.1.3.

computed on a generic diameter at the outlet section is compared to the analytical solution. The evolutions in time of the centerline velocities computed at different sections are also presented. A good agreement between analytical and numerical solutions is obtained in both cases.

This interface geometry can now be used to investigate the performance of the algorithm implemented for the shear stress computation. Due to the heterogeneous geometrical orientation of the triangular elements used to discretize the cylindrical interface, an accurate evaluation of the algorithm running under generic conditions can be achieved. From the Poiseuille analytical solution, the wall shear stress vector is always oriented along the longitudinal axis of the cylinder, and its magnitude is given by

$$\tau_w = \frac{R}{2}\frac{\Delta p}{L} = 8 \cdot 10^{-5} \frac{kg}{mm \cdot s^2}$$

Figure 36 shows the color contour of the numerically computed values of wall shear stress on the cylindrical interface. Plotting these values as a function of the distance

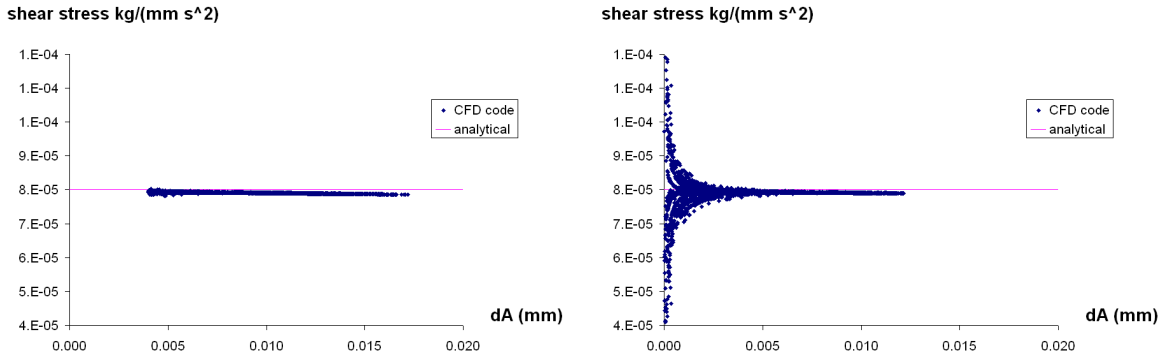

(a) **(b)**

Figure 38: Wall shear stress values computed on the cylinder using (a) and not using (b) a filter on dA.

dA between the interface grid point and its normal intersection with the Cartesian mesh, as defined in figure 24, values ranging between

$$6.95 \cdot 10^{-5} \frac{kg}{mm \cdot s^2} \leq \tau_w \leq 7.69 \cdot 10^{-5} \frac{kg}{mm \cdot s^2}$$

are obtained. Interface points exhibiting the worst wall shear stress approximations exhibit errors, when compared to the analytical value, up to 13% (figure 37). Looking at the same plot obtained by running a simulation on a five times more refined mesh, whose grid size is then D/100, an error on the computed shear stress values never exceeding 2% is achieved,

$$7.83 \cdot 10^{-5} \frac{kg}{mm \cdot s^2} \leq \tau_w \leq 8.02 \cdot 10^{-5} \frac{kg}{mm \cdot s^2}$$

as shown in figure 38 (a). This example shows how accurate values for the computed pressure and velocity do not imply an equally accurate estimation of the shear stress field. However, performing successive refinements of the grid size, it is possible to converge to the required precision for the shear stress computation. Thus, the shear

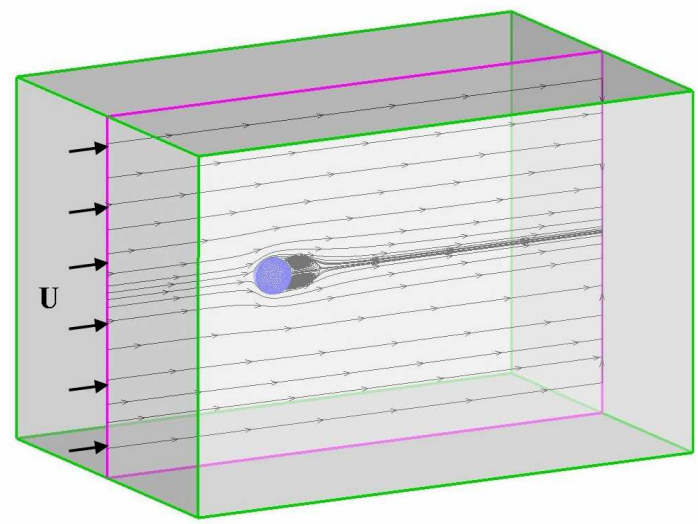

Figure 39: Uniform flow past a sphere. To avoid any sphere influence on the imposed velocities at the boundaries, a computational domain much larger than the sphere is used.

stress algorithm turns out to be much more sensitive to the mesh size than the solver for the governing equations. As a consequence, every time an accurate shear stress field is the simulation priority, it will be necessary to perform a sensitivity analysis with respect to the mesh size. One last remark must be presented about the algorithm for the shear stress computation. Figure 38 (b) shows how poor is the wall shear stress evaluation in case no filters are used on the distance dA. Bypassing any grid intersection point whose distance dA is smaller than a predefined value dA_{min}, as explained in 4.1.3 and here set to $dA_{min} = 0.4\Delta x$, the accurate evaluation shown in plot 38 (a) is obtained.

5.1.4 Uniform flow past a sphere - *IB*

The next validation test involves the uniform flow past a sphere. The computational domain is represented by a Cartesian grid with a discretized spherical surface immersed in it. Figure 39 shows the geometry of the two domains, where the Cartesian mesh has been shaded for clarity. The governing equations are solved throughout the

Cartesian volume outside the sphere.

Geometry and boundary conditions

The computational domain consists of a duct with square cross section extending between $-5 \leq x \leq 10$ and $-5 \leq y, z \leq 5$. The sphere with unit diameter D is positioned at the origin of the Cartesian domain. At the inlet section $x = -5$, a Dirichlet type boundary condition is used for the velocity field through the imposition of a constant value U along the x axis. At the outlet section $x = 10$, a Neumann boundary condition setting to zero the velocity variation along the x axis is applied. A zero pressure variation imposed at the outlet section reflects the condition for a fully developed flow. However, a difference in pressure between the inlet and the outlet sections is expected in order to overcome both the viscous drag created around the sphere and the additional resistance due to the presence of a wake downstream the sphere itself. On the four remaining Cartesian boundaries, a zero normal pressure derivative and a constant tangential velocity U are imposed. These conditions imply that the perturbation induced by the sphere on the velocity field around its surface becomes negligible at the border of our domain. This hypothesis is sustained by a simulation performed on a larger computational domain along the y and z axes, defined as $-5 \leq x \leq 10$ and $-7 \leq y, z \leq 7$. The computed solution did not vary when compared to the one obtained using the smaller domain. Similarly, extending the domain upstream of the sphere along the x axis produced no changes in the solution. Conversely, differences appear in case of an extension of the computational domain downstream the sphere. This is due to the facet that the flow field at the outflow section is not fully developed, especially at high Reynolds numbers when the recirculation area increases in length. It will be shown that this inconsistency does not significantly affect the accuracy of the computation when compared to the benchmark solution, probably due to the small normal gradient at the outlet section.

Finally, boundary conditions must be imposed on the sphere surface. Standard no slip Dirichlet conditions are used for the velocity field, while the normal derivative for the pressure values is set to zero. All of the described boundary conditions, implemented using second order approximations in space, are summarized below.

$$\begin{cases} initial\ (t=0) & \mathbf{u}=0 & & p=0 \\ inlet & u=U & v=w=0 & p=0 \\ outlet & \dfrac{\partial \mathbf{u}}{\partial x}=0 & & \dfrac{\partial p}{\partial x}=constant \\ lateral\ surfaces & u=U & v=w=0 & \dfrac{\partial p}{\partial \mathbf{n}}=0 \\ sphere\ surface & \mathbf{u}=0 & & \dfrac{\partial p}{\partial \mathbf{n}}=0 \end{cases}$$

Using D and U as our characteristic length and velocity in the definition of the Reynolds number, the flow field is simulated at Re=50, 100, 200.

Results

A non-uniform mesh of approximately 100x50x50=250k grid points is used. The grid size varies linearly from a value of 0.4 at the boundary of the domain down to a value of 0.025 in the proximity of the sphere. In the box $-0.7 \leq x, y, z \leq 0.7$ enclosing the sphere, the grid size remains constant at 0.025, increasing linearly to 0.05 along the x axis for $0.7 \leq x \leq 2, -0.7 \leq y, z \leq 0.7$. A highly refined mesh in this area is in fact crucial to obtain a detailed description of the recirculation region past the sphere that is expected to be confined here. The sphere surface is discretized with an unstructured triangular mesh whose elements have a side length of approximately 0.05. The computational refinement in the proximity of the sphere allows having a

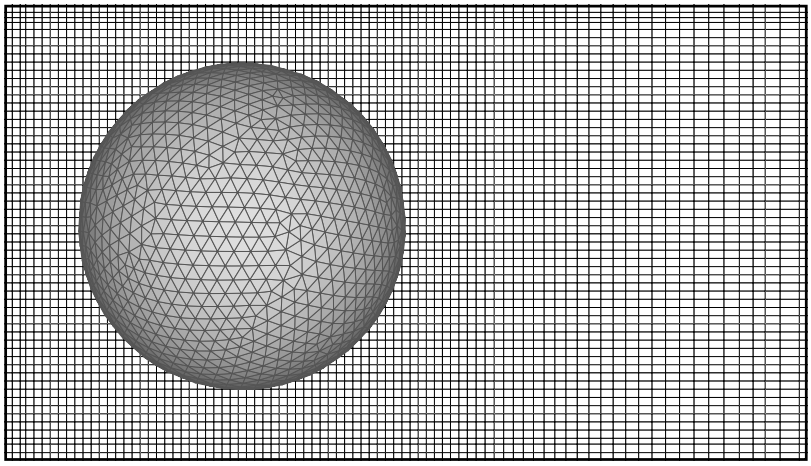

Figure 40: Uniform flow past a sphere with the numerical domain orthogonal mesh close to the interface unstructured mesh.

grid size comparable to the size of the unstructured mesh elements of the spherical interface. As previously described, this is essential for an optimal implementation of our solid-fluid interaction algorithm. Numerical sensitivity tests show that the use of a more refined mesh for the sphere surface does not have appreciable effect on the accuracy of the computed solution. Figure 40 shows the geometry of the numerical domain in the proximity of the sphere. Due to the highly refined computational grid, a significantly smaller pseudo time step must be used in these simulations compared to the previous test cases. This becomes necessary to avoid instability problems of the solution. Each simulation is stopped when a steady state indicated by a stability error $\varepsilon_s < 10^{-3}$ is reached. Similarly to what happened for the lid-driven cavity flow, the error does not converge to a smaller value because of the recirculation area downstream the sphere. Once again, the computational points experiencing the highest errors are clustered in the proximity of the vortex centers, where the velocities are very small. Excluding these points from the stability error computation, a value $\varepsilon_s < 10^{-4}$ is reached. Figure 41 shows the steady state streamlines close to the sphere at Re=50, 100, 200. Our results are compared to the numerical solutions obtained by Johnson [53] and Gilmanov [38], representing our benchmark solutions for this problem. In

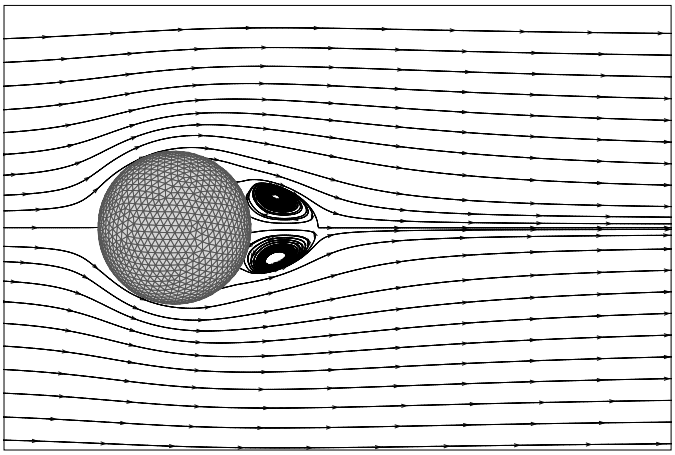

(a)

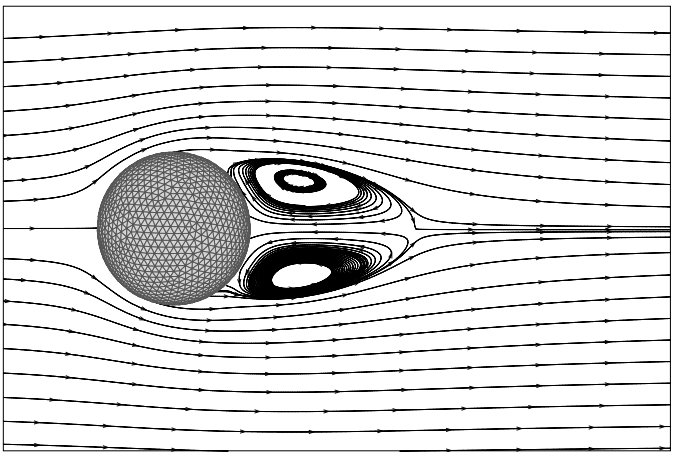

(b)

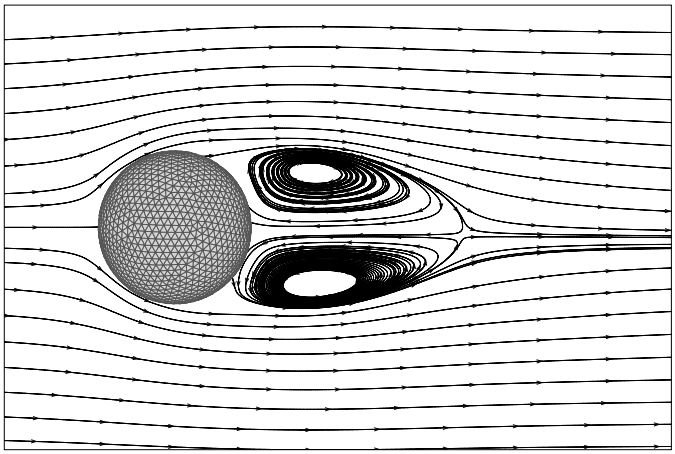

(c)

Figure 41: Flow past a sphere. Streamlines around the sphere at plane z=0: (a) Re=50, (b) Re=100, (c) Re=200.

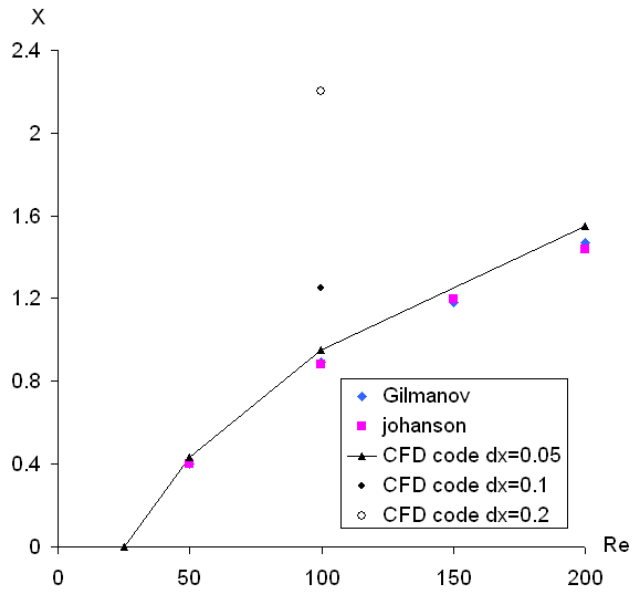

Figure 42: Flow past a sphere. Length of the recirculation zone at different Reynolds numbers and grid refinements.

these works, a "recirculation zone" is defined as the area extending downstream of the sphere up to the duct section where the velocity vector field does not retain any negative component along the main flow direction. As shown in figure 42, the length of the recirculation zone is observed to increase with the Reynolds number, showing a good agreement between the computed and the benchmark solutions. In order to evaluate the recirculation length sensitivity to the Cartesian grid size, increasingly refined meshes were used to compute the flow field at Re=100. The results indicated a decrease in accuracy of the simulation outcomes for coarser computational grids. A mesh size of 0.05 seemed to represent the best compromise between solution accuracy and computational time.

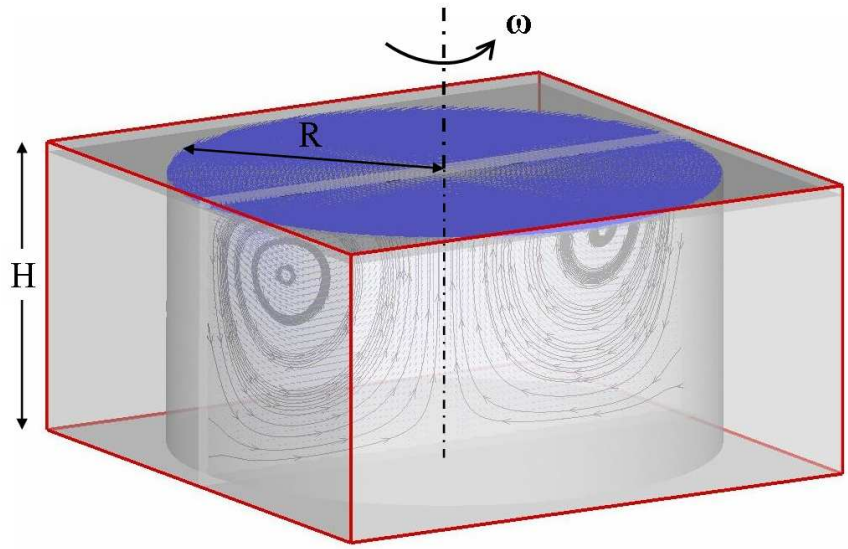

Figure 43: Geometry of cylinder with top wall rotating about its vertical symmetry axis. Flow field is computed inside the immersed solid interface.

5.1.5 Flow induced in a cylinder with top wall rotating - *IB*

This geometry represents a simplified version of the cone-and-plate device. It is used to test our code in a case of a rotating interface immersed inside the computational domain, as shown in figure 43. The governing equations are solved exclusively inside the cylindrical body.

Geometry and boundary conditions

The numerical domain consists of a circular cylindrical chamber with radius to height ratio R/H. On the bottom and side surfaces, fixed wall no-slip boundary conditions are imposed on the velocity field, while the normal pressure derivative is set to zero. On the the top wall, Dirichlet no slip boundary conditions are also implemented, but a constant angular velocity ω with respect to the symmetry axis of the cylinder is imposed. Pressure boundary conditions are the same used on the other surfaces. The overall situation is summarized here below.

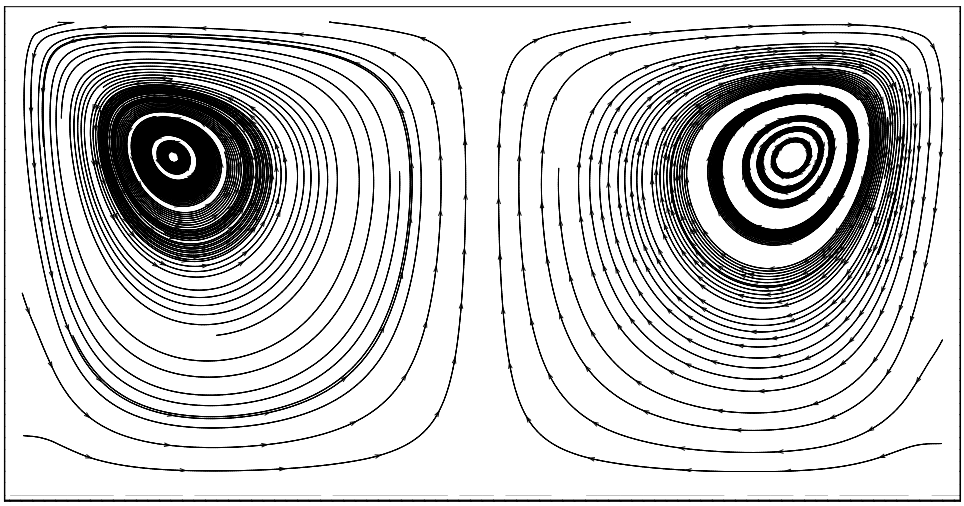

Figure 44: Flow induced in a cylinder with top wall rotating. Curves are the representation of the streamlines projections on a centered vertical section. As expected, the flow field is symmetric respect to the axis of rotation.

$$
\begin{cases}
\textit{initial } (t=0) & \mathbf{u}=0 & & p=0 \\
\textit{top wall} & u_\theta(r)=\omega r \quad u_r=u_z=0 & & \dfrac{\partial p}{\partial \mathbf{n}}=0 \\
\textit{bottom wall} & \mathbf{u}=0 & & \dfrac{\partial p}{\partial \mathbf{n}}=0 \\
\textit{cylinder lateral wall} & \mathbf{u}=0 & & \dfrac{\partial p}{\partial \mathbf{n}}=0
\end{cases}
$$

Following a convention widely accepted in the literature [72, 95, 87], the Reynolds number for this particular geometry is defined as

$$Re = \omega R^2/\nu \tag{97}$$

where R and ω·R are used as our characteristic length and velocity. The flow field is simulated at Re=100.

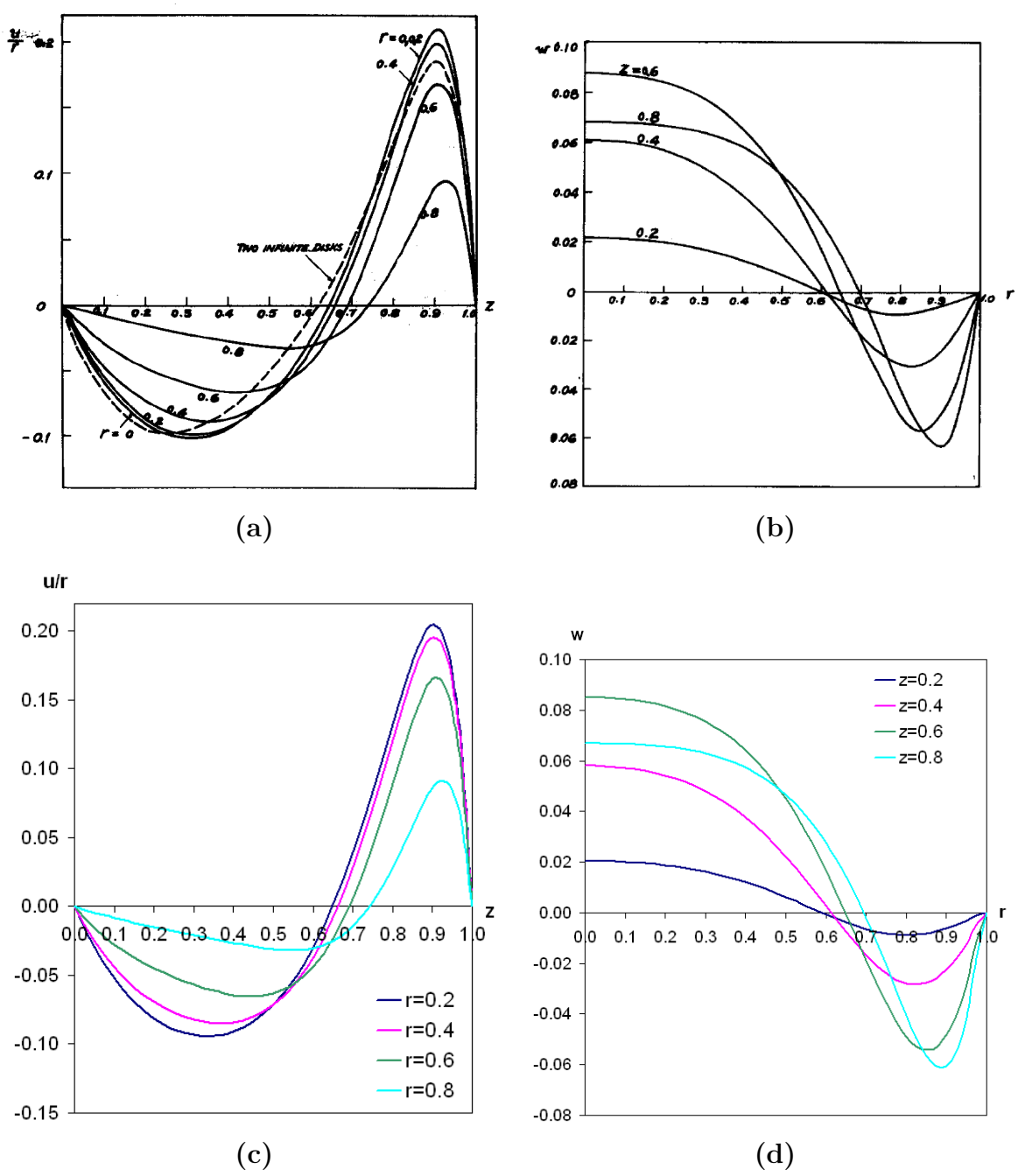

Figure 45: Flow induced in a cylinder with top wall rotating. Top graphs from Pao, bottom graphs from our numerical simulation. (a,c) Radial velocity vs vertical position at different values of r, (b,d) Vertical velocity vs radial position at different values of z.

Results

For this simulation, the radius to height ratio is set to one. A computational mesh uniform along each of the Cartesian directions is built, and its grid size kept constant to R/40 throughout the whole domain. This results in a numerical grid of approximately 250K computational points. The computation is considered to have reached a steady state when a pointwise stability error $\varepsilon_s < 10^{-4}$ is achieved. One first attempt to consider an error $\varepsilon_s = 10^{-3}$ small enough to obtain stability miserably failed, providing us with a misleading solution. A more accurate analysis of the real time evolution of the computed flow field showed how the solution was still changing in time, although this was happening very slowly. Once an error $\varepsilon_s < 10^{-4}$ is afterwards reached, the instantaneous velocity variations are only considered numerical fluctuations. The computed radial and vertical velocities at different values of radius and vertical position are compared with the data obtained by Pao, considered our benchmark solution for this problem [72]. Figure 45 shows a very good agreement between the two sets of data for both radial and vertical velocities. In addition, figure 44 shows the flow field on a vertical section passing through the axis of rotation of the cylinder. Despite the use of a fully 3D numerical code that does not use any symmetry hypothesis, it must be observed how the computed flow field is axisymmetrical, as logically expected.

5.1.6 Womersley flow on an oscillatory regime - *IB*

All of the previous validation tests have been carried on for steady state flow regimes. The reliability of the CFD code must now be assessed under unsteady flow conditions. For this purpose, the pressure-driven oscillatory flow of a viscous fluid in a straight, rigid, circular tube is simulated. The computational domain is equivalent to the one used for the steady state Poiseuille flow simulation already described in section 5.1.3,

but the different boundary conditions will lead to different solutions.

Geometry and boundary conditions

Recalling the Poiseuille geometry, the length of the tube is four times the diameter of its circular cross section, named D. On the cylinder lateral surface, no slip boundary conditions are once again imposed on the velocity field, while the value for the pressure variation along the normal is set to zero. Neumann boundary conditions are implemented at both the inlet and the outlet Cartesian sections through the imposition of a zero derivative for the velocity values along the longitudinal axis of the tube. Pressure is still treated using Dirichlet type boundary conditions, but for this problem a periodically oscillating value is imposed at the inlet. The outlet pressure value is sill set to zero. At the initial instant of time, the Poiseuille steady-state solution corresponding to the first imposed value of inlet pressure $p = p(0^+)$ is used. The overall boundary and initial conditions are summarized here below,

$$\begin{cases} initial\ (t=0) & Poiseuille\ steady\text{-}state\ solution \\ inlet & \dfrac{\partial \mathbf{u}}{\partial x} = 0 \qquad p = \dfrac{P_M - P_m}{2}\ cos(\omega t) + \dfrac{P_M + P_m}{2} \\ outlet & \dfrac{\partial \mathbf{u}}{\partial x} = 0 \qquad p = 0 \\ cylinder\ lateral\ surfaces & \mathbf{u} = 0 \qquad \dfrac{\partial p}{\partial \mathbf{n}} = 0 \end{cases} \tag{98}$$

where P_M and P_m represent respectively the maximum and the minimum inlet pressure values during a whole cycle. Let's define U as the maximum velocity across one pressure cycle expected at the tube centerline. Using D and U as our characteristic

length and velocity in the definition of the Reynolds number, the simulations are performed at Reynolds numbers never exceeding Re=30. In addition, due to the periodic nature of the simulation, a new dimensionless number must be considered; the Womersley number. This is defined as the ratio between the unsteady inertial and the viscous forces acting on the fluid, namely

$$W = R\sqrt{\frac{\omega}{\nu}} \tag{99}$$

where ω represents the pulsation, or angular frequency, of the periodic motion and ν the kinematic viscosity of the fluid. Simulations with a Womersley number ranging from W=0.6 to W=3.5 will be carried out.

Results

As for the Poiseuille test case, each simulation is performed on a uniform mesh whose grid size is D/20, resulting in a computational mesh of about 75k cells. The cylinder surface is discretized with an unstructured triangular mesh whose elements have a side length equivalent to the Cartesian grid spacing. Since we are dealing with a numerical solution periodically changing in time, the definition of the stability error must be modified. Condition for the solution to be stable is that the computed flow field does not change in value from one cycle to another. The pointwise stability error at time n is therefore defined as

$$\varepsilon_s = \max_{i,j,k} \frac{|\mathbf{u}^n_{i,j,k} - \mathbf{u}^{n-T}_{i,j,k}|}{|\mathbf{u}^n_{i,j,k}|} \tag{100}$$

where T represents the period of the oscillation

$$T = \frac{1}{f} = \frac{2\pi}{\omega} \qquad\qquad f = frequency \tag{101}$$

The computation is considered to have reached stability when a pointwise error $\varepsilon_s < 10^{-5}$ is achieved. At this time, the developed flow field will be homogeneous across the tube longitudinal axis, and a global conservation of mass is ensured at any successive instant of time. The difference between the inflow and the outflow will be constantly kept lower than one percent. Our results are thus compared to the analytical values computed by Womersley in the mid fifties, here considered our benchmark solutions [97, 98]. Womersley showed how, in a tube sufficiently long in relation to its diameter, no radial nor tangential motion of the liquid will be present, and the axial velocity along the tube will be independent of the section where it is computed. Given a pressure gradient per unit length

$$\frac{\Delta p}{L} = M cos(\omega t) \tag{102}$$

the resulting velocity can be expressed as

$$u(r) = \frac{M}{\mu}\frac{R^2}{W^2}\ M_0'(r)\ sin(\omega t + \varepsilon_0) \tag{103}$$

where M_0' and ε_0 are functions of the modules and phases of the solution for the zero-order Bessel functions of complex arguments [66]. Since $\varepsilon_o = \varepsilon_0(r)$, the phase delay between the input and a generic section waveforms varies across the pipe, and is computed as

$$\Delta\phi(r) = \varepsilon_0(r) - \frac{\pi}{2} \tag{104}$$

The limiting form of this solution for small Womersley numbers is given by a quasi-steady Poiseuille equation

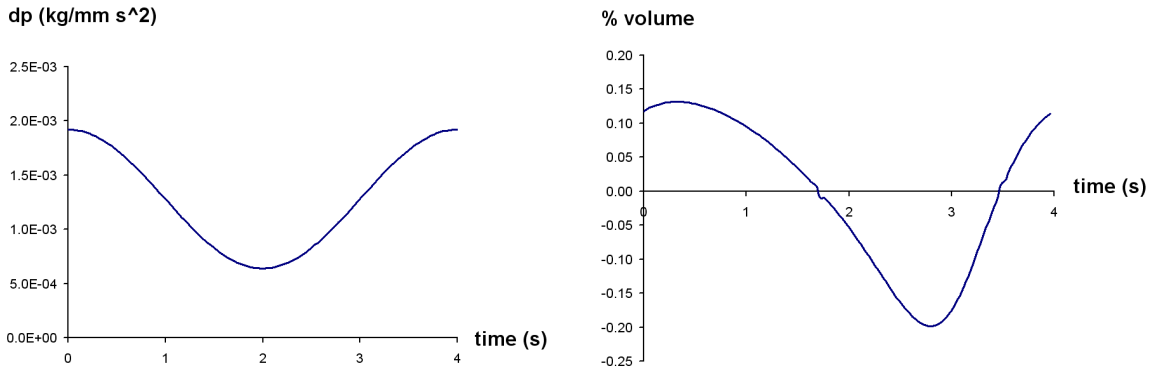

(a) **(b)**

Figure 46: Simulation performed at Womersley number W=0.6 (a) Input pressure waveform and (b) evolution in time of the percentage volume leak.

$$u(r) = \frac{1}{4\mu} M(R^2 - r^2)\ cos(\omega t) \tag{105}$$

This implies that for low frequency of the imposed pressure gradient, a quasi-steady solution must be expected, miming the velocity profile solution of the steady state Poiseuille equation driven by the instantaneous pressure gradient. The maximum velocity will thus still be reached along the centerline of the tube. Conversely, for increasing values of the Womersley number, the effect of the unsteady inertial forces should start overcoming the viscous forces in the fluid, leading to more complex time-dependent flow patterns. The point of instantaneous maximum velocity on each section of the tube will move back and forth towards the periphery wall, depending on the considered instant of time, and a phase delay with respect to the input waveform will arise. Let's now simulate the flow field under two different pressure gradient waveforms.

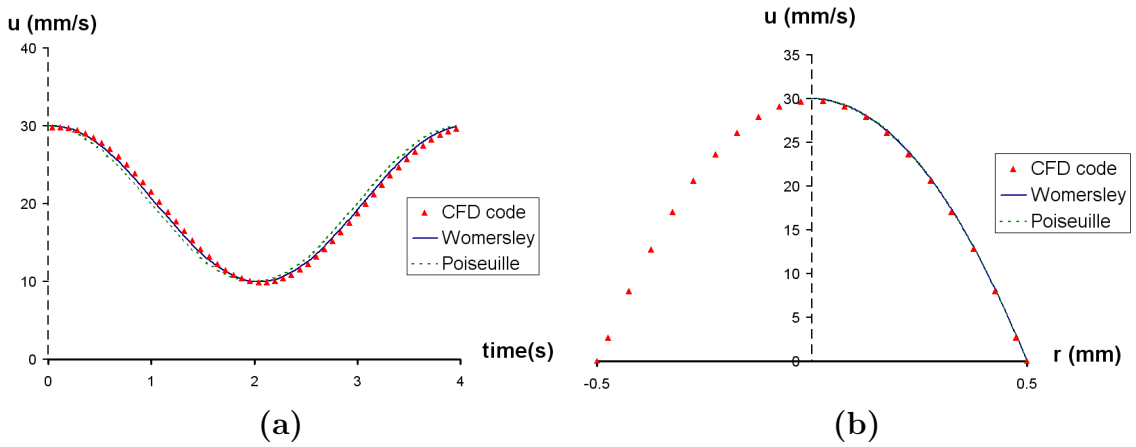

Figure 47: Oscillatory flow in a pipe at Womersley number W=0.6. Evolution in time of the velocity at the pipe centerline (a) and velocity profile at the time of maximum pressure gradient (b).

(1) W=0.6 - pressure gradient always positive

Following the notations given in (98), a pressure gradient oscillating at a pulsation $\omega = \pi/2$ ($\rightarrow T = 4s$) is imposed between the inlet and the outlet sections. The resulting Womersley number for this simulation is then $W = 0.6$, while the maximum and minimum pressure gradient values are set to

$$P_M = 1.92 \cdot 10^{-3}\ kg/(mm \cdot s^2) \quad \longrightarrow \quad u_{max} = 30mm/s$$
$$P_m = 0.64 \cdot 10^{-3}\ kg/(mm \cdot s^2) \quad \longrightarrow \quad u_{min} = 10mm/s$$

as illustrated in figure 46 (a). Due to the low Womersley number, a resulting quasi-steady flow field is expected. Here above, the maximum and minimum velocities at the tube centerline derived from the analytical quasi-steady Poiseuille solution (105) are also given. In figure 47, both the evolution in time of the fluid velocity at the tube centerline and the velocity profile along a generic section computed at a the time of maximum pressure gradient are presented. The two curves are compared to the Womersley analytical solution, revealing a good accuracy of the computation

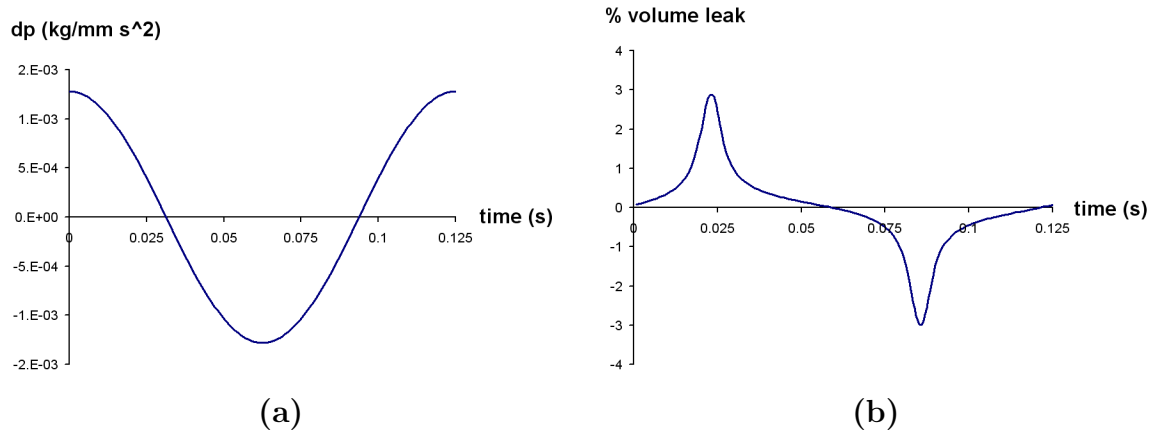

(a) (b)

Figure 48: Simulation performed at Womersley number W=3.5 (a) Input pressure waveform and (b) percentage volume leak.

results. In addition, the quasi-steady Poiseuille solution indicated in equation (105) is shown on the same plots. The great fit between these curves and the computed data output strongly confirm our hypothesis of quasi-steady flow field at this low Womersley number. The volume leak between the inlet and the outlet sections along a pressure cycle is also presented in figure 46 (b), proving once again the conservative character of the numerical code.

(2) W=3.5 - pressure gradient switching from positive to negative

To test the code performance for higher frequencies, a pulsation $\omega = 16\pi$ ($\rightarrow T = 0.125s$) is now imposed, resulting in a Womersley numbers $W = 3.5$. The maximum and minimum pressure gradient values are now set to

$$P_M = 1.28 \cdot 10^{-3}\ kg/(mm \cdot s^2) \quad \longrightarrow \quad u_{max} = 20mm/s$$
$$P_m = -1.28 \cdot 10^{-3}\ kg/(mm \cdot s^2) \quad \longrightarrow \quad u_{min} = -20mm/s$$

defining the waveform illustrated in figure 48 (a). In this case, as opposed to the previous simulation, the flow periodically inverts direction inside the tube. The limit

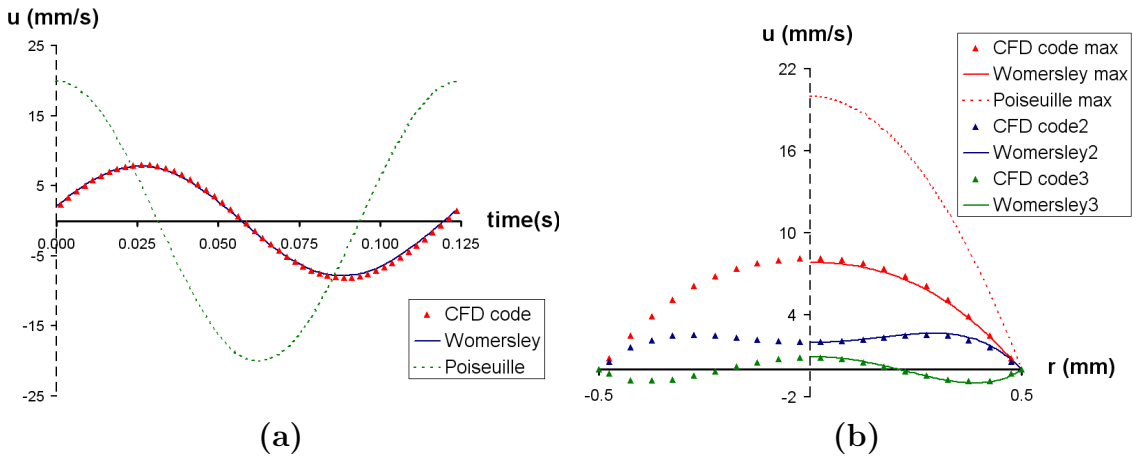

Figure 49: Oscillatory flow in a pipe at Womersley number W=3.5. Evolution in time of the velocity at the pipe centerline (a) and velocity profiles at different instants of time (b).

velocity values at the tube centerline for the quasi-steady Poiseuille flow (105) are also indicated. Similarly to what was done for the previous simulation, in figure 49 (a) the evolution in time of the fluid velocity at the tube centerline is compared to the Womersley solution, exhibiting a good solution accuracy. In the same picture, the quasi-steady Poiseuille solution is also plotted. It is here evident that now, due to the high pressure frequency, the flow does not have the time to fully develop, and the resulting velocity field strongly differs from the quasi-steady situation. This becomes more evident by observing that the differences in the peak velocity value are significantly reduced. In addition, the velocity output exhibits a nonhomogeneous phase delay developing across the pipe when compared to the inlet pressure waveform. In figure 49 (b), velocity profiles at different instants of time are shown with the correspondent Womersley solutions, still demonstrating a good data fit. Finally, figure 48 (b) shows the volume leak between the inlet and the outlet sections. Despite its higher value when compared to the previous simulation, a reasonable range between $\pm 3\%$ is obtained.

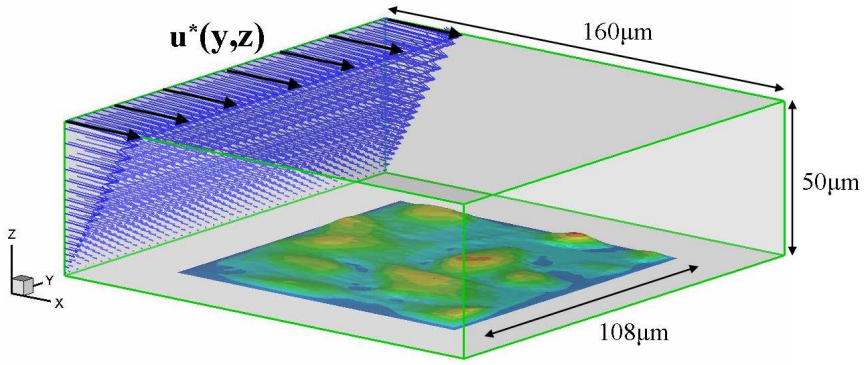

Figure 50: Reduced sector of the original cone-and-plate geometry. Endothelial cells are visible on the bottom surface. For clarity, the computational mesh has been shaded.

5.2 cone-and-plate simulation

At this point of the thesis, the numerical code has been successfully tested by running standard test cases of increasing geometrical and physical complexity. The excellent agreement between the computed and the "benchmark" solutions makes us confident about the ability of the code to compute accurate results for flow conditions whose solutions are still missing in the up-to-date scientific literature.

The next step is then to investigate the flow field that develops on a layer of confluent endothelial cells during a typical experiment performed in a cone-and-plate device, as introduced in section 4.2.1. The flow conditions will be simulated for both steady and unsteady rotation imposed by the cone surface.

5.2.1 Steady state

The simulation of the flow field produced by a cone rotating at a steady angular velocity is first considered. The computational domain, illustrated in figure 50, is represented by a Cartesian grid, where a cluster of endothelial cells is discretized and immersed in it. The remarkable difference in size between the endothelial cell height and the vertical extension of the Cartesian domain makes it difficult to appreciate

the 3D cells features, better visible in the next pictures.

Cells discretization

In collaboration with Dr. Jo's "Vascular, Heart Valve, and Bone Mechanobiology Laboratory" at Emory university, it was possible to obtain six samples from cultured human umbilical vein endothelial cells (HUVEC). Some of them were "fixed " in order to increase their stiffness, while others were kept alive inside the same type of biological media used to grow them. None of the samples was sheared in the cone-and-plate device. All of the samples were then brought to Dr. Riedo's "Picoforce lab" at the Georgia Tech School of Physics to be imaged using their AFM (atomic force microscopy) facility.

As illustrated in figure 51, an area of $108\mu m \times 108\mu m$ was scanned for each sample at a resolution of $0.85\mu m$, resulting in a 128x128 data set matrix. Due to the dragging of the cantilever tip across the cells surface, some of the samples were damaged. In addition, the cantilever tip itself got frequently contaminated by binding to random membrane molecules. As a consequence, only two of the six original samples finally provided good enough images to be used for our computational purposes. The output obtained from the AFM software consists of a square matrix $A(n \times n)$ representing the topography of the imaged sample. The a_{ij} element indicates the vertical position of the cantilever tip when scanning the specific point on the cell layer associated with the indexes of the matrix element,

$$a_{ij} = z(x,y) \begin{cases} x = (i-1)\Delta x & i = 1....n \\ y = (j-1)\Delta y & j = 1....n \end{cases} \tag{106}$$

where Δx and Δy represent the scanning resolutions along the two axes.

These data were then imported into the *Gambit* pre-processor software. In order

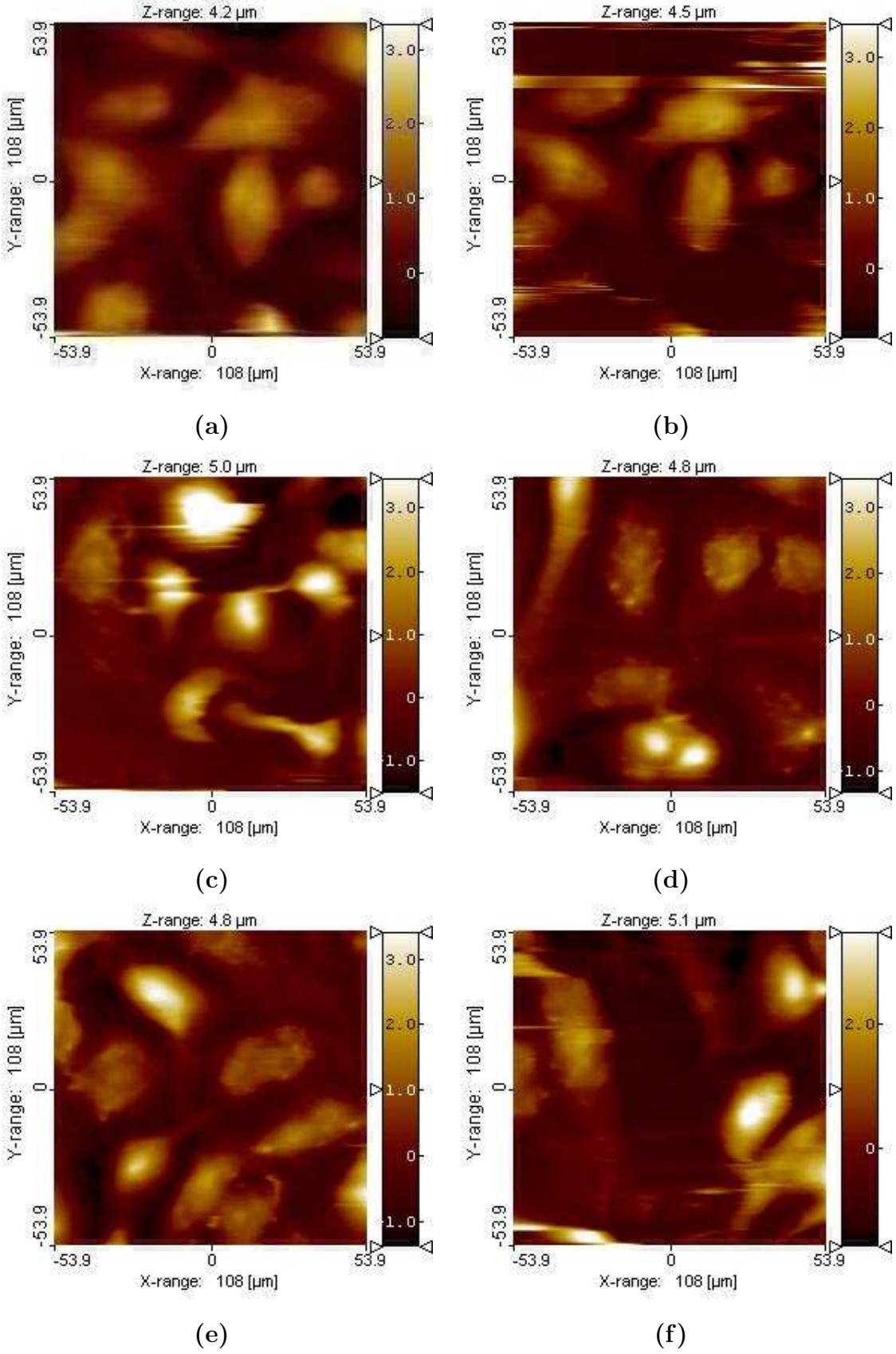

Figure 51: AFM images from alive (a,b) and fixed (b,c,d,e) samples of HUVEC.

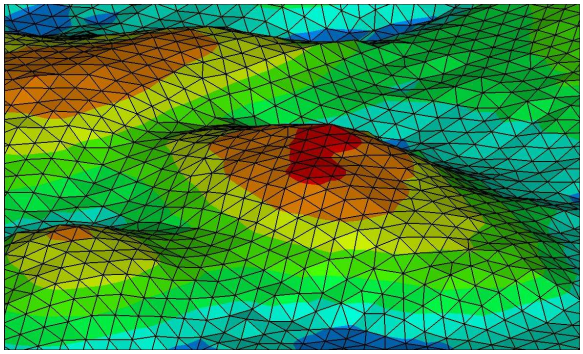

Figure 52: Particular of the triangular mesh on a single cell. The axes have been scaled at $x : y : z = 1 : 1 : 0.4$.

to create the 3D geometry representing the cells surface, two successive *spline* interpolations along the x and y axes are implemented. The resulting surface is thus meshed using triangular elements whose average size is $\sim 2\mu m$. More refined meshes were also tested, but, as it will be explained later, they did not improve significantly the accuracy of the computational outputs. The cells surface geometry is now ready to be "immersed" in the computational domain. In figure 52, the dicretization pattern around a single cell is presented.

Geometry and boundary conditions

The computational domain consists of a parallelepiped with square base extending between $70\mu m \leq x, y \leq 230\mu m$ and $0\mu m \leq z \leq 50\mu m$. The discretized sample of endothelial cells is centrally positioned on its bottom surface. Recognizing that this surface represents a sector of the real plate, it is straightforward to impose no slip boundary conditions on it. When trying to impose boundary conditions on the remaining top and lateral surfaces, we have to face the problem that these surfaces are in the interior of the original cone-and-plate domain, and thus no velocity values are given from simple physical considerations. The idea to overcome this difficulty is to simulate the flow field inside the entire cone-and-plate domain with no cells lying on the plate surface, using a coarser numerical grid. The computed values will thus be

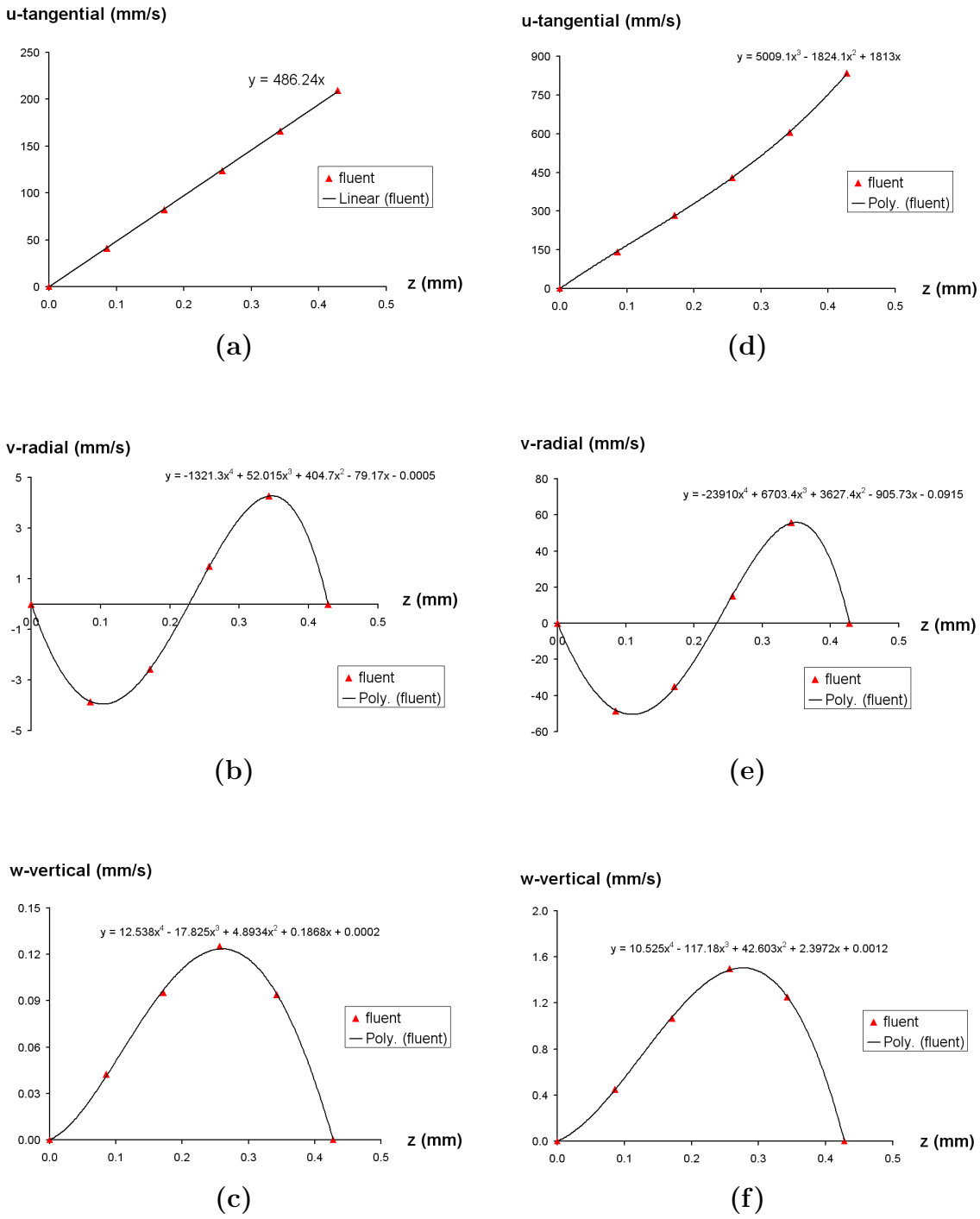

Figure 53: Velocities vs vertical position in the cone-and-plate section r=20mm. Computed by *Fluent* for (a,b,c) 100rpm and (d,e,f) 400rpm.

interpolated to obtain the boundary conditions to be imposed on our reduced geometry. This approach is based on the hypothesis that the presence of the endothelial cells does not affect the flow field inside the device at a reasonable distance from them. Thanks to the precious collaboration of Dr. Suo Jin, a research scientist in Dr. Giddens' "Cardiovascular Biofluid Dynamics Laboratory", these solutions were obtained using *Fluent* software for two different angular velocities of the rotating device: $100rpm$ and $400rpm$. The output velocities at the radial position $r = 20mm$ and their interpolation formulas along the vertical direction are shown in figure 53, providing the real cone-and-plate geometry described in section 4.2.

Suitable velocity boundary conditions to impose on our numerical domain are now available. Because of the cone-and-plate symmetry along the tangential direction, a zero pressure variation is imposed at both the inlet and outlet sections, and a constant normal pressure derivative on the top and lateral Cartesian boundaries. As previously stated, these conditions imply that the perturbation induced by the cells on the velocity field around them becomes negligible at the border of our domain. This hypothesis is confirmed by running multiple simulations on differently sized domains. The computed solutions were compared at random check points common to all of the domains, and a similar behavior was observed. Finally, boundary conditions must be imposed on the cells surface. Standard no slip Dirichlet conditions are used for the velocity field, while the normal derivative for the pressure values is set to zero. Addressing the cone-and-plate steady-state solution computed by *Fluent* with the symbol (*), all of the described boundary conditions, implemented using second order approximations in space, are summarized below.

$$
\begin{cases}
initial\ (t=0) & steady\text{-}state\ solution\ with\ no\ cells\ (*) & \\
inlet(x=70\mu m) & \mathbf{u}=(*) & \dfrac{\partial p}{\partial x}=0\ (p_{point}=0) \\
outlet(x=230\mu m) & \mathbf{u}=(*) & \dfrac{\partial p}{\partial x}=0 \\
top/lateral\ surfaces & \mathbf{u}=(*) & \dfrac{\partial p}{\partial \mathbf{n}}=constant \\
bottom\ surfaces & \mathbf{u}=0 & \dfrac{\partial p}{\partial \mathbf{n}}=0 \\
cells\ surface & \mathbf{u}=0 & \dfrac{\partial p}{\partial \mathbf{n}}=0
\end{cases}
$$

Following a convention widely accepted in the literature, the Reynolds number for the cone-and-plate experiments is defined as the ratio of the characteristic centrifugal forces to the viscous forces acting on the fluid at any radius from the center [19, 11, 88]. Working on forces per unit volume, it can be expressed as

$$
Re=\frac{r^2\Omega\alpha^2}{\nu} \Leftarrow \begin{cases} f_c=\dfrac{\rho u_\theta^2}{r}\sim \rho r\Omega^2 \\ \\ f_v=\dfrac{\mu u_\theta}{h^2}\sim \dfrac{\mu\Omega}{r\alpha^2} \end{cases} \tag{107}
$$

where α and Ω represent respectively the cone angle and angular velocity, r the radial position and ν the kinematic viscosity of the fluid. In order to reproduce the real environment experienced by the endothelial cells in the cone-and-plate device, the density and viscosity values characteristic of the biological media used in the experiments are used, namely $\rho=1.02\cdot 10^{-6}kg/mm^3$ and $\mu=7.8\cdot 10^{-7}kg/(mm\cdot s)$. Simulations at $100rpm$ and $400rpm$ were run, resulting in a Reynolds number ranging from Re=0.42

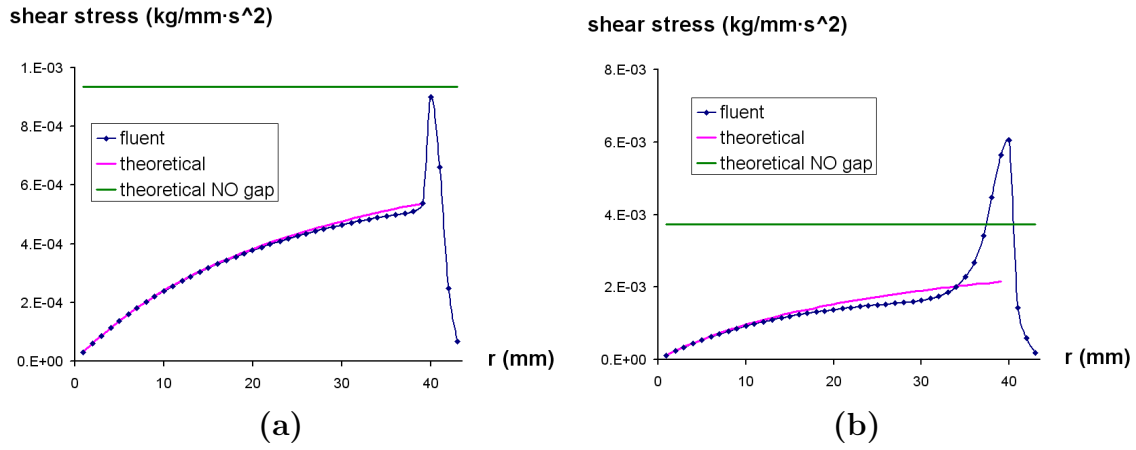

Figure 54: Shear stresses vs radial position on the plate with no cells. Computed by *Fluent* for (a) 100rpm and (b) 400rpm. The theoretical values are computed assuming purely tangential primary flows. As expected, the theoretical wall shear stress on the plate surface is constant throughout the whole domain when no gap is present.

to Re=1.7.

Results

A non-uniform mesh of approximately 80x80x40=256k grid points is used for the most accurate simulation in case of angular velocity $100rpm$. The grid size along the x and y directions is kept constant at a value of $2\mu m$. Along the vertical direction, it varies from a value of $0.5\mu m$ in the proximity of the endothelial cells up to $3\mu m$ at the top boundary of the domain. The cells surface is discretized with an unstructured triangular mesh whose elements have a side length of approximately $1\mu m$. Due to the highly refined computational grid, a very small pseudo time step of $\Delta t = 10^{-7}s$ must be used in order to avoid instability problems of the solution. The simulation is stopped when a steady state with a pointwise stability error $\varepsilon_s < 10^{-5}$ is reached. The computed shear stress field is then "compared" to the solution obtained with Fluent, when no cells are present in the domain. As illustrated in figure 54, its value is

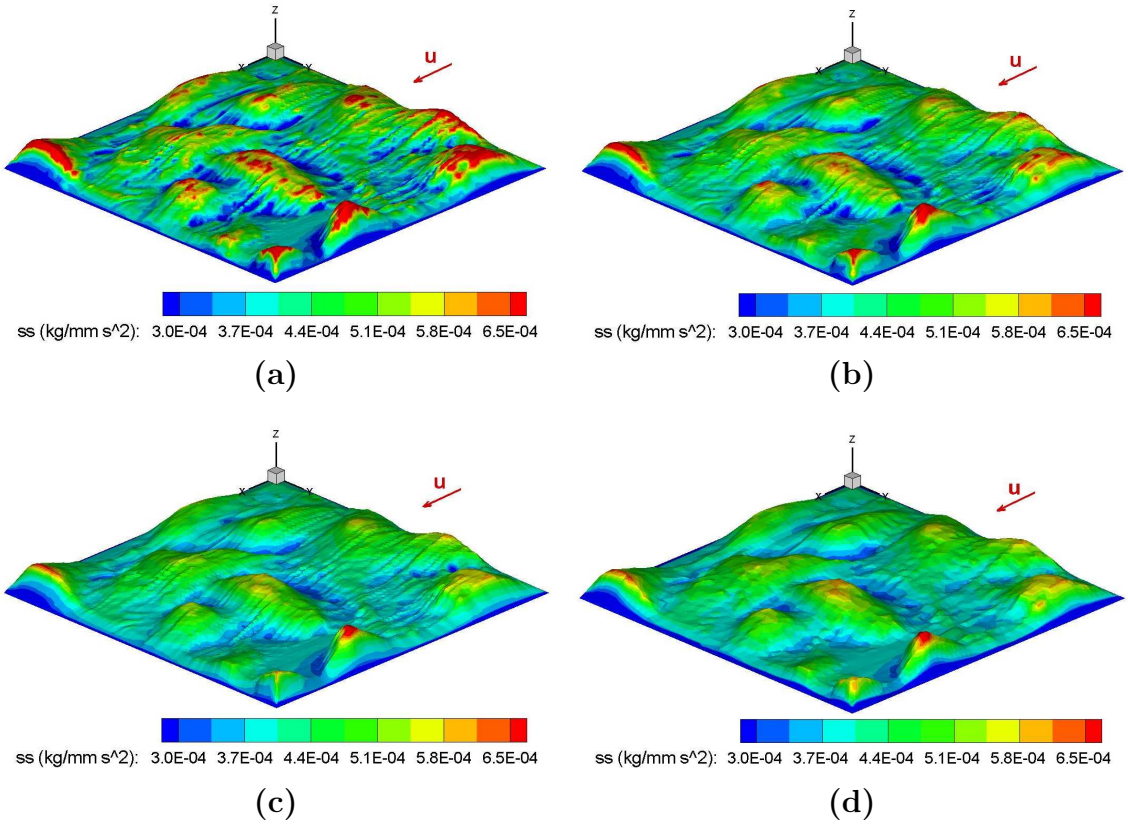

Figure 55: Contour plots for the shear stress distribution on the cells surface computed at 100rpm. Moving from simulation (a) to (d), both Cartesian and interface meshes become coarser, resulting in an overall decrease in the computational accuracy. For a detailed description of the used meshes, refer to the table presented in the text.

$$\tau_{w\_no\_cells}(r = 20mm) \sim \begin{cases} 3.77 \cdot 10^{-4} \dfrac{kg}{mm \cdot s^2} = 3.77 \dfrac{dynes}{cm^2} & at\ 100rpm \\ 1.38 \cdot 10^{-3} \dfrac{kg}{mm \cdot s^2} = 13.8 \dfrac{dynes}{cm^2} & at\ 400rpm \end{cases}$$

Figure 55 (a) shows a contour plot for the shear stress distribution on the cells surface. It must be noted that, in order to obtain a smooth transition zone between the meshed cells and the domain bottom wall representing the plate surface, the four lateral borders of the cells surface have been smoothed up to a zero vertical elevation.

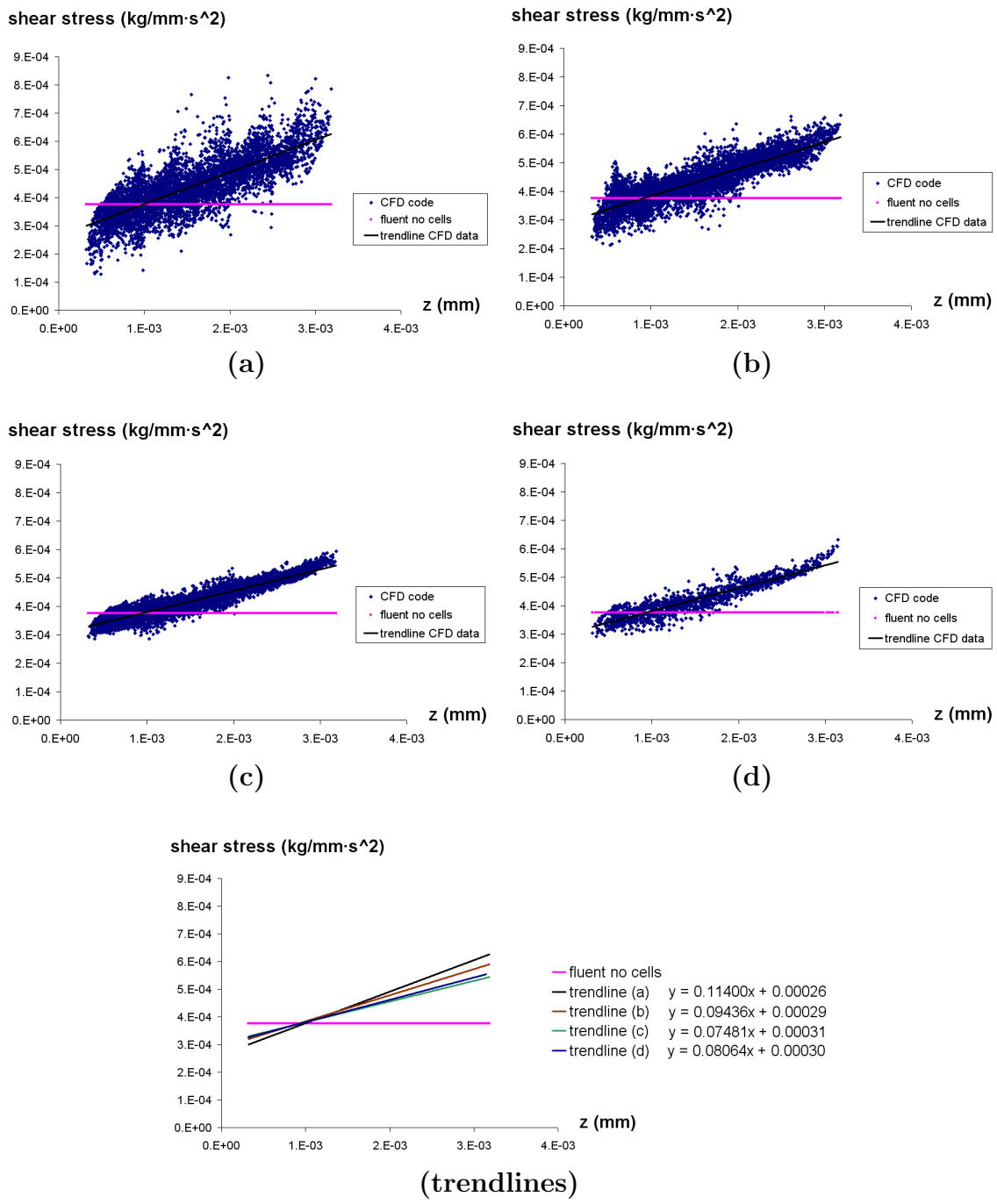

Figure 56: Shear stresses as a function of the vertical elevation on the cells surface computed at 100rpm. Moving from simulation (a) to (d), both Cartesian and interface meshes become coarser, resulting in an overall decrease in the computational accuracy. In the bottom graph, all of the linear regression lines for the shear stress obtained from the different meshes are compared. For a detailed description of the grid sizes, refer to the table presented in the text.

Nevertheless, the real situation would include a continuous layer of cells, each of them feeling the presence of its upstream and downstream neighbors. As a consequence, the shear stress values computed on those cells closest to the interface borders lack a real physical significance, and thus will be ignored in our analysis. Only the shear stresses computed in the central zone $0.2L < x, y < 0.8L$, were L defines the side length of the squared cells interface, are considered. As expected, peak shear stress areas are clustered around the highest points of each endothelial cell, experiencing values up to twice the value measured on the plate in the absence of a cell layer. Oppositely, depression areas express the lowest values of shear stress, as low as half of $\tau_{w\_no\_cells}$. The situation is illustrated in figure 56 (a), where the wall shear stress values are plotted as a function of the vertical coordinate of the point being considered. The overall trend for the shear stress is to increase as a linear function of the vertical elevation, as indicated by a correlation coefficient value $r = 0.8$. Nevertheless, a significant scattering of the data around the regression line is present, and it may be interpreted as a "local" effect, that is dependent on the micro-scale contours. This suggests that the neighboring endothelial cells play a key role in the determination of the shear stress distribution. As a consequence, the shear stress over a layer of endothelial cells may be considered as the result of two concurrent effects, one acting at a local micro-scale field and the other providing a macro-scale shear stress distribution that increases linearly with the cell elevation.

In order to evaluate the shear stress sensitivity to both the Cartesian ($\Delta x/y/z$) and the interface ($\Delta mesh$) mesh size, the same simulation is carried out using the other three different sets up (b-c-d) listed below

	$\Delta x = \Delta y$	Δz	$\Delta mesh$	Δt
Simulation (a)	$2\mu m$	$0.5\mu m$	$1\mu m$	$t = 10^{-7}s$
Simulation (b)	$2\mu m$	$1\mu m$	$1\mu m$	$t = 10^{-6}s$
Simulation (c)	$2\mu m$	$2\mu m$	$1\mu m$	$t = 10^{-6}s$
Simulation (d)	$4\mu m$	$2\mu m$	$2\mu m$	$t = 10^{-5}s$

Due to the use of these coarser meshes, it was possible to reach stability of the solution using larger time steps, as indicated in the table. This fact will become fundamental when simulating flow fields under unsteady conditions. The time step will then represent its actual "physical" significance, and a reasonable computational time will strongly depend on its value. The computed shear stress fields are once again presented in figures 55, where the color scales have been kept constant for an easier comparison. All of the computations exhibit similar shear stress distributions, although small variations in values are present. An accurate analysis leads to the conclusion that a single step decrease in grid accuracy ($a \rightarrow b$, $b \rightarrow c$, $c \rightarrow d$) causes errors never exceeding 4%. When comparing the most and the least accurate meshes, errors up to 13% will arise. These errors reflect the loss of information at the micro-scale level when coarser meshes are used, while the macro-scale linear dependency of the shear stress on the vertical elevation is retained. These considerations are sustained by the data plotted in figure 56, where again wall shear stress values are presented as a function of the vertical coordinate of each point on the cell surface. A comparison between all of the regression lines computed for the different meshes is also presented.

The same approach is used to reproduce the flow field on the cells layer for the cone rotating at a constant velocity of $400rpm$. Two simulations are performed using the time and space discretizations listed below.

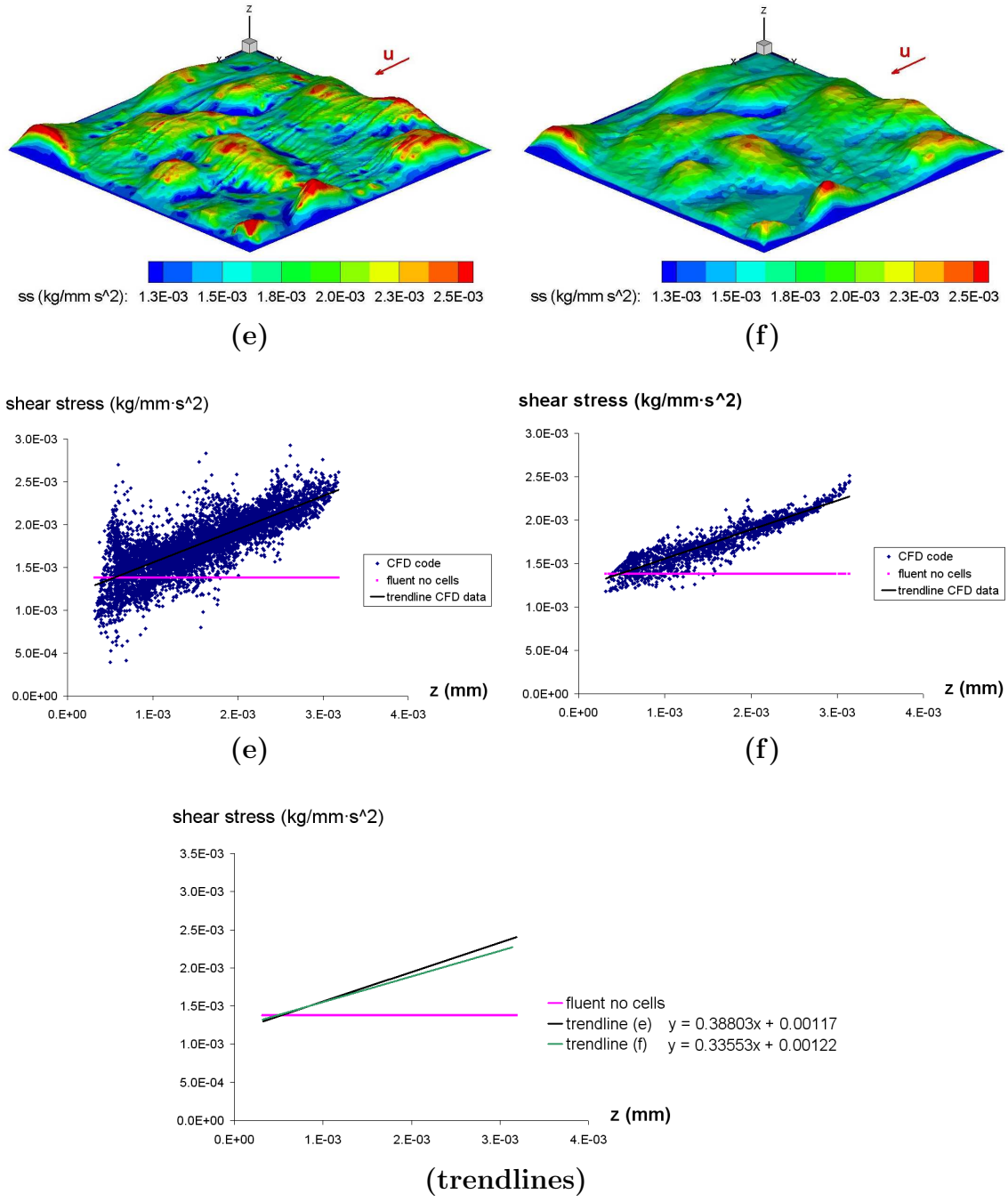

Figure 57: Contour plots for the shear stress distribution on the cells surface computed at 400rpm. Moving from simulation (e) to (f), both Cartesian and interface meshes become coarser, resulting in an overall decrease in the computational accuracy. Shear stresses are also presented as a function of the vertical elevation. In the bottom graph, all of the linear regression lines for the shear stress obtained from the different meshes are compared. For a detailed description of the meshes used, refer to the table presented in the text.

	$\Delta x = \Delta y$	Δz	$\Delta mesh$	Δt
Simulation (e)	$2\mu m$	$1\mu m$	$1\mu m$	$t = 10^{-6}s$
Simulation (f)	$4\mu m$	$2\mu m$	$2\mu m$	$t = 10^{-5}s$

Once again, the computed shear stress field illustrated in figure 57 is "compared" to the solution obtained with *Fluent* when no cells are present on the plate. Similarly to results from the slower cone rotation, peak shear stress areas are clustered at the highest points on the single cells, expressing values up to twice the value measured on the plate in the absence of cells. While at low rotational speed the data scattering was homogeneous around the regression line, the increase in cone velocity causes the the depression areas to express a spreader data distribution, as opposed to the points at high elevation. This results in a stronger effect on the areas of low shear stress, where values down to one third of $\tau_{w\_no\_cells}$ are reached.

Remark on the inside/outside interface algorithm

Before moving on to simulate the oscillating regime, we want to give a "visual" example of how the algorithm that classifies points as inside or outside any immersed interface works. Due to the complicated geometry involved in the cells discretization, this case represents a good test to check the performance of the algorithm. In figure 58 (a), five generic planes belonging to the Cartesian grid are represented. Some of their points are physically inside the cells interface, while others will be in the fluid phase. After the scanning performed by the involved algorithm, each point is assigned a flag whose value can be

$$\begin{aligned} flag = 0 \quad &\Rightarrow \quad outside\ the\ interface \\ flag = 1 \quad &\Rightarrow \quad inside\ the\ interface \end{aligned}$$

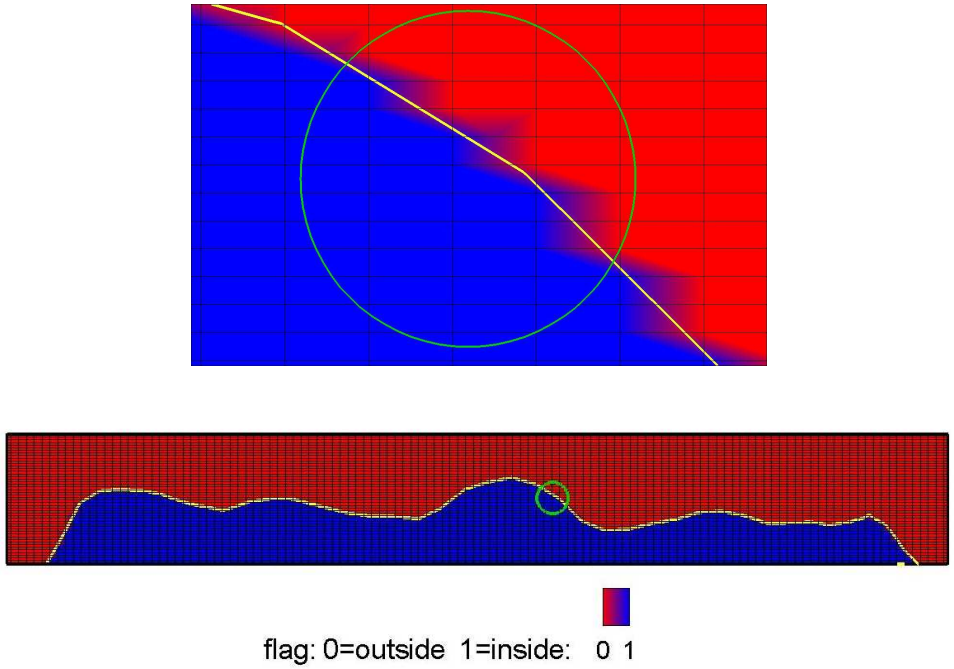

(b)

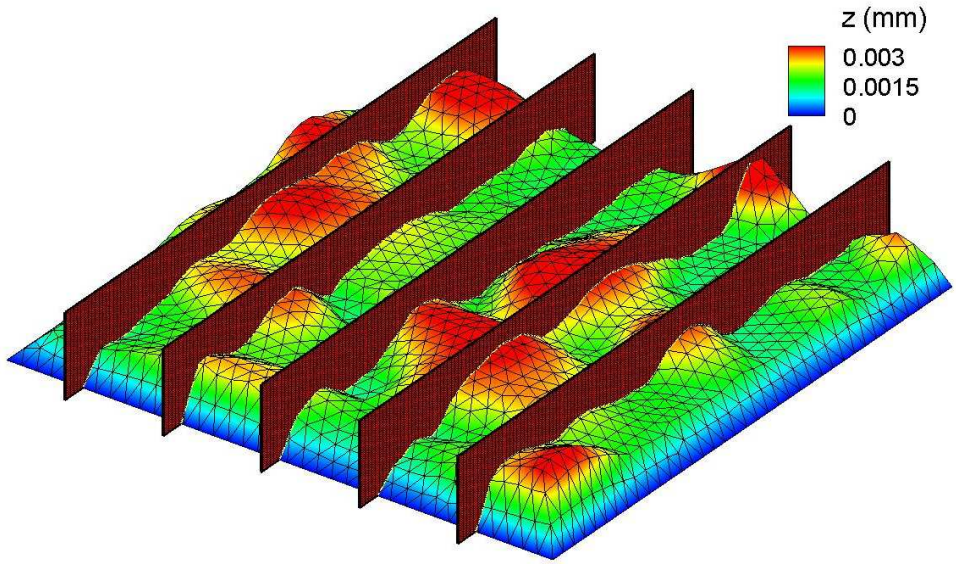

(a)

Figure 58: (a) Random planes of the computational grid slicing the interface mesh. Each point on these planes must be classified as inside or outside the interface. (b) View of a single plane intersecting the cell surface. The yellow line represents the real intersection between the meshed 3D surface and the considered plane. The circled area is further magnified for an easier interpretation.

The computed flag-field is illustrated in figure 58 (b), where the exact intersection between one of the cutting planes and the cells surface is also shown. The algorithm proves to be very reliable under generic geometrical conditions.

5.2.2 Oscillating regime

The flow field developing in the proximity of the endothelial cells during an oscillatory experiment in the cone-and-plate device is now investigated. The geometry of the computational domain is identical to the one used for the steady state case, as previously shown in figure 50.

Geometry and boundary conditions

Similarly to the steady state simulation, the crucial issue is here represented by the imposition of suitable conditions on the domain boundaries. In the previous case, the problem was overcome by interpolating the values for the flow field inside the real cone-and-plate geometry computed using a commercially available software, *Fluent*. Unfortunately, the same procedure cannot be employed for the unsteady case because of the difficulties in obtaining reliable mixed space/time interpolations on the boundaries of the numerical domain. The direct numerical values obtained from the *Fluent* solution do not have adequate spatial resolution to be useful as boundary conditions in the micro-scale computational domain of the cells. An approximate procedure based on a scaled/mixed analysis of both the numerical steady state *Fluent* solution and the analytical solution provided by Chung [19] is thus implemented. Chung obtained a solution for the perturbation equations resulting from a double series expansion in powers of the Reynolds and the Womersley numbers, provided values of these parameters are small. Because of the presence of a fluid free surface at the outer rim of the cone-and-plate device, Chung derived a solution comprising three different terms. The first, additionally expanded in series of the cone angle α,

accounts for the general solution far from the outer rim, while the second defines the flow field in the device outer section. A third term becomes necessary to satisfy the boundary conditions at the radial extremity of the cone-and-plate. As previously observed by Sdougos and Buschmann [88, 11], the zero order solution for the expansion in terms of the Reynolds number defines a primary flow characterized by concentric streamlines whose velocities vary linearly along the vertical direction, and changing in time at the same frequency of the imposed cone oscillation. Both radial and vertical velocity components are identically equal to zero. Considering higher order solutions expanded in terms of both Reynolds and Womersley numbers, new velocity terms accounting for a secondary fluid motion along the radial and vertical directions arise in the solution, oscillating at twice the frequency of the cone. It must be remarked that this analytical formulation for the velocity field derived by Chung cannot be used as a boundary condition for the reduced numerical domain, since it was developed for a cone-and-plate geometry with no gap between the cone tip and the plate surface, in contrast with our experimental setup.

Let's see how to overcome this difficulty. The first step of the proposed procedure involves the comparison of the steady state solutions obtained from both Chung's work and the *Fluent* simulation. Considering that Chung's analytical solution refers to a simplified cone-and-plate geometry lacking a gap between the cone tip and the plate surface, the velocity profiles will need to be compared on a common scale length. For this purpose, the analytical Chung's velocity $\mathbf{u}_{Chung}$ at the generic radial position $r = \bar{r}$ is then adjusted to the new "stretched" domain present in the real experimental device using the following formulation:

$$k(\bar{r}) = \frac{h_{simpl}(\bar{r})}{h_{real}(\bar{r})} \;\Rightarrow\; \mathbf{u}_{Chung-real}(z_{real}) = \mathbf{u}_{Chung}(z_{real} \cdot k(\bar{r})) \tag{108}$$

where h_{real} and h_{simpl} indicate, respectively, the cone height at radius $\bar{r}$ with (real

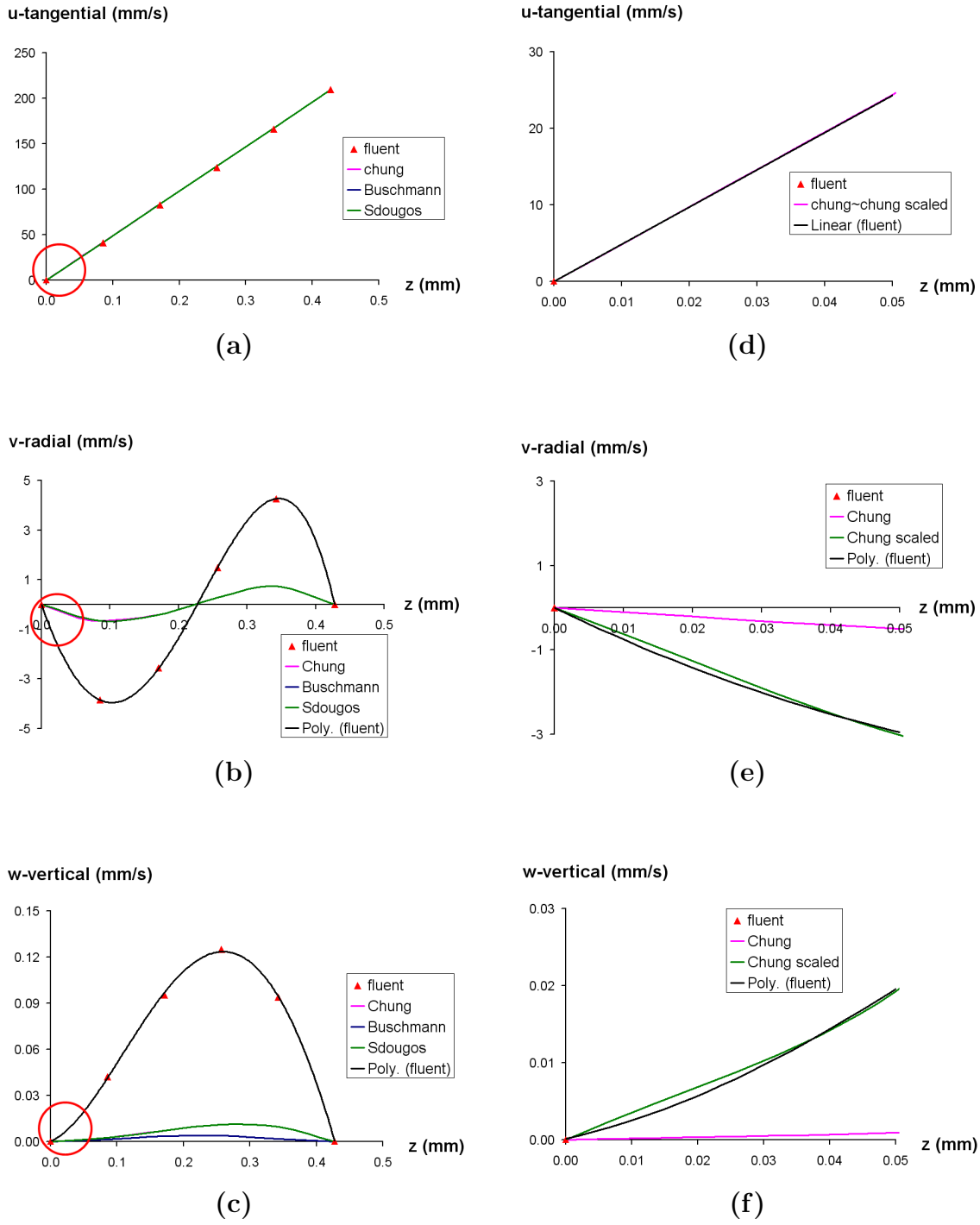

Figure 59: Velocity profiles along the vertical position computed at radial position $r = 20mm$ for the cone rotating at a steady angular velocity 100rpm. The numerical values computed by *Fluent* are compared with the analytical solutions obtained from different authors (a,b,c). The areas circled in red, defining the numerical domain vertical size, are then magnified (d,e,f), and the Chung solution scaled to match the numerical one.

device) or without (Chung simplified version) a gap. Using a constant cone angular velocity of 100rpm and a cone angle $\alpha = 0.5°$, the output velocity profiles at the radial position $r = 20mm$ are shown in figures 59 (a,b,c). The velocities computed by Sdougos and Buschmann, once "stretched", are also presented in the same plots, indicating a good overall agreement with Chung. Similarly, the velocity profiles obtained by the *Fluent* simulation on the realistic geometry can be considered a scaled version of the analytical ones, due to their evident qualitative shape similarity. It is thus assumed that the oscillating flow field inside the real cone-and-plate device will be a scaled version of the analytical solution available for the simplified no gap geometry, furthermore retaining its temporal characteristic frequency. As a consequence, a scale factor between the two steady state solutions is computed for each velocity component in order to obtain an "overlap" of the *Fluent* solution when compared to the Chung one. These scaling parameters are optimized such that the best fit is obtained in the vertical range defining the reduced numerical domain, namely $0\mu m \leq z \leq 50\mu m$. Figures 59 (d,e,f) show the "adjusted" Chung solutions once the velocities scaling factors, roughly defined as

$$k_\phi = \frac{\phi_{Fluent}}{\phi_{Chung-real}} \qquad \phi = u, v, w \tag{109}$$

have been applied. At each instant of time, the new "ad hoc" boundary conditions for the numerical unsteady simulation will thus be represented by the computed values from the Chung analytical solution derived in the oscillating case scaled by the steady state factors $k_{u,v,w}$. Using the pressure boundary conditions previously described for the steady state simulation, all of the described boundary conditions are summarized below

$$
\begin{cases}
initial\ (t=0) & scaled\ oscillating\ analytical\ solution\ with\ no\ cells\ (*) & \\
inlet(x=70\mu m) & \mathbf{u}=(*) & \dfrac{\partial p}{\partial x}=0 \\
outlet(x=230\mu m) & \mathbf{u}=(*) & \dfrac{\partial p}{\partial x}=0 \\
top/lateral\ surfaces & \mathbf{u}=(*) & \dfrac{\partial p}{\partial \mathbf{n}}=constant \\
bottom\ surfaces & \mathbf{u}=0 & \dfrac{\partial p}{\partial \mathbf{n}}=0 \\
cells\ surface & \mathbf{u}=0 & \dfrac{\partial p}{\partial \mathbf{n}}=0
\end{cases}
$$

where the symbol (*) represents the velocity field computed with the described procedure. During the simulation, an angular velocity defined by

$$\Omega(t) = Acos(\omega t)$$

is imposed to the cone, with $A = \omega = 100rpm = 10.5rad/s$. The resulting Reynolds and Womersley numbers will be, respectively, Re=0.42 and W=0.64. Low values for these parameters are also required to justify the use of the series expansion in Chung's analytical approach. A quasi-steady flow field is once again expected.

Results

In order to simulate the evolution in time of an unsteady flow field, the choice for the time step size becomes a critical issue. In a steady state simulation, the time step used for a specific computational mesh must ensure the stability of the solution.

This requirement is equivalent to imposing a higher threshold on the choice of the time step size in order to avoid instability. For an unsteady problem, the necessity to run the simulation for a required amount of "physical" time, usually about three or four times the cone oscillating period T, sets an additional lower limit in the choice of the time step size. In fact, for an extremely small time step, the required computational time could become unreasonably long for our purposes, since it is inversely proportional to the size of the time step. Due to our presently available computational power, a good compromise suggests using a time step $\Delta t = 10^{-5}s$. To avoid instability problems, a non-uniform mesh of approximately 40x40x30=50k grid points is used for the unsteady simulation. The grid size along the x and y directions is kept constant at a value of $4\mu m$, while along the vertical direction it varies from a value of $2\mu m$ in the proximity of the endothelial cells up to $3\mu m$ at the top boundary of the domain. The cells surface is discretized with an unstructured triangular mesh whose elements have a side length of approximately $2\mu m$. As previously described for the steady simulation, this computational set up resulted in error peaks up to 10% when compared to the most refined mesh. The simulation is stopped when a steady state with a pointwise stability error $\varepsilon_s < 10^{-6}$ is reached.

	$\Delta x = \Delta y$	Δz	$\Delta mesh$	Δt
Simulation (h)	$4\mu m$	$2\mu m$	$2\mu m$	$t = 10^{-5}s$

To obtain significant data, once again only the shear stress values registered in the central area of the cells layer are considered in our analysis. In order to analyze the time dependent shear stress field over the endothelial cells, a set of reference points has been chosen on the waveform representing the cone angular velocity as a function of time, as illustrated in figure 60 (a). Once again, figure 60 (c) shows the wall shear stress values as a function of the considered point vertical coordinate

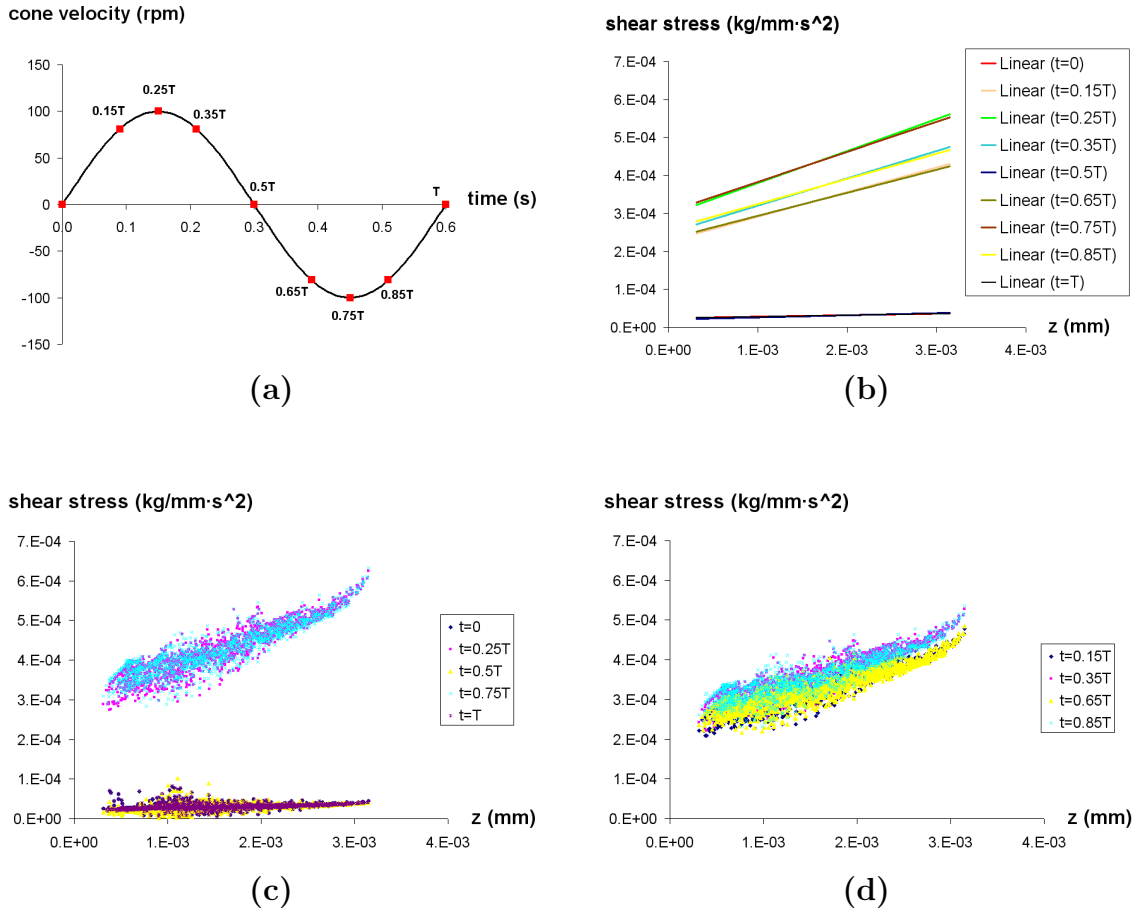

Figure 60: (a) Reference points along an oscillation period T (c,d) Shear stress distribution as a function of the considered point elevation: computed at the specific reference points (b) Linear trends computed from the data sets in c and d. Hereafter, the regression equations are listed for each of the "clumping" patterns observed:
t=0.25T and t=0.75T $\longrightarrow$ y = 0.08461x + 0.00030
t=0.35T and t=0.85T $\longrightarrow$ y = 0.07190x + 0.00025
t=0.15T and t=0.65T $\longrightarrow$ y = 0.06468x + 0.00023
t=0, t=0.5T and t=T $\longrightarrow$ y = 0.00359x + 0.00002

computed at specific instants of time when the cone is either still or rotating at its maximum speed. In figure 60 (d), shear stress values at other instants of time are also presented. Regardless of its vertical coordinate, it is clear how each interface point reaches its peak shear stress value when the cone rotation is at the maximum velocity. Conversely, every time the cone inverts its direction of rotation, each point on the

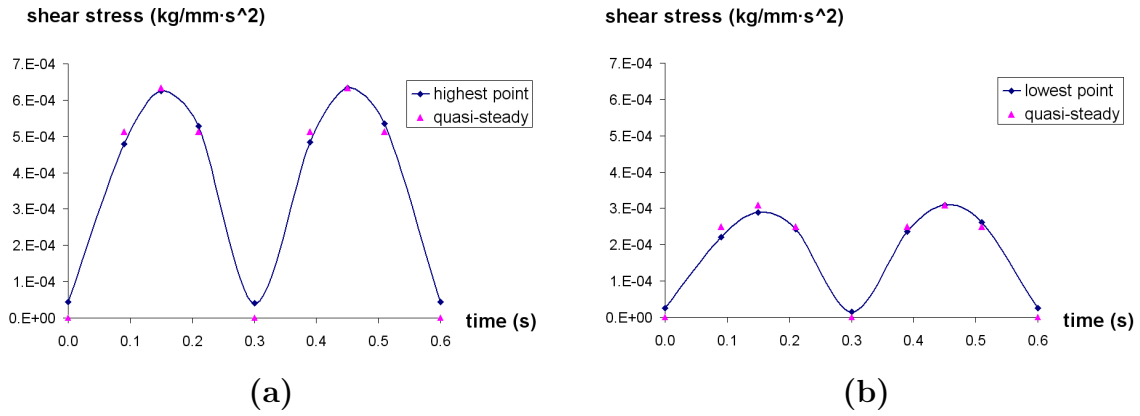

Figure 61: Shear stress evolution in time at the points of maximum (a) and minimum (b) elevation. Comparison with the "theoretical" quasi-steady solution defined in equation (110).

endothelial layer experiences a shear stress value close to zero. This behavior suggests a quasi-steady character of the overall simulation. This observation is sustained by the plot in 60 (b), where the linear regression lines for the shear stress values are represented for all of the considered instants of time. It is very interesting to observe the shear stress evolution in specific areas on the cells interface. Let point A, corresponding to the highest point on the endothelial cells layer, be representative of the areas expressing the highest values of shear stress. Conversely, let point B be chosen inside the deepest depression area on the interface, representing zones of low shear stress values. If we define a quasi-steady shear stress at a generic point P as

$$\tau_{quasi-steady}(t) = |\tau_{100rpm} \cdot cos(\omega t)| \tag{110}$$

where τ_{100rpm} represents the shear stress value computed at P for a steady cone rotation of $100rpm$, figure 61 reveals a different behavior for the points A and B. Point A, located at the top of a single endothelial cell, does not experience a different shear stress value depending on the velocity direction of the cone. This can be considered

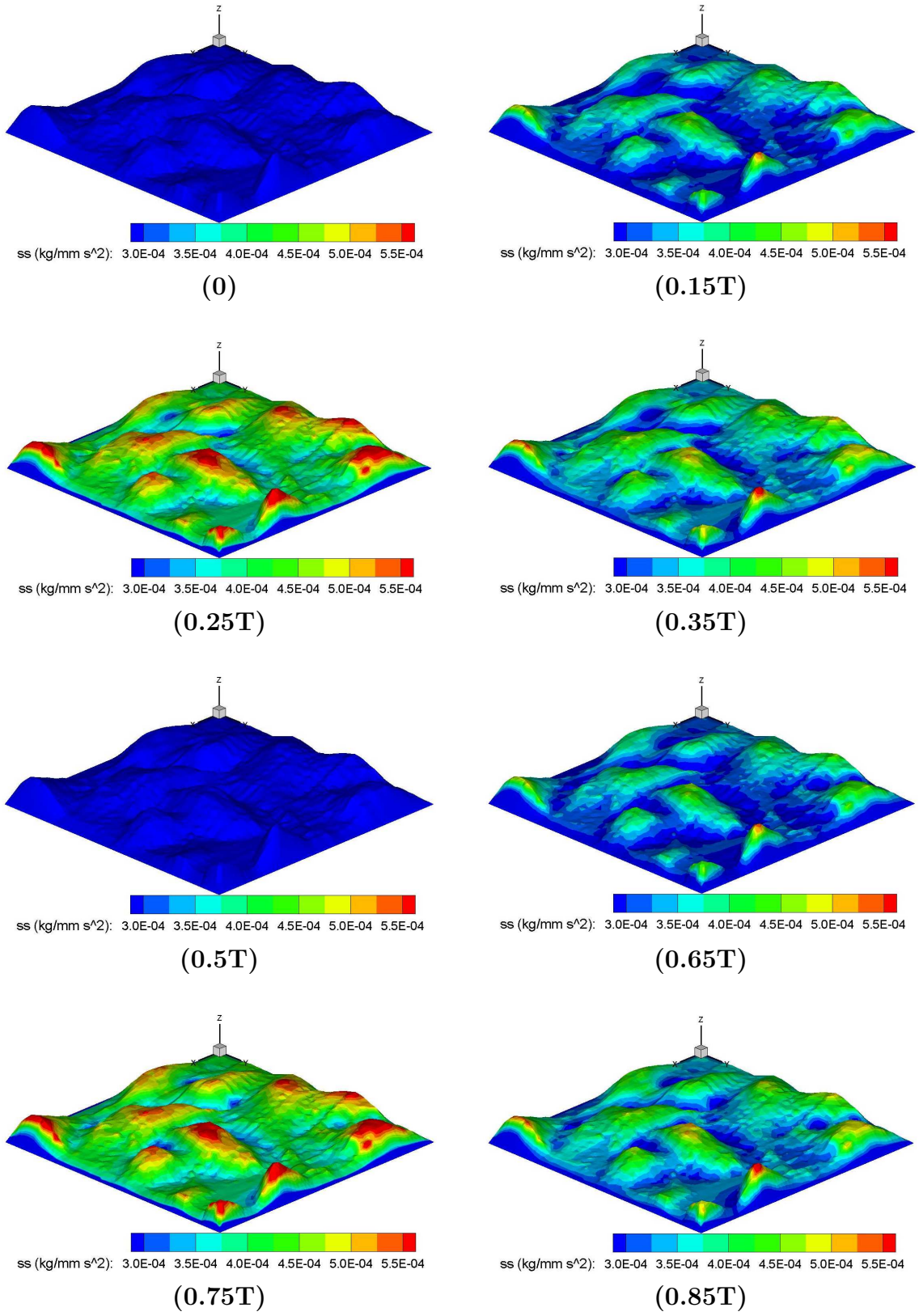

Figure 62: Contour plot for the shear stress distribution at different instants of time.

intuitive, since the cell slope on the two opposite sides does not change significantly. The only difference when compared with an hypothetical quasi-steady state, as observed from figure 61 (a), is the small hysteresis experienced by the shear stress field. In fact, as soon as the cone starts decelerating from the point of maximum velocity, the shear stress value tends to delay its decrease, regardless of the velocity direction imposed by the cone. Accordingly, during the accelerating phase, the shear stress value still tends to increase less rapidly than it would do in case of a quasi-steady flow. However, these effects can be considered more qualitative than quantitative.

Completely different behavior is observed in the depression areas, where the shear stress values are typically very low. Here, as evident from figure 61 (b), a marked asymmetry for the shear stress evolution in time arises as a function of the cone rotating direction, when a difference in the peak shear stress values of about 10% is observed. This suggests a dependency of the shear stress field on the specific surface geometry "upstream" of the considered point. As happened for point A, the same hysteresis is also observed in the shear stress evolution, still being more of a qualitative feature. Finally, as shown in figure 62, the typical shear stress spatial distribution experienced in the steady state simulation is also recovered in the oscillating regime, being the shear stress values scaled as a function of the considered instant of time. It must be also noted how the shear stress field changes at twice the frequency of the rotating device, as expected by the simplified analytical solution.

CHAPTER VI

DISCUSSION AND CONCLUSIONS

The relationship between blood flow, mechanotransduction and the localization of arterial lesions is a central topic in the ongoing investigation of the biology of the endothelium. The development of new technologies in concert with the improvement of existing methods in imaging modalities, computational modeling, fluid dynamics and cellular/molecular biology could represent a powerful tool to advance our understanding of the problem [25].

The goal of this work was to set up a computational tool capable of reproducing the micro-flow field created by experiments performed on a layer of endothelial cells positioned in the cone-and-plate device. The same CFD code can be used to extend the analysis to geometrically different shearing devices. These results can then be used in biological studies to address the influence of the hemodynamic environment over the endothelium.

Numerical results

After a comprehensive validation of the CFD code was performed by running standard test cases of increasing geometrical and physical complexity, the flow field that develops over a group of endothelial cells in the cone-and-plate shearing device during standard biological experiments was investigated. The following conclusions can be inferred from simulations performed at steady and unsteady rotational regimes.

1. Under the steady flow conditions examined in this research, the shear stress distribution over a layer of endothelial cells in the cone-and-plate device can be considered to be the result of two concurrent effects. The shear stress field to

a first order of approximation is linearly proportional to the height of a point on the cell surface. This finding enables a good estimate of the shear stress distribution, assuming the topography of the cells is known, without solving the equations of motion for each situation. However, there are second order effects on the shear stress that depend upon local variations in topology. These were seen as the computational grid was refined to a better spatial resolution, and the micro-effects are likely due to fluid dynamic influences of the specific local neighborhood.

2. For the steady state experiments performed at the cone velocity $\omega = 100rpm$, variations in wall shear stress τ_w were in the range between half and twice the value experienced on the plate surface far form the cells: $0.5 \cdot \tau_{w\_no\_cells} < \tau_w < 2 \cdot \tau_{w\_no\_cells}$. Increasing the cone rotational speed to $400rpm$, the lower threshold for the shear stress values dropped to about one third of $\tau_{w\_no\_cells}$, while the upper bound did not vary. This suggests that the effect of the micro-scale shear stress distribution in the depression areas may increase with the cone velocity, as opposed to the top of the cells. Previous studies on the shear stress distribution under steady state conditions were carried out by Yamaghuchi [84] and Barbee [8]. While the first of these investigators reported endothelial cells to experience peak shear stress values up to six times $\tau_{w\_no\_cells}$, Barbee computed a shear stress field whose values were similar to our results.

3. For the simulations performed in an oscillating regime, a quasi-steady behavior for the computed shear stress field was observed. Nevertheless, a small but clearly observed asymmetry for the shear stress evolution in time in the depression areas arose as a function of the cone rotating direction. A difference in the peak shear stress values of about 10% was observed, suggesting that the "shielding effect" of the neighbors cells plays an important role in the determination of

the shear stress field in these areas. Although the quasi-steady model has been proved to be a good approximation at the low Womersley number used in our studies, we suggest caution in extending this finding as the Womersley number increases.

4. A minor hysteresis is experienced by the flow field during the cone accelerating and decelerating phases, causing a "delay" in the shear stress adaptation to the hypothetical quasi-steady behavior.

Biological implications

It is largely recognized that wall shear stress acting on the arterial walls plays a key role in the physiological and pathological behavior of the endothelium. A qualitative relationship with many of the biological and biochemical processes occurring at the single cell level has been hypothesized, sometimes sustained by direct observation. Starting from the detected change in the cell surface topography [85, 8, 7], wall shear stress has been implicated in the development and adaptation of vascular beds [54] and in the chronic physiological remodeling of large arteries [39]. Other works have focused on its implications in activating specific plasma membrane sensors and receptors, in initiating molecular mechanisms of mechanotransduction [23, 24, 45], in determining specific paths of cellular and subcellular stress distribution [8, 13] and in triggering the amplification of mechanical stimuli by the adhesion to the endothelium of circulating cells and molecules [79, 64]. Moreover, the correlation between the cytoskeleton motion in living cells and the applied mechanical forces has been lately attracting many researchers [28, 63, 46, 100].

The capability of the developed CFD code to model the microscopic flow field in the neighborhood of endothelial cells in response to the imposed mechanical environment could represent a great opportunity to investigate a more quantitative understanding of the specific biological processes.

In this investigation, the geometry of the endothelial cells examined was obtained from cells that were cultured under static conditions, and hence their shapes were not influenced by flow. It is known that endothelial cells exposed to shear *in vitro* or *in vivo* align with the dominant flow direction, and this geometric effect was not modeled in our study. While this limitation was not relevant to the computational methods developed in the research, it does imply caution in drawing conclusions that can be directly applied to cells that have been exposed to flow.

Nonetheless, the results have important implications for interpreting cone-and-plate experiments. The range of Reynolds numbers and Womersley parameters we investigated is typical of *in vitro* studies in many laboratories, so our methods should be applicable to a wide spectrum of biological investigations. The strong effect of gap height on the wall shear stress distribution across the plate surface is clearly seen (e.g. figures 54 and 59), and this should serve to guide biological investigators in the selection of the location of cells to be studied in a cone-and-plate device.

The fact that wall shear stress is, to a good approximation, directly proportional to cell surface height in a given study may help explain mechanism for cell alignment under longer term exposure to flow. Unless there is perfect symmetry in geometry (and this would never be the case with actual cells), the forces created by wall shear stress will tend to form a rotational couple to bring cells towards alignment with the predominant shear stress direction under steady flow conditions. Under oscillatory conditions, on the other hand, the direction of the couple changes within each cycle, producing minimal net rotational forces.

At our institution, ongoing studies in Dr. Jo's lab [51] are focused on investigating caveolae and caveolin-1 spatial distribution on the plasma membrane and its relation to the imposed mechanical environment [9]. These investigators hypothesize that caveolae density on the cell surface may be critical in mechanosensing cell signaling, especially in the activation of the two mechanosensitive signaling proteins ERK and

Akt. The detailed description of the shear stress spatial distribution over the surface of a single endothelial cell could provide us with important indications about the processes linking the mechanical environment to the mechanosignaling process. Other interests of our collaborators include the expression of vascular adhesion molecules, particularly ICAM-1 and VCAM-1, on the endothelial surface and the relationship of their spatial distribution to the micro-environment of wall shear stress.

The overall significance of this work is not only limited to simulating the experimental fluid mechanics conditions found in the cone-and-plate device, but the developed CFD code may also be implemented in other biological systems. Specifically, Dr. Bao's lab [49] is developing bionanotechnologies and biomolecular engineering approaches for basic biological studies and medical applications. On-going research includes in vivo targeting of cell-surface receptors using magnetic nanoparticles, and tagging/targeting of proteins in living cells using quantum-dot based probes. These approaches are being applied to the detection, analysis and diagnosis of cancer, atherosclerosis, and viral infection. They have been developing the magnetic nanoparticle probes for in vivo plaque detection. The broad and long-term goal of these projects is to develop nanotechnology and biomolecular engineering tools and methodologies for the detection and molecular analysis of atherosclerotic plaque formation, which has a compelling medical need. The developed CFD code could then be used to trace the path of single nanoparticles injected in the flow field. Different nanoparticle distributions caused by changes in flow conditions could then be a factor in the clustering of these probes in particular areas of the endothelial cell surface, and this work could then be used to gain a quantitative description of this mechanism.

The methods developed in this study can also be applied to the study of motion of small, nano-sized particles, whether these are biological molecules, such as low density lipoproteins, or fabricated particles. The trajectory of particles near the

endothelial cell surface can be determined from the velocity field using a transformation to a Lagrangian description. For example, the residence time of nanoparticles or lipoproteins in the "valleys" of the surface contour can be determined. Clearly, the relevance to atherogenesis is an important aspect of future work. It is known that atherosclerotic plaques develop in humans in regions of low and/or oscillatory shear stress. An LDL molecule whose trajectory takes it to within one micron of a cell "valley" would remain there for an extended time under the oscillatory conditions investigated here, implying a higher local concentration of LDL. While the biological mechanisms of incorporating LDL into the artery wall are key issue, the microscopic flow environment is a contributing factor and must be understood.

REFERENCES

[1] "A.H.A. heart disease and stroke statistics - 2006 update," tech. rep., American Heart Association, 2006.

[2] "Statistical data about cardiovascular disease in europe," tech. rep., European Heart Network, 2006.

[3] Armfield, S. and Street, R., "The fractional-step method for the Navier-Stokes equations on staggered grids: the accuracy of three variations," *Journal of Computational Physics*, vol. 153, pp. 660–665, 1999.

[4] Armfield, S. and Street, R., "Fractional step methods for the Navier-Stokes equations on non-staggered grids," *ANZIAM Journal*, vol. 42, pp. 134–156, 2000.

[5] Armfield, S. and Street, R., "An analysis and comparison of the time accuracy of fractional-step methods for the NavierStokes equations on staggered grids," *Int. J. Numer. Meth. Fluids*, vol. 38, pp. 255–282, 2002.

[6] Azerad, P. and Bansch, E., "Quasi-stability of the primary flow in a cone and plate viscometer," *J of Mathematical Fluid Mechanics*, vol. 6, pp. 253–271, 2004.

[7] Barbee, K. A., Davies, P. F., and Lal, R., "Shear stress-induced reorganization of the surface topography of living endothelial cells imaged by atomic force microscopy," *Circ. Res.*., vol. 74, pp. 163–171, 1994.

[8] Barbee, K. A., Mundel, T., Lal, R., and Davies, P. F., "Subcellular distribution of shear stress at the surface of flow-aligned and nonaligned endothelial monolayers," *Am J Physiol.*, vol. 268, pp. 1765–1772, 1995.

[9] Boyd, N. L., Park, H., Yi, H., Boo, Y. C., Sorescu, G. P., Sykes, M., and Jo, H., "Chronic shear induces caveolae formation and alters erk and akt responses in endothelial cells," *Am J Physiol Heart Circ Physiol.*, vol. 285(3), pp. 1113–1122, 2003.

[10] Brown, D. L., Cortez, R., and Minion, M. L., "Accurate projection methods for the incompressible Navier-Stokes equations," *Journal of Computational Physics*, vol. 168, pp. 464–499, 2001.

[11] Buschmann, M. H., Dieterich, P., Adams, N. A., and Schnittler, H. J., "Analysis of flow in a cone-and-plate apparatus with respect to spatial and temporal effects on endothelial cells," *Biotechnol Bioeng.*, vol. 89(5), pp. 493–502, 2005.

[12] Bussolari, S. R., Dewey, C. F. J., and Gimbrone, M. A. J., "Apparatus for subjecting living cells to fluid shear stress," *Rev Sci Instrum.*, vol. 53(12), pp. 1851–1854, 1982.

[13] Butler, P. J., Norwich, G., Weinbaum, S., and Chien, S., "Shear stress induces a time- and position-dependent increase in endothelial cell membrane fluidity," *Am J Physiol.*, vol. 280, pp. c962–c969, 2001.

[14] Caro, C. G., *The Mechanics of the Circulation.* Oxford University Press, USA, 1978.

[15] Charm, S. E. and Kurland, G. S., *Blood flow and microcirculation.* New York: Wiley, 1974.

[16] Chiu, J. J., Wang, D. L., chien, S., Skalak, R., and Usami, S., "Effects of disturbed flow on endothelial cells," *J Biomech Eng.*, vol. 120, pp. 2–8, 1998.

[17] Chorin, A. J., "Numerical solution of the Navier-Stokes equations," *Mathematical Computations*, vol. 22, pp. 745–762, 1968.

[18] Chorin, A. J., "On the convergence of discrete approximations to the Navier-Stokes equations," *Mathematical Computations*, vol. 23, pp. 341–353, 1969.

[19] Chung, C. A., Tzou, M. R., and Ho, R. W., "Oscillatory flow in a cone-and-plate bioreactor," *J Biomech Eng.*, vol. 127(4), pp. 601–610, 2005.

[20] Conte, S. D. and DeBoor, C., *Elementary Numerical Analysis.* McGraw-Hill, 1972.

[21] Cox, D. B., "Radial flow in the cone-plate viscometer," *Nature*, vol. 193, p. 670, 1962.

[22] Davies, M. J. and Thomas, A., "Thrombosis and acute coronary artery lesions in sudden cardiac ischemic death," *The New England Journal of Medicine*, vol. 310, pp. 1137–1140, 1984.

[23] Davies, P. F., "Flow-mediated endothelial mechanotransduction," *Physiol. Rev.*, vol. 75, pp. 519–560, 1995.

[24] Davies, P. F. and others, "Spatial relationships in early signaling events of flow-mediated endothelial mechanotransduction," *Annual Review of Physiology*, vol. 59, pp. 527–549, 1997.

[25] Davies, P. F., Spaan, J. A., and Krams, R., "Shear stress biology of the endothelium," *Annals of Biomedical Engineering*, vol. 33, pp. 1714–1718, 2005.

[26] Davies, P. F., Zilberberg, J., and Helmke, B. P., "Spatial microstimuli in endothelial mechanosignaling," *Circ Res.*, vol. 92(4), pp. 359–370, 2003.

[27] DeBakey, M. E., Lawrie, G. M., and Glaeser, D. H., "Patterns of atherosclerosis and their surgical significance," *Annals of surgery*, vol. 201, pp. 115–131, 1985.

[28] Dewey, C. F. J., Bussolari, S. R., Gimbrone, M. A. J., and Davies, P. F., "The dynamic response of vascular endothelial cells to fluid shear stress," *J Biomech Eng.*, vol. 103(3), pp. 177–185, 1981.

[29] Ding, H., Shu, C., Yeo, K. S., and Xu, D., "Numerical computation of three-dimensional incompressible viscous flows in the primitive variable form by local multiquadric differential quadrature method," *Computer Methods in Applied Mechanics and Engineering*, vol. 195, pp. 516–533, 2006.

[30] Dintenfass, L., *Blood microrheology Viscosity factors in blood flow, ischemia and thrombosis*. London: Butterworth, 1972.

[31] Dudgeon, D. J. and Wedgewood, L. E., "Laser doppler measurements of flow in a cone-and-plate rheometer and the effect of cone misalignment," *Rheol Acta*, vol. 36, pp. 28–37, 1997.

[32] Foias, C. and Temam, R., "Remarques sur lesequations de Navier-Stokes stationnaires et les phenomenes successifs de bifurcation," *Annali Scuola Superiore-Pisa*, pp. 29–63, 1978.

[33] Fujima, S., Tabata, M., and Fukasawa, Y., "Extension to three-dimensional problems of the upwind finite element scheme based on the choice of up- and down-wind points," *Comput. Methods Appl. Mech. Engrg.*, vol. 112, pp. 109–131, 1994.

[34] Fuster, V., Badimon, L., Badimon, J. J., and Chesebro, J. H., "The pathogenesis of coronary artery disease and the acute coronary syndromes," *The New England Journal of Medicine*, vol. 326, pp. 242–250, 1992.

[35] Fuster, V., Fayad, A., and Badimon, J. J., "Acute coronary syndromes: biology," *Lancet*, vol. 353(2), pp. SII5–SII9, 1999.

[36] Giddens, D. P., Zarins, C. K., and Glagov, S., "The role of fluid mechanics in the localization and detection of atherosclerosis," *J Biomech Eng.*, vol. 115, pp. 588–594, 1993.

[37] Gilmanov, A. and Sotiropoulos, F., "A hybrid cartesian/immersed boundary method for simulating flows with 3d, geometrically complex, moving bodies," *Journal of Computational Physics*, vol. 207(2), pp. 457–492, 2005.

[38] Gilmanov, A., Sotiropoulos, F., and Balaras, E., "A general reconstruction algorithm for simulating flows with complex 3d immersed boundaries on cartesian grids," *Journal of Computational Physics*, vol. 191(2), pp. 660–669, 2004.

[39] Glagov, S., Weisenberg, E., Zarins, C. K., Stankunavicius, R., and Kolettis, G. J., "Compensatory enlargement of human atherosclerotic coronary arteries," *The New England journal of medicine*, vol. 316(22), pp. 1371–5, 1987.

[40] Glagov, S., Zarins, C. K., Giddens, D. P., and Ku, D. N., "Hemodynamics and atherosclerosis: insights and perspectives gained from studies of human arteries," *Arch. Pathol. Lab. Med.*, vol. 112, pp. 1118–1031, 1988.

[41] Gresho, P., "On the theory of semi-implicit projection methods for viscous incompressible ow and its implementation via a nite element method that also introduces a nearly consistent mass matrix i: Theory," *Int. J. Num. Meth. Fluids*, vol. 11, pp. 587–620, 1990.

[42] Guermond, J. L. and Quartapelle, L., "Calculation of incompressible viscous flows by an unconditionally stable projection fem," *Journal of Computational Physics*, vol. 132, pp. 12–33, 1997.

[43] Guj, G. and Stella, F., "A vorticity-velocity method for the numerical solution of 3d incompressible flows," *J. Comput. Phys.*, vol. 106, pp. 286–298, 1993.

[44] Hazel, A. L. and Pedley, T. J., "Alteration of mean wall shear stress near an oscillation stagnation point," *J Biomech Eng.*, vol. 120, pp. 227–237, 1988.

[45] Helmke, B. P. and Davies, P. F., "The cytoskeleton under external fluid mechanical forces: hemodynamic forces acting on the endothelium," *Annals of Biomedical Engineering*, vol. 30, pp. 284–296, 2002.

[46] Helmke, B. P., Goldman, R. D., and Davies, P. F., "Rapid displacement of vimentin intermediate filaments in living endothelial cells exposed to flow," *Circ. Res.*, vol. 86, pp. 745–752, 2000.

[47] Hiptmair, R., "Discrete hodge operators," *Numerische Mathematik*, vol. 90(2), pp. 265–289, 2001.

[48] Hirt, C. W., Amsden, A. A., and Cook, J. L., "An arbitrary lagrangian-neulerian computing method for all flow speeds," *Journal of Computational Physics*, vol. 14(3), pp. 227–253, 1974.

[49] http://www.bme.gatech.edu/groups/bao/.

[50] Jiang, B. N., Lin, T. L., and Povinelli, L. A., "Large-scale computation of incompressible viscous flow by least-squares finite element method," *Comput. Methods Appl. Mech. Engrg.*, vol. 114, pp. 213–231, 1994.

[51] Jo, H., Song, H., and Mowbray, A., "Role of nadph oxidases in disturbed flow- and bmp4- induced inflammation and atherosclerosis," *Antioxidants & Redox Signaling*, vol. 8, pp. 1609–1619, 2006.

[52] Johnson, A., *Numerical and experimental investigation of flow past a sphere up to a Reynolds number of 300*. PhD thesis, University of Iowa, 1996.

[53] Johnson, A. and Patel, V. C., "Flow past a sphere up to a Reynolds number of 300," *J. Fluid Mech.*, vol. 378, pp. 19–70, 1999.

[54] Kamiya, A., Bukhari, R., and Togawa, T., "Adaptive regulation of wall shear stress opimizing vascular tree function," *Bull. Math. Biol.*, vol. 46, pp. 127–137, 1984.

[55] Kim, J. and Moin, P., "Application of a fractional-step method to incompressible Navier-Stokes equations," *Journal of Computational Physics*, vol. 59, pp. 308–323, 1985.

[56] Ku, D. N., Giddens, D. P., Zarins, C. K., and Glagov, S., "Pulsatile flow and atherosclerosis in the human carotid bifurcation. positive correlations between plaque location and low oscillation shear stress," *Arteriosclerosis*, vol. 5, pp. 293–302, 1985.

[57] Ku, H. C., Hirsh, R. S., and Taylor, T. D., "A pseudospectral method for solution of the three-dimensional incompressible Navier-Stokes equations," *J. Comput. Phys.*, vol. 70, pp. 439–462, 1987.

[58] Ladyzhenskaya, O., *The Mathematical Theory of Viscous Incompressible Flow*. Gordon and Breach, New York, 1969.

[59] Langille, B. L. and Adamson, S. L., "Relationship between blood flow direction and endothelial cell orientation at arterial branch sites in rabbits and mice," *Circulation Research*, vol. 48, pp. 481–488, 1981.

[60] Levesque, M. J., Liepsch, D., Moravec, S., and Nerem, R. M., "Correlation of endothelial cell shape and wall shear stress in a stenosed dog aorta," *Arteriosclerosis*, vol. 6, pp. 220–229, 1986.

[61] Levesque, M. J., Nerem, R. M., and Sprague, E. A., "Vascular endothelial cell proliferation in culture and the influence of flow," *Biomaterials*, vol. 11, pp. 702–707, 1990.

[62] Lusis, A. J., "Atherosclerosis," *Nature*, vol. 407, pp. 233–241, 2000.

[63] Malek, A. M. and Izumo, S., "Mechanism of endothelial cell shape change and cytoskeletal remodeling in response to fluid shear stress," *J Cell Sci.*, vol. 109, pp. 713–726, 1996.

[64] Malinauskas, R., Herrmann, R., and Truskey, G., "The distribution of intimal white blood cells in the normal rabbit aorta," *Atherosclerosis*, vol. 115, pp. 147–163, 1995.

[65] McGill, H. C., "Persistent problems in the pathogenesis of atherosclerosis," *Arteriosclerosis*, vol. 4), pp. 443–451, 1984.

[66] McLachlan, N. W., *Bessel functions for engineers*. Oxford University Press, 1941.

[67] Meakin, R. L., "Object x-rays for cutting holes in composite overset structured grids," *AIAA Computational Fluid Dynamics Conference, 15th*, June 2001.

[68] Merill, E. W., "Rheology of blood," *Physiol. Rev.*, vol. 49, pp. 863–888, 1969.

[69] Mooney, M. and Ewart, R. H., "The conicylindrical viscometer," *Physics*, vol. 5, pp. 350–354, 1934.

[70] Moore, J. E., Xu, C., Glagov, S., Zarins, C. K., and Ku, D. N., "Fluid wall shear stress measurements in a model of the human abdominal aorta: oscillatory behavior and relationship to atherosclerosis," *Atherosclerosis*, vol. 110, pp. 225–240, 1994.

[71] Noria, S., Xu, F., McCue, S., Jones, M., Gotlieb, A. I., and Langille, B. L., "Assembly and reorientation of stress fibers drives morphological changes to endothelial cells exposed to shear stress," *Am J Pathol.*, vol. 164(4), pp. 1211–1223, 2004.

[72] Pao, H. P., "Numerical solution of the Navier Stokes equations for flows in the disk-cylinder system," *The Physics of Fluids*, vol. 15(1), pp. 4–11, 1972.

[73] Pedley, T. J., *The Fluid Mechanics of Large Blood Vessels*. Cambridge University Press, 1980.

[74] Pelech, I. and Shapiro, A. H., "Flexible disk rotating on a gas film next to a wall," *J. Appl. Mech.*, vol. 31, pp. 577–584, 1964.

[75] Quartapelle, L., *Numerical Solution of the Incompressible Navier-Stokes Equations*. Birkhuser, 1993.

[76] Quartapelle, L., "Fractional-step projection methods," to be published.

[77] Quarteroni, A., *Elementi di calcolo numerico*. Progetto Leonardo, 1995.

[78] Robbins, S., Kumar, V., and Cotran, R. S., *Basic Pathology*. Saunders, 7th ed., 2003.

[79] Ross, R., "Cell biology of atherosclerosis," *Annual Review of phisiology*, vol. 57), pp. 791–804, 1995.

[80] Ross, R., "Atherosclerosis - an inflammatory disease," *The New England journal of medicine*, vol. 340(2), pp. 115–126, 1999.

[81] Ross, R. and Glomset, J. A., "Atherosclerosis and the arterial smooth muscle cell: Proliferation of smooth muscle is a key event in the genesis of the lesions of atherosclerosis," *The New England journal of medicine*, vol. 180(93), pp. 1332–9, 1973.

[82] Rouhanizadeh, M., Lin, L., Arcas, D., and Hsiai, T., "Spatial variations in shear stress at low reynolds number flow," *Annals of Biomedical Engineering*, vol. 33(10), pp. 1425–1440, 2005.

[83] Rouhanizadeh, M., Soundararajan, G., Arcas, D., Lo, R., Browand, F., and Hsiai, T., "Mems sensors to resolve spatial variations in shear stress in a 3-d bifurcation model," *IEEE Sensors*, vol. 6(1), pp. 78–88, 2006.

[84] Sakurai, A., Nakano, A., Yamaguchi, T., Masuda, M., and Fujiwara, K., "A computational fluid mechanical study of flow over cultured endothelial cells," *Adv Bioeng.*, vol. 20, pp. 299–302, 1991.

[85] Satcher, R. L. J., Bussolari, S. R., Gimbrone, M. A. J., and Dewey, C. F. J., "The distribution of fluid forces on model arterial endothelium using computational fluid dynamics," *J Biomech Eng.*, vol. 114(3), pp. 309–316, 1992.

[86] Schmid-Schonbein, G. V. and Granger, D. N., *Molecular Basis for Microcirculatory Disorders*. Springer, 2003.

[87] Schouveiler, L., Gal, P. L., Chauve, M. P., and Takeda, Y., "Spiral and circular waves in the flow between a rotating and a stationary disk," *Experiments in Fluids*, vol. 26, p. 179187, 1999.

[88] Sdougos, H. P., Bussolari, S. R., and Dewey, C. F., "Secondary flow and turbulence in a cone-and-plate device," *J Fluid Mechanics*, vol. 138, pp. 379–404, 1984.

[89] Shen, J., "On error estimates of projection methods for Navier Stokes equations: first order schemes," *SIAM Journal of Numerical Analysis*, vol. 29, pp. 57–77, 1992.

[90] Shen, J., "On error estimates of some higher order projection and penalty-projection methods for Navier Stokes equations," *Numer. Math.*, vol. 62, pp. 49–73, 1992.

[91] Slattery, J. C., "Analysis of the cone-plate viscometer," *J. Coll. Sci.*, vol. 16, pp. 431–437, 1961.

[92] Soundararajan, G., Yu, M. R. H., DeMaio, L., and Hsiai, E. S. K. T., "Mems shear stress sensors for microcirculation," *Sensors and Actuators: A. Physical.*, vol. 118(1), pp. 25–32, 2005.

[93] Svindland, A., "The localization of sudanophilic and fibrous plaques in the main coronary bifurcation," *Atherosclerosis*, vol. 48, pp. 139–145, 1983.

[94] Temam, R., "Sur l'approximation de la solution des equations de Navier-stoke par la methode des fractionnarires ii," *Arch. Rational Mech. Anal.*, vol. 33, pp. 377–385, 1969.

[95] Valentine, D. T. and Jahnke, C. C., "Flows induced in a cylinder with both end walls rotating," *Phys. Fluids*, vol. 6(8), pp. 2702–2710, 1994.

[96] Weinan, E. and Liu, J. G., "Projection method i -convergence and numerical boundary layers," *SIAM Journal on Numerical Analysis*, vol. 32, pp. 1017–1057, 1995.

[97] Womersley, J. R., "Methods for the calculation of velocity, rate of flow and viscous drag in arteries when the pressure gradient in known," *Journal of Physiology*, vol. 127, pp. 553–563, 1955.

[98] Womersley, J. R., "An elastic tube theory of pulse transmission and oscillatory flow in mammalian arteries," *Aeronautical research laboratory*, vol. WADC TR 56-614, 1957.

[99] Yamaguchi, T., Yamamoto, Y., and Liu, H., "Computational mechanical model studies on the spontaneous emergent morphogenesis of the cultured endothelial cells," *Journal of Biomechanics*, vol. 33, pp. 115–126, 2000.

[100] Yoon, M., Moir, R. D., Prahlad, V., and Goldman, R. D., "Motile properties of vimentin intermediate filaments in living cells," *J Cell Biol.*, vol. 143, pp. 147–157, 1998.

[101] Zarins, C. K., Giddens, D. P., Bharadvaj, B. K., Sottiurai, V. S., Mabon, R. F., and Glagov, S., "Carotid bifurcation atherosclerosis. quantitative correlation of plaque localization with flow velocity profiles and wall shear stress," *Circulation Research*, vol. 53, pp. 502–514, 1983.